Molecular dynamics studies of phase transition of n-alkanes mixtures, coupling-decoupling mechanism affecting thermal interfacial conductance of n-alkanes and Fokker-Planck theory of lattice thermal conductivity of crystalline solids

by

Yi Zeng

A dissertation submitted to the Graduate Faculty of
Auburn University
in partial fulfillment of the
requirements for the Degree of
Doctor of Philosophy

Auburn, Alabama
December 14, 2019

Keywords: Molecular Dynamics, Energy Storage, Interface Conductance, Phase Change Materials, Soft Materials, Thermal Conductivity and Thermal Transport

Approved by

Jay M. Khodadadi, Co-Chair, Professor, Mechanical Engineering Department
Jianjun Dong, Co-Chair, Professor, Department of Physics
Roy W. Knight, Associate Professor, Mechanical Engineering Department
Daniel Mackowski, Professor, Mechanical Engineering Department

Abstract

Renewable energy sources, such as solar energy or geothermal energy, are promising to complement or even substitute unsustainable fossil fuel energy sources in direct thermal energy utilization. The requirement of a reliable and stable supply from renewable energy mandates highly effective energy storage systems that are capable to absorb and release a large amount of heat over a short period of time. This leads to the exploits of various phase change materials (PCM) with complex structures and/or compositions for their potential applications in thermal energy storage. Thermal transport properties of PCM are essential to the effectiveness of the thermal energy storage systems. Despite recent progresses in thermal conductivity measurements and atomistic level numerical simulation techniques, heat transfer mechanisms in nano-structured organic PCM and bulk crystalline PCM near melting temperatures are known only at a qualitative level. In both cases, Hook's Law-like harmonic interatomic forces is no longer an accurate approximation to describe the atomistic dynamics that governs the heat transfer processes in these materials. Therefore, anharmonic effects that include the contributions of higher-order potential terms were considered. Further improvement of the effectiveness of complex PCM needs a more quantitative understanding of the fundamental mechanisms associated with thermal transport of these intrinsically anharmonic materials.

We first performed a set of systematic molecular dynamics (MD) simulations of the structures and bulk thermal conductivity of mixtures of long-chain n-alkane molecules. We

identified how the orientation factor of the n-alkane mixtures is affected by the surface during the crystallization process, where the surface can be artificially adjusted to be attractive or repulsive to n-alkane molecules. We further demonstrated that the thermal conductivity of the mixtures correlate strongly with the orientation of n-alkane chains in the solid-state phase, yet it is insensitive to the number ratio of the mixture.

Next, we focus on elucidating the microscopic mechanism of heat transfer across the van der Waals (vdW) force bonded molecular interfaces. To simplify our study, we constructed ideal crystal models of n-eicosane, where all molecules are perfectly aligned in the same direction. Knowledge of the interfacial thermal transport in such idealized n-alkane crystals is important to understanding the upper limits of overall thermal conductivity in such nano-structured molecular crystals. It is important to note that the thermal interfacial conductance (TIC) of these perfectly-aligned n-alkanes crystals cannot be predicted by conventional interfacial heat transfer models such as the acoustic mismatch model (AMM) and the diffusive mismatch model (DMM), because both atomic structures and their vibrational dynamics are essentially identical at both sides of the interface when averaged over a long period of time. By analyzing the MD-simulated atomistic dynamics at the single atomic/molecular level, we unveiled a thermal coupling-decoupling mechanism that emerges from stochastic dynamics of atoms. Two parameters, the duration and strength of the thermal coupling, are identified to quantify the TIC from the single atomic level. This coupling-decoupling mechanism explains the temperature-inverse-TIC in n-alkanes and provides new insights into heat transfer across a broad range of flexible interfaces that consist of nano-meter long molecules and weak interfacial forces, such as interfacial self-assembled monolayers or paraffins or lipid types of soft materials.

Finally, we expanded our study to develop new transport theories and simulation methods that are applicable for a wide range of solids at the temperature conditions near the solid-to-liquid phase transition, i.e. melting. This study is in part motivated by our findings of the drastic effects of increasing anharmonic interfacial forces on heat transfer properties in n-alkanes near their melting temperatures. The failure of harmonic or quasi-harmonic approximations near melting temperatures is unavoidable in all types of PCM, including both soft molecular materials for near human-body temperature applications and the hard oxides adopted in the high-temperature applications. The widely-adopted phonon gas (PG) model, which requires anharmonic effects are perturbatively small, likely breaks down at such high temperatures. As the first step to develop a unified theoretical model for heat transfer within very anharmonic solids, either strongly-bonded bulk crystals or weakly-bonded molecular nano-materials, we proposed a Fokker-Planck equation (FPE) theory to describe stochastic fluctuations and relaxation processes of lattice vibration for a wide range of conditions, including those beyond the PG limit. Using the time-dependent, multiple state-variable probability function of a vibration FPE, we first derive time-correlation functions of lattice heat currents in terms of correlation functions among multiple vibrational modes, and subsequently predict the lattice thermal conductivity based on the Green-Kubo formalism. When the quasi-particle kinetic transport theories are valid, this vibration FPE not only predicts a lattice thermal conductivity that is identical to the one predicted by the phonon Boltzmann transport equation, but also provides additional microscopic details on the multiple-mode correlation functions. More importantly, when the kinetic theories become insufficient due to the break-down of the PG approximation, this FPE theory remains valid to study the correlation functions among vibrational modes in highly anharmonic lattices with significant mode-mode interactions and/or in

disordered lattices with strongly-localized modes. We also discussed the possible MD simulation algorithms that can extract the parameters of vibrational FPE for very anharmonic solids.

Acknowledgments

Time flies. It is hard to believe that I am about to finish my Ph.D. work at this moment. Without many people's help, this dissertation would never have been completed. I would like to gratefully acknowledge their help.

I would like to express my sincere appreciation to my advisor, Dr. Jay M. Khodadadi, for his supervision, support and encouragement that has led me to finish this academic adventure during my doctoral study at Auburn. In addition to letting me choose my research topics with complete freedom, he has always guided me on the right track of my research road by organizing routine meetings, revising my drafts with insightful suggestions, and providing opportunities for my professional growth.

I'd like to thank my co-advisor, Dr. Jianjun Dong from the Department of Physics. His knowledge, experience, and perceptive observations on fundamental theory of thermal transport has guided me to build a fundamental understanding on phonon transport, the connection between engineering and science, and the broader impact of my research. It is my fortune to work with him.

I would like to thank my dissertation committee members, Dr. Roy Knight and Dr. Daniel Mackowski, for their useful advice on improvement of my dissertation. Special thanks go to Dr. Ash Abebe from the Department of Mathematics and Statistics, for serving as the outside reader of my dissertation.

I am grateful to the Graduate Research Scholars Program of the Alabama Experimental Program to Stimulate Competitive Research through three rounds (10 to 12) of scholarship support and the US Department of Energy (Award Number DE-SC0002470) for the financial support of my doctoral research.

I am very grateful for the friendship of all of my friends. Many thanks to Lopez Omar, Kurt Johnson and Sanders for the daily discussions of physics problems, Python programming and steak cooking. In addition, thanks to my friends Alin, Dadapi, Damao, John Zheng and Zhepi for sharing the enjoyable game time.

Finally, I am deeply thankful to my family for their love, support, and sacrifice. Moreover, their encouragement helped me keep moving forward during frustrating times.

Table of Contents

List of Tables

List of Figures

List of Abbreviations

AIREBO	Adaptive Intermolecular Reactive Empirical Bond Order potential
AMM	acoustic mismatch model
BTE	Boltzmann transport equation
COMPASS	Condensed-phase Optimized Molecular Potentials for Atomistic Simulation Studies
DMM	diffusive mismatch model
EMD	equilibrium molecular dynamics
FPE	Fokker-Plank equation
IFCs	interatomic force constants
LAMMPS	Large-scale Atomic/Molecular Massively Parallel Simulator
LHTES	latent heat thermal energy storage
LJ	Lennard-Jones
MD	molecular dynamics
N-Alkane	normal alkane
NEMD	non-equilibrium molecular dynamics
NERD	Nath, Escobedo and de Pablo-Revised
OPLS	Optimized Potentials for Liquid Simulations
PCM	phase change materials
PGA	phonon gas approximation
phBTE	phonon Boltzmann transport equation
ReaxFF	reactive force field
SKS	Smit, Karaborni and Siepmann
smRTA	Single mode relaxation time approximation
TES	thermal energy storage
TIC	thermal interfacial conductance

TraPPE	transferable potentials for phase equilibria
UA	united atom
vdW	van der Waals

List of Symbols

Nomenclature

A	drift coefficient
B	diffusion coefficient
C	correlation function
c_α	specific heat of phonon mode α
$\mathcal{D}$	normalized drift/diffusion matrix
E	energy, kcal/mol
$\mathbf{f}$	force on a particle, kcal/(mol Å)
$\mathbf{G}$	reciprocal lattice vector, cm^{-1}
G_K	thermal interfacial conductance, W/(mK)
$\hbar$	reduce Planck Constant, J s
J	heat current, Kcal/(mol fs)
k_B	Boltzmann Constant, J/K
L	length, Å
N	number of atoms or phonon modes
n	phonon number
P	pressure, $\mathrm{N/m}^2$; probability function
$\mathbf{p}$	momentum of particles, kg m/s
q	heat flux, Kcal/(mol fs)
q_atom	atomic interfacial heat current, kcal/(mol fs)
$\mathbf{q}$	wave vector of phonons, cm^{-1}
$\mathbf{r}$	position vector of particles, Å
T	temperature, K

t	time, s, fs
$\Delta\hat{V}$	perturbatively small deviations in the vibration Hamiltonian
V	volume of simulation box and crystal, Å^3
v	velocity, Å/fs
W	work, kcal/(mol fs)
w	rate of transition
X, Y	physical quantities
x, y, z	Cartesian coordinates

Greek Symbols

α	index of phonon modes; thermal coupling ratio
β	index of phonon modes
Γ	vibration micro-state
γ	fitted decay factors, index of phonon modes
γ_K	single molecule thermal conductance, pW/(m K)
Δ	statistical variance; difference
δ	Delta function; change of a quantity
ε	Lennard-Jones parameter, energy scale
κ	thermal conductivity, W/(m K)
μ	eigenvector of scattering matrix
σ	Lennard-Jones parameter, length scale; standard deviation
τ	phonon lifetime, ps
Ω	volume of the unit-cell, Å^3
ω	frequency, Thz, cm^{-1}

Subscripts

c	coupling process
cell	supercell
d	decoupling process
eq	equilibrium state
I, J, K	x, y or z
i	particle i
int	interface
k	reciprocal space k vector
L	left side of the interface
Latt	lattice
N	total number phonon modes
R	right side of the interface
X, Y	physical quantities
α , β , γ	index of phonon modes
λ	index of eigenvalue
μ, v	indices
∞	infinity

Superscripts

0	initial state
β	index of phonon modes

Chapter 1 Introduction

1.1 Background

Fossil fuels and electricity, which are conventional high-exergy sources of energy, will continue to provide the largest share of heating and cooling energy for human activities in the foreseeable future. At the same time, economically and environmentally sustainable renewable energy sources become increasingly vital to meet the ever-increasing world-wide energy demands as economy grows and quality of human lives improve. Direct heating technologies that utilize low-exergy renewable energy sources, for example, simple solar thermal collection systems, are especially promising for applications within the low-to-medium temperature range of 0-260 °C [1], i.e. the temperature range that is closely relevant to a majority of human activities, because they not only reduce the fossil fuels consumption but also lead to an optimization of the energy end-use efficiency (Figure 1-1).

1.2 Thermal Energy Storage Through Phase Transition

Unfortunately, the temporal and spatial disparity between energy supply and energy demand imposes a fundamental challenge for any operationally stable and economically competitive utilization of renewable energies. In effect, storage of different forms of energy remains as the greatest obstacle to further utilization of renewable energy. In particular, thermal energy storage (TES) systems, which can effectively store and release heat, have become an indispensable component of any dispatchable renewable energy technology [2]. Most promising TES systems nowadays use the so-called phase change materials (PCM), which undergo solid to liquid transitions at their melting temperatures and absorb/release large amounts of latent heat with only small volume change. This type of TES systems is often referred as latent heat TES (LHTES) systems. A class of organic PCM, e.g. alkanes or sugar alcohols, have been extensively studied as promising candidates for low-to-medium temperature LHTES systems. Previous studies have shown that a wide range of options of melting temperatures within this temperature range can be engineered using this class of organic PCM. As compared to low-melting metals and molten salts, these hydrocarbon-based PCM have higher energy storage density, negligible phase separation or super-cooling during phase transition, low toxicity and non-corrosiveness to metals.

1.3 Improvement of Thermal Conductivity of PCM

Further optimization of the properties of these organic PCM for thermal energy storage applications requires more detailed and quantitative understanding of microscopic heat transfer mechanisms inside these complex materials systems that consist of high density of internal interfaces that are only bonded with the relatively weak van der Walls (vdW) forces or hydrogen-bond forces. For example, the inherently low thermal conductivity of organic PCM sets a constraint on thermal efficiency of LHTES system by limiting heat exchange between the PCM and heat transfer medium. The values of thermal conductivity and the prices of some typical engineering materials are presented in Figure 1-2. One technical solution to increase thermal conductivity is to design a LHTES system combined with highly thermally conductive structures, such as metal/carbon-based fins or forms, which essentially increases the contact area between the PCM and heat transfer medium with an inevitable increase in cost and mass of the LHTES system [4]. To enhance the flexibility of LHTES design, researchers have searched for other solutions. Nano-scale structures with high thermal conductivity are proposed to be used as fillers into PCM to synthesis nano-enhanced PCM [5]. These PCM filled with nano-composite can accelerate the charging/melting and discharging/solidification processes of LHTES system, resulting in an enhancement of their thermal performance. One key obstacle to effectively engineer thermal transport properties in organic nano-composite PCM is the underlying filler-to-host interfacial heat transfer mechanisms that remain unclear at the molecular level.

1.4 Thermal Transport at the Atomic scale

Using molecular dynamics (MD) simulations, microscopic heat transfer mechanisms covering the macroscopic scale thermal transport properties can be assessed and explained by the collective behaviors of atoms. Considering n-alkane molecules, there exists a huge discrepancy between the inter-molecular and intra-molecular interactions, resulting in an obvious difference on the thermal transport rate within and among molecules. For a certain number of n-alkanes with linear chain structures, heat transfer within their molecules are nearly ballistic since the mean free path of the phonon is longer than the length of the molecular chains. The orientation of the molecules is a crucial parameter for their effective bulk thermal conductivities at the micro-scale level.

Meanwhile, addition of nanostructures can serve as a template for those molecules to align in a more orderly way, which essentially provides more thermal transport tunnels and higher thermal conductivity. In addition, the molecular interfaces between two nano-meter long n-alkane molecular blocks with weak van der Waals interfacial bonding have relatively low thermal interfacial conductance (TIC). Unfortunately, the limited length of those long-chain n-alkanes, e.g. eicosane ($C_{20}H_{42}$) with a length of ~2 nm, inevitably introduces a large number of molecular interfaces to dominate thermal transport even though a microscopic molecular system is constructed from only thousands of molecules. However, the conventional acoustic mismatch (AMM) model or the diffusive mismatch model (DMM) [6] are clearly insufficient to predict TIC of this type of flexible interfaces because the dynamically-averaged atomic configurations on both sides of such an interface are essentially identical, i.e. no atomistic mismatch exists. An improved atomistic-scale understanding of the interfacial heat transfer mechanisms is needed for development of next-generation of advanced materials with improved TIC.

Our simulation studies of temperature-dependent interfacial thermal conductance of organic PCM clearly unveil the drastic effects of increasing the anharmonic chemical bonding on heat transfer properties around solids' melting temperatures. Although such drastic increase of anharmonicity is expected in all PCM when they go through the solid-to-liquid structural transitions, there are lack of quantitative transport theories to quantify the effects on the thermal conductivity of highly anharmonic solids. Even for conventional crystals, our understanding of temperature-dependence of the thermal conductivity is largely based on the so-called phonon gas approximation (PGA) [7][8], which describes the thermal excitation and relaxation processes within a vibrating lattice in term of weakling interacting quasi-particles phonons and assumes the single-particle Bose-Einstein statistics for phonon number distributions at thermal equilibrium. When the PGA is valid, the phonon Boltzmann transport equation (phBTE) [9][10] is the default choice of transport theory for the thermal conductivity calculation from first principles. Other important assumptions adopted by the phBTE are: (1) the lifetime of every phonon is finite because of the scatterings by lattice anharmonicity, lattice defects/disorder, or other particles, and (2) each quasi-particle phonon travels at its group velocity. Multiple implementations of the phonon BTE methods have been reported in recent years, and the calculated results adopting various theoretical and numerical approximations have been systematically bench-marked among themselves and compared with available experimental data. The overall good agreement between the first-principles computational results and available experimental data for a large number of crystals at moderate temperatures establishes the phBTE as a practical and robust computational tool to design advanced technology materials with optimized thermal transport properties.

However, concerns have been raised about the validity of the phonon BTE beyond the PGA limit, where interactions among the vibrational modes are significant and the weakly interacting quasi-particle approximation becomes insufficient. In addition, the group-velocity approximation limits the application of phBTE to study solids with strong structural disorder since the group velocity cannot be defined unambiguously without translational periodicity. The lack of a quantitative theory for lattice thermal conductivity beyond the PGA limit motivates us to develop a unified theoretical model for heat transfer within highly anharmonic solids, either strongly-bonded bulk crystals or weakly-bonded molecular nano-materials. This study is of the broad interest to understand thermal transport properties of PCM, especially at the temperature ranges near the melting temperatures.

1.5 Structure of the Dissertation

Chapter 2 contains the literature reviews of the work on molecular structure of long-chain n-alkanes during crystallization/melting process in MD simulations, the thermal transport of long-chain polymers by utilizing MD methods, and the predictions of the lattice thermal conductivity of crystalline solid based on first principle calculations.

In Chapter 3, the theoretical methodologies utilized in this thesis are explained. MD simulation is described at first. The evaluation of thermal conductivity based on the non-equilibrium MD approach is explained. Then, the calculation of lattice thermal conductivity in crystalline solid based on phBTE is presented.

In Chapter 4, the effect of the orientation of the mixtures of n-alkanes molecules on the thermal conductivity of the n-alkane mixtures is illustrated by utilizing MD simulations. In addition, the contribution from the number ratio of the mixture is also discussed.

In Chapter 5, a thermal coupling and decoupling mechanism of the interfacial thermal conductance of long-chain molecules in MD simulations is presented. Two thermal coupling parameters are evaluated quantitively for a wide temperature range.

In Chapter 6, a Fokker-Planck equation (FPE) theory is presented to describe stochastic fluctuation and relaxation processes of lattice vibration over a wide range of conditions, including those beyond the PGA limit. By comparing the results of our vibration FPE and those of the phBTE, a quantitative criterion to delineate the break-down condition of the PGA at high temperatures is proposed. We further discuss the possible MD algorithms to extract the drift and diffusion parameters for vibrational normal modes at very high temperatures.

Finally, the conclusions of the dissertation and the future research directions are presented in Chapter 7.

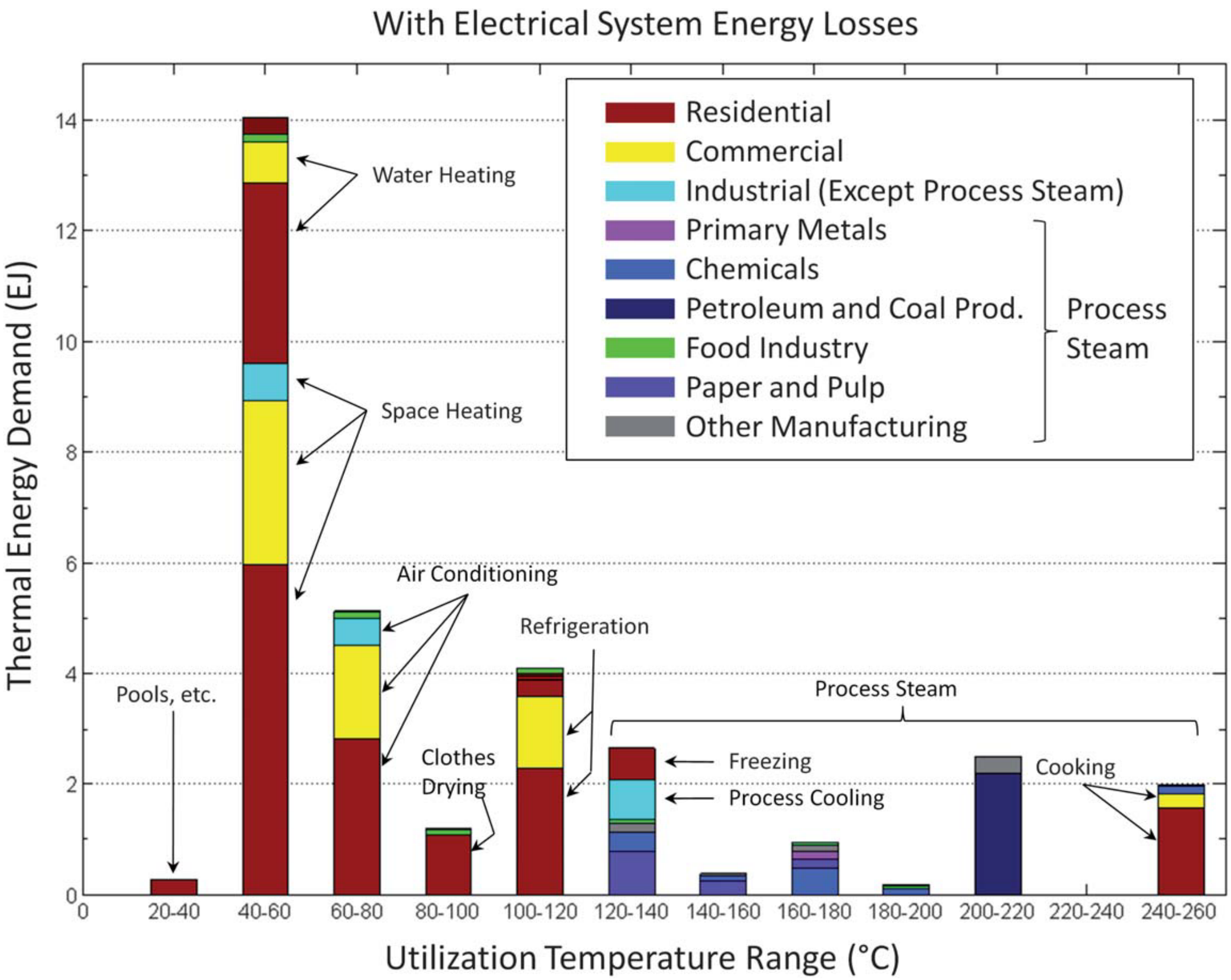

Figure 1-1 Thermal energy usage versus temperature distribution from 0 to 260 °C with Electrical System Energy Losses in the United State. The end-uses with the largest contribution are annotated. The total thermal energy demand from 0 to 260 °C in 2008 was 33.5 EJ (31.7 quads). [1]

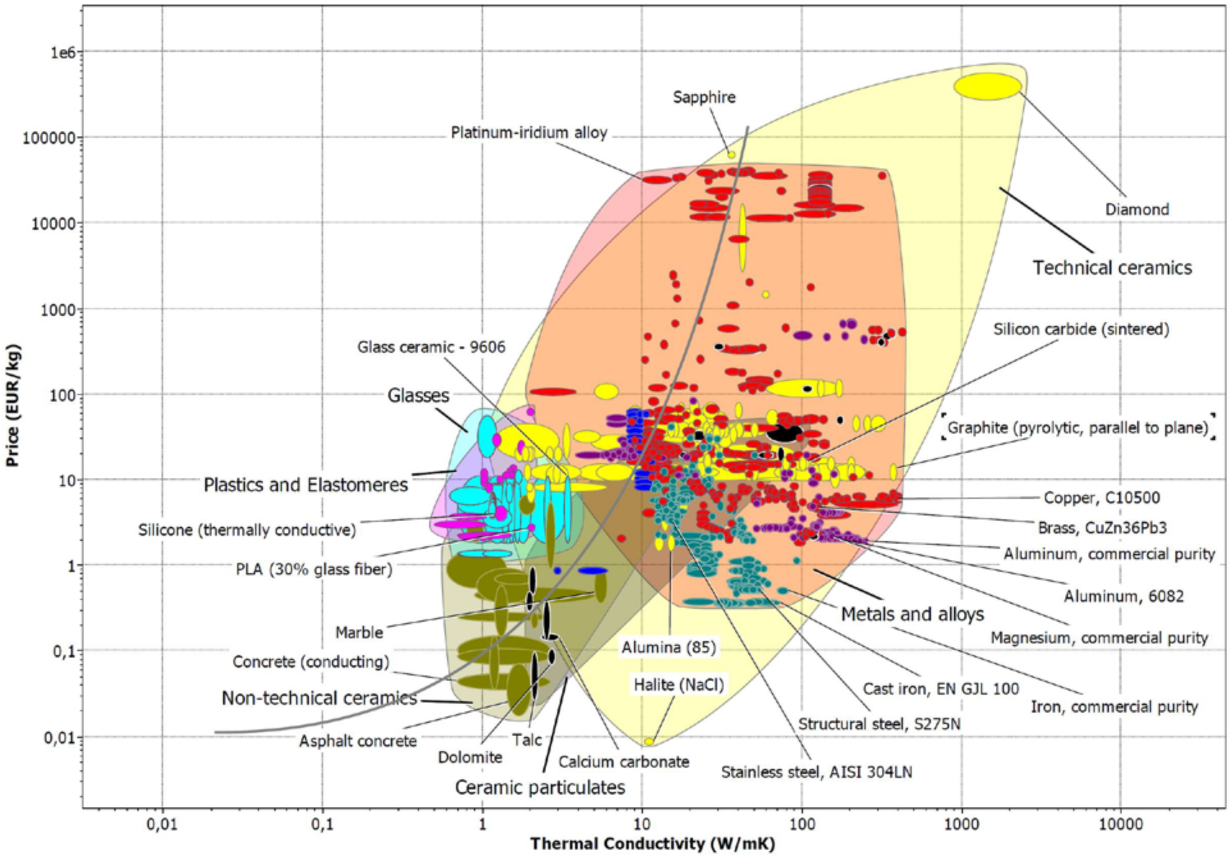

Figure 1-2 Thermal conductivity vs. price for engineering materials. The colored areas indicate the family envelopes. The grey line is the approximate Pareto frontier which presents the optimal allocation of price on thermal conductivity. [3]

Chapter 2 Literature Survey

In this chapter, a comprehensive literature survey on thermal transport of nano-structured polymeric solids and bulk crystals is presented. The review contains three parts: the first part discusses the molecular structure of n-alkanes during melting and crystallization in MD simulations; the second part focuses on the calculations of thermal transport of long-chain polymers by MD simulations. In the third part, a series of theoretical work on first-principles calculations of lattice thermal conductivity of crystalline solids are summarized. The strengths and limitations of the computational methods adopted in these studies are discussed.

2.1 Molecular Structures

In this section, a review of MD simulations to reveal the crystallization and melting of n-alkanes are presented. The effect of the chain-length, crystallization temperature and surface potential on the dynamic characteristics and quantitative nucleation rate of n-alkane molecules are elucidated by MD simulations. For shorter chain n-alkanes, the strength of the surface potential is highly crucial to the orientation of the molecules in the crystal, adjusting the orientation of the lamella structure to be parallel or perpendicular to the surface. In addition, the orientation of the molecules is highly related to its microscopic thermal transport, which will be discussed in Chapter 4.

Straight-chain n-alkanes C_nH_{2n+2} (henceforth denoted as C_n), as the main byproducts of petroleum processing, are promising candidates for thermal energy storage applications for the low-temperature range. In addition, these n-alkanes with heavy molecular weight crystallizing at low temperatures are the primary components forming the wax deposits, which involves nucleation of liquid molecules and thermal transport through the thin wax deposits layer[11][12]. Crystallization of n-alkanes has been widely investigated by experimental methods, identifying the respective phases and transition temperatures[13]. During the crystallization processes, the rotator phases of n-alkanes are observed in-between the liquid and the crystalline solid phase, presenting noticeable variation of properties dependent on the n-alkanes' molecular length and the even-odd effect[13][14]. Deeper understandings of crystallization of n-alkanes have been explored at the nanoscale by performing molecular dynamics (MD) simulations with various empirical and semi-empirical potentials.

Shimizu and Yamamoto [15] carried out MD simulation on the melting and crystallization in the thin film of n-alkanes ($C_{10}H_{22}$) with the simple bead-spring model. As the surface molecules were perpendicular to the surface, it provided a stable surface to initiate the melting from the interior molecules. During crystallization processes, a layer-by-layer growth of stacked lamellae with a hexagonal structure can be reproduced by slow cooling due to the nucleation sites from the surface monolayers. The surface state of the thin film strongly affected the melting and crystallization processes of n-alkanes.

Waheed et al. [15] performed nonequilibrium MD simulations to obtain the crystal growth rate for n-alkanes with a united-atom model. In the presence of a surface potential, the crystal of n-eicosane in a hexagonal phase grew on the surface potential from an amorphous phase as the temperature decreases from 400 K to 285 K. In addition, simulations in isothermal crystallization were performed for the temperature range from 225 K to 300 K. The growth rate of crystallization cannot be calculated above 295 K due to the formation and re-melting of molecules in the simulation. When the temperature dropped below 240 K, the simulations took too long to obtain a growth rate owing to the super low mobility of molecules.

Yamamoto et al. [16] investigated the crystallization in short n-alkanes ($C_{11}H_{24}$) by MD simulations with a united atom model. An artificial ultrathin film was designed in the simulation to serve as the substrate for molecular crystallization. Through adjusting the interaction force between substrate and molecules, the crystallization of short n-alkanes can present two different patterns: perpendicular and parallel growth. A strong attraction from the substrate led to a parallel lamella and a weak attraction substrate prefers the perpendicular lamellae that have a higher melting point than the bulk.

Wentzel and Milner [18] executed an all atom simulation of pure of $C_{23}H_{48}$ and mixture of $C_{21}H_{44}$ $C_{23}H_{48}$ to characterize their disorder in n-alkane rotator phases. Three potentials (OPLS-AA, Borodin and Smith, FW) were tested in the simulation and only the FW potential could provide a reasonable result agreeing with experimental observations of all the rotator phases. A spurious monoclinic crystal phase was found to be stably existing in a narrow temperature range between orthorhombic crystal and RI phases for all potentials, even though it was not observed from experiments, which might be a result of tiny energy difference between the orthorhombic and monoclinic crystals. In simulation with periodic boundary condition, pure C_{23} had difficulty in nucleating a region of amorphous melt in a relatively small initially-ordered system, resulting in a persistence in solid state at temperatures 15 K above the melting point. An extended temperature range of 35 K for stable rotator phases was observed in the 50 – 50 mixture of C_{21} and C_{23} alkanes, which was about two times that of the temperature range of pure C_{23}. The extended temperature range for stable rotator phases is a result of the breakdown of interlayer interaction that lead to the crystal ordering in pure alkanes, which provides more experimental and numerical flexibility to the studies on the properties of the RI and RII phases.

Anwar et al. [19] identified the microscopic mechanisms of homogeneous crystal nucleation and growth by conducting MD simulation of the crystallization of C_{20}. As nucleation initiated, the molecular chain started aligning and then straighten with an increase in the local density, leading to formation of an ordered structure. Other independent chains then tried to join to the existing crystallin cluster with one end and then slid to attaching the crystallized chains.

Yi and Rutledge [20] studied homogeneous nucleation of the crystal phase in n-octane (C_8H_{18}) melts by MD simulation with a united atom model. Reasonable agreement of the structure of crystal phase and the melting temperature of C_8 was achieved between the MD simulations and experimental results. In addition, a cylindrical nucleus model based on the classical nucleation theory was proposed to provide a description of the dependence of free energy on the nucleus size. At 170 K and 180 K, the free energy of formation reached their maximum value when the numbers of molecules were around 18 – 25. However, the critical nucleus was observed at 190 K due to the limitation of the size of the simulated system. In addition, as the temperature increased, the interfacial free energy of the side surface kept relatively stable, while the interfacial free energy of the end surface had significant drop from 5.4 mJ/m^2 to about 3 mJ/m^2.

Yi and Rutledge [21] simulated the homogeneous nucleation of n-eicosane ($C_{20}H_{42}$) crystal from supercooled melt by MD with a united atom model. The melt C_{20} molecules were quenched from 400 K to 250 K for nucleation. After 40 nanoseconds, the crystal started stably to grow and the size of largest nucleus grew over 200 numbers to be serve as the object for rest of the system crystallization. There existed a relative flatness of the top the free energy barrier below 200 nuclei, which led to either the re-melt or the formation of a stable crystal phase.

Luo et al. [22] performed MD simulation on the study of the crystallization behavior of pure n-alkanes and their binary and polydisperse mixtures. The response of the molecules with different chain-lengths to the equilibrium temperature led to the phenomena of segregation of molecules. Shorter chain n-alkanes have higher mobility in comparison to the longer ones at the same temperature, which leads to a strong molecular length-dependent segregation in the binary mixtures of n-alkanes (C_{10} C_{20} and C_{10} C_{30}). Smaller difference of the chain length of molecules in a polydisperse mixture exhibits a weaker segregation than the binary case.

Yamamoto [23] studied the crystallization of multicomponent system of n-alkanes, binary mixtures of C_{10} – C_{20}, a tertiary mixture of C_{10} – C_{14} – C_{20}, and a quaternary mixture of C_{10} – C_{14} – C_{20} – C_{25}, by MD simulations. Due to existence of segregation among multicomponent system of n-alkanes, molecular domain structure with same chain-length were formed and the domain structures with closer chain-lengths were located closer while the distinct chain-length were well-separated. This phenomenon is achieved by the self-diffusion of short chains which first escaped from a lamella then reattached to the neighbor lamella. In addition, the existence of the surface potential drives the long-chain molecules in the multicomponent mixture of n-alkanes forming a lamellar structure and leads to a rapid crystallization process.

In this section, a review of MD simulations to reveal the crystallization and melting of n-alkanes was presented. The effect of the chain-length, crystallization temperature and surface potential on the dynamic characteristics and quantitative nucleation rate of n-alkane molecules are elucidated by MD simulations. For shorter chain n-alkanes, the strength of the surface potential is highly crucial to the orientation of the molecules in the crystal, adjusting the orientation of the lamella structure to be parallel or perpendicular to the surface. In addition, the orientation of the molecules is highly related to its microscopic thermal transport, which will be discussed in Chapter 4.

2.2 Heat Transfer Properties of Long-Chain Polymers

Due to the difficulty in direct measurement/observation of temperature distribution and/or heat fluxes at the nano-meter scale, molecular dynamics (MD) simulations have been widely adopted to provide non-continuum theoretical models to understand heat transfer properties of polymers. While bulk non-metallic polymers with amorphous molecular structures typically have low bulk thermal conductivity, some MD simulation studies have shown that certain polymers with ordered or partially-ordered long molecular chains are intrinsically highly conductive of heat.

Using an AIREBO all-atom potential based MD simulations with the Green-Kubo formalism and a modal decomposition analysis method, Henry and Chen [24] revealed a very high thermal conductivity (~ 1000 W/mK) in a single polyethylene (PE) chain, which is several orders of magnitude higher than that of a bulk PE. The existence of the non-attenuating modes with very long relaxation times has been proposed as the main contribution to this observed high thermal conductivity. The boundary scattering in the short chain-length cases is also found to suppress the effectiveness of this non-attenuating mode base heat transfer mechanism due to the high density of the internal chain-to-chain interfaces.

Liu and Yang [25] further showed in their all-atom MD simulation studies that the enhancement of the thermal conductivity of polymer materials at the stretched condition correlates with an observed alignment of polymer chains due to mechanical stretching. The simulation results showed a more than five-fold increase in the thermal conductivity when the polymers were stretched three times the original length. A higher thermal conductivity of polymer can be reached with a slower stretching rate. In addition, the molecular weight also plays an important role on the thermal conductivity under the same stretching condition. More importantly, the enhancement of thermal conductivity of polymers is mainly driven by approaching a higher orientational order of molecules under larger strains.

Luo et al. [26] performed NEMD simulations to study the thermal energy transport in polydimethylsiloxane (PDMS), an important long-chain component of thermal interface materials.

Although the thermal conductivity of a single molecular chain of PDMS is comparable with that of a single PE molecular chain, the overall bulk thermal conductivity of lab-synthesized bulk PDMS is only ~ 7 W/mK, a value significantly lower than that of bulk PE materials. The huge discrepancy on bulk thermal conductivity between PE and PDMS is mainly contributed from the conformational disorders that are introduced by the random rotations in the silicon-oxygen-silicon segments in the PDMS molecular chains.

Zhang and Luo [27] studied the influence of morphology on thermal conductivity of PE single chain and crystalline fiber using MD simulations. The morphology of crystalline PE is found to be sensitive to temperature, i.e. an ordered system transits to a disordered one as the temperature increases from 300 K to 700 K. This transition leads a monotonous decrease in crystalline PE's thermal conductivity and an abrupt drop of the thermal conductivity is observed between 380 K and 400 K in a relaxed molecular system. By artificially increasing the dihedral energy in single PE chain, the molecule becomes stiffer and more thermally conductive due to reduction of the along-chain disorder and phonon scattering within chain.

Liu and Yang [28] reported a comprehensive MD investigation of length-dependent thermal conductivity of eight different types of polymer materials: PE, polyacetylene, polybutadiene, polybenzimid, poly(p-phenylene), poly(phenylene ether), poly(methylene oxide) and poly(ethylene oxide). They found that the polymer materials with stiffer backbones usually have higher thermal conductivity. The thermal conductivity of single polymer chain that consists of double carbon-carbon (C=C) bonds can be 2.6 times that of PE materials that consists of single carbon-carbon (C-C) bonded molecular chains. The thermal conductivity of polybutadiene, which consists of a mixture of single and double carbon-carbon bonds, is lower than that of PE. In addition, the polymers that incorporate into aliphatic/aromatic pristine chains have lower thermal conductivities due to the creation of localized vibrational modes from mass disorder. As the length of the polymers increases, the intrinsic phonon scattering becomes more significant on their thermal transport.

Zhang and Luo [29] took full advantage of the temperature-related morphology of crystalline PE to regulate its thermal conductivity in their MD simulations. By adjusting temperature from 380 K to 410 K, the thermal conductivity of crystalline PE drops from about 30 W/mK to 5 W/mK with a transition from an ordered crystalline structure to an amorphous one. Meanwhile, the inverse switch of thermal conductivity can be reached by increasing the strain. The tunability of thermal conductivity can be achieved from 5 to 12 in MD simulations, with the largest value was reached by the combination of temperature and strain.

Babaei, Keblinski and Khodadadi [30] [31] performed NEMD simulations on the calculation of thermal conductivity of the mixture of paraffin molecules and carbon nanotubes (CNT)/graphene in both solid and liquid phases. Interestingly, enhancement of thermal conductivity was found in the mixture but not directly originating from introduction of the carbon-based nanofillers. Both fillers, CNT and graphene, are mainly treated as template for arrangement of the paraffin molecules in a more orderly way, leading a transition from amorphous to crystalline. Strong correlation was found between the thermal conductivity values and alignment parameters of the mixture, with the higher alignment parameter always connected to a registered high thermal conductivity.

Zhang et al. [32] studied a series of polymer nanofibers and found the connections between their thermal conductivity and molecular characteristics by MD simulations at different temperatures. The suppression of segmental rotations and large phonon group velocity mainly result in the good thermal stability of polymer nanofibers, leading to a desirable thermal conductivity. In addition, heavier atoms (e.g. oxygen) and weaker backbone bonds brought low thermal conductivity to polymers by employing a low phonon group velocity. At high temperatures, the confined segmental rotations become excited and the thermal conductivity of polymers drop due to the introduction of the disorder-phonon scattering. Therefore, the π-conjugate polymers with intrinsically ordered backbones, strong bonds and dihedral angles, can be the potential choices on fabricating nanofibers with high thermal conductivity for high-temperature applications.

In addition to the aforementioned efforts on thermal conductivity of polymers, the interfacial thermal transport across them is also of great importance to the macroscopic thermal conductivity. In Chapter 5, the mechanisms that are applicable for amorphous interfaces will be discussed.

2.3 Lattice Thermal Conductivity of Bulk Crystals

First-principles calculations of the lattice thermal conductivity (κ_{Latt}) of crystals are mainly performed by solution of the phBTE [33]. The theoretical foundation of the phonon BTE is the so-called phonon gas (PG) model, which assumes that interactions among vibrational modes are weak enough that the numbers of phonons of each mode follow the single-particle Bose-Einstein distribution at equilibrium. The phBTE assumes that (1) each quasiparticle phonon travels at a group velocity v_g, and (2) the lifetime τ of every phonon is finite because of the scatterings by lattice anharmonicity, lattice defects/disorder, or other particles. For electronic insulators, the necessary inputs for a phonon BTE calculation are the harmonic phonon spectra and the phonon scattering terms, both of which can be numerically calculated using the first-principles methods. Multiple implementations of the phonon BTE methods have been reported in recent years. The calculations can be categorized into two categories: (1) the single mode relaxation time approximation (smRTA) ([34][35]) and (2) the full solutions of the phonon BTE, by either iteration methods, variational methods, or exact diagonalization methods.

Within the smRTA approximation, Tang and Dong [34] predicted the κ_{Latt} of MgO at conditions ranging from ambient to the core-mantle boundary. A good agreement between the calculation and experimental results was achieved in the low pressure-temperature conditions, providing reasonable results for the κ_{Latt} of MgO in the lower mantle. These numerical results indicated that the calculated κ_{Latt} of MgO notably change with depth in the lower mantle, increasing from 15-20 W/mK around the 670 km to 40-50 W/mK around the mantle side of core-mantle boundary, providing a controversy of the constant-thermal-conductivity assumption adopted in many geodynamics simulation studies of low mantle. Tang et al. [34] also further improved the numerical efficiency of their algorithms with massive code parallelization and extended their studies to the $MgSiO_3$ perovskites, which consisted of a 20-atom unit. Based on the first principles predicted pressure and temperature dependence of the thermal conductivity of Fe-bearing MgO and $MgSiO_3$, they proposed a theoretical model of the overall thermal conductivity of the lower mantle, which is approximately constant between 2.5 and 3.5 W/mK. These values imply that the mantle has a blanketing effect on heat flow across the core-mantle boundary.

Broido et al.[35] presented a series of first-principles calculations of lattice thermal conductivity of Si and Ge, also within the smRTA approximation. For a wide range of temperature, excellent agreement (<5% difference at room temperature) between the calculated and measured intrinsic κ_{Latt} of silicon and germanium is achieved. The acoustic phonons are the main contribution to the κ_{Latt} of Si and Ge, providing 95% and 92% of κ_{Latt} of Si and Ge, respectively, at room temperature. Meanwhile, the optic phonons also served as dominating scattering channels for heat-carrying acoustic phonons to prevent a dramatic increase in the κ_{Latt}. However, Ward et al. [36]

also demonstrated that the smRTA approximation is not universally valid. For example, smRTA fails to accurately predict κ_{Latt} in Diamond due to the neglect of the effects of the off-diagonal terms in the phonon-phonon scattering matrices. A full solution of BTE is necessary for the calculation of κ_{Latt} in Diamond. It is important to note that the discrepancy between the full solutions and the approximate smRTA solutions of phBTE usually diminished as the temperature increases, suggesting the effects is not related to the failure of PGA.

Cepellotti and Marzari [37] reported a diagonalization method to numerically evaluate the eigenstates of the phonon scattering matrix in the phBTE. They further proposed to interpret such eigen-states as “relaxons”, a kind of collective phonon excitations, to provide an alternative kinetic description of microscopic thermal transport in crystalline materials. Each relaxon is a linear combination of all phonons and decays to its equilibrium state after excitation. The parity of relaxons show that only the odd relaxons contribute to heat flux and determine the κ_{Latt} but the even ones are not able to change the κ_{Latt}. This numerical diagonalization approach, although more computationally intensive, is valuable in the case the iterative method fails to converge in some cases, for example, 2D graphene. As “relaxon” behaviors manifest the correlated phonon dynamics, the “relaxon” effects are expected to more significant at lower temperatures rather than at high temperatures.

To study anharmonic phonon interactions beyond the perturbative approximation, such as the phonon scattering rates calculated with the Fermi’s golden rule, Esfarjani and Chen [38] combined both MD simulation method and the lattice dynamics approach to study the thermal properties of Si. The extraction of the force constant from first-principle density functional theory calculations was applied to provide a reliable potential for MD simulations. Within the Green-Kubo formalism, the heat flux autocorrelation was extracted from MD simulations for the κ_{Latt}

calculations. In addition, the extracted force constant was also applied to obtain the phonon life times in combination with the perturbation theory. Thus, the κ_{Latt} in an isotropic system can be calculated from the smRTA. The small differences of the κ_{Latt} between the two methods above the Debye temperature, i.e. the MD results are 10% to 20% higher than those of the lattice dynamics calculated, indicate that the phonon gas approximation is valid in Si bulk crystals for the studied temperature ranges. However, it is important to point out that only 3rd and 4th order lattice anharmonicity are retained in their MD simulations in order to significantly reduce the computational loads of MD simulations. As a result, such approaches do not apply to highly anharmonic crystals, such as crystals near their melting temperatures.

Similar combined MD and lattice dynamics studies have been reported Lu et al. [39] for the prediction of the κ_{Latt} of lead telluride (PbTe). In this study, the MD simulations are carried out without the truncation of lattice anharmonicity, i.e. in principle, all orders of lattice anharmonicity are included. For the temperature range of 300 to 800 K, the anharmonic phonon dispersions are highly related to the temperature change and observed avoided crossing between transverse optical modes and longitudinal acoustic modes at 600 K. In addition, the phonon mean free paths of optical modes are shorter than the lattice constant, which can provide lower thermal conductivity at higher temperatures. This indicates a possibility of the break-down of the PGA in PbTe at the elevated temperatures, at least for the optic phonons. At the same time, the calculated low values of PbTE (1 – 2 W/mK) is consistent with experimental data. However, it remains unclear how much the small simulation cell artifacts affects the uncertainties of the derived values of $\kappa_{\mathrm{Latt},}$ since the scattering rates are typically sensitive to the size of simulation cells.

Another approach to evaluate the effects of increased anharmonicity at the evaluated temperatures have also been reported in recent years. Feng et al. [40] investigated the four-phonon scattering in the calculation of κ_{Latt} of boron arsenide, silicon and diamond, and presented that the higher-order anharmonicity reduces the calculated κ_{Latt} to a great extent to agree with the experimental data at high temperatures. Including these four-phonon scatterings, the lifetime of optic phonon is significantly reduced due to the creation of more scattering configurations between optical and acoustic modes. This effect becomes more important at higher temperatures for crystalline materials. A detailed study on the effects of the phonon frequency renormalization to the thermal and thermal transport properties of NaCl is reported by Ravichandran and Broido [41]. Their conclusions are consistent with those of Feng et al. [40]. This class of calculations are still based on the PGA and phBTE.

In summary, the calculated κ_{Latt} from phBTE adopting various theoretical and numerical approximations have been systematically benchmarked among themselves and compared with available experimental data. The overall good agreement between the first-principles computational results and available experimental data for a large amount of crystals at moderate temperatures establishes the phBTE as a practical and robust computational tool to design advanced technology materials with optimized thermal transport properties, wherever the PGA is a valid approximation. Meanwhile, concerns have been raised about the validity of the phonon BTE beyond the PG limit, where interactions among vibrational modes are significant and the weakly interacting quasiparticle approximation becomes insufficient.

Chapter 3 Computational Methodology

3.1 Molecular Dynamics Simulation

Classical molecular dynamics (MD) simulation is an atomic simulation method that provides the evolution of a micro-system by tracing the trajectories all the atoms in space. These atoms are generally treated as single particles in the simulation with neglecting the interaction within the atom. The interactions among those particles are usually calculated from an empirical force field. In addition, Ab-initio MD is required if the interactions within the atom, e.g. between ions and electrons, need to be considered. In classical MD simulations, the dynamics of all the particles are governed by the Newton's equation of motion coupled with empirical potentials and appropriate initial and boundary conditions. To connect those individual atoms' microscopic dynamics to macroscopic properties, statistical mechanics is usually used to analyze the simulation results.

3.1.1 Governing equation

The Newtonian equation of motion is in the governing position for running an MD simulation. For a system with N particles and potential E_{U} at a time interval t, the equations are:

$$m\frac{d^2\mathbf{r}_i}{dt^2} = -\nabla \bullet E_{\mathrm{U}}(\mathbf{r}_i)\text{, } i = 1, 2, \ldots, N\text{,} \qquad \text{Eq. (3.1)}$$

where m is the mass of particles and $\mathbf{r}$ is the coordinate of each particles in space. It should be noted that the potential energy E_{U} is only a function of all the particles' coordinates in the system. Therefore, the essence to describe a molecular system is to provide the coordinates' evolution of all the particles with certain constraints.

3.1.2 Potential energy

In order to solve the Newton's equation of motion, appropriate empirical potential energy functions are applied in the MD simulations. These potential energy functions, also called the force field, are a collection of mathematical expressions to describe the dependent energy of a system on the coordinates of its particles. An appropriate force field can provide a precise description of the molecular interactions and a proper reproduction of the system's dynamics. For an organic molecular system, its total potential energy, E_{U}, term can be always separated into the intramolecular, E_{intraU}, and the intermolecular, E_{interU}, parts:

$$E_{\mathrm{U}} = E_{\mathrm{intraU}} + E_{\mathrm{interU}} . \qquad \text{Eq. (3.2)}$$

The intramolecular potential energy itself that accounts for the interactions within a molecule is usually divided into four parts:

$$E_{\mathrm{intraU}} = E_{\mathrm{bond}} + E_{\mathrm{angle}} + E_{\mathrm{dihedral}} + E_{\mathrm{improper}} , \qquad \text{Eq. (3.3)}$$

where E_{bond}, E_{angle}, E_{dihedral} and E_{improper}, represent the bond stretching interaction, angle bending interaction, torsional dihedral interaction and improper dihedral interaction, respectively.

The intermolecular potential energy consists of the van der Waals (vdW) interaction in its 6 – 12 Lennard-Jones form and the Coulomb interactions:

$$E_{\mathrm{interU}} = 4\varepsilon\left[\left(\frac{\sigma}{r_{ij}}\right)^{12} - \left(\frac{\sigma}{r_{ij}}\right)^{6}\right] + \frac{Cq_i q_j}{\varepsilon_C r_{ij}} , \qquad \text{Eq. (3.4)}$$

where ε stands for the depth of potential well and σ is the finite distance at which the inter-particle potential is zero, r_{ij} is the distance between particles i and j, C is an energy-conversion constant, q_i and q_j are the charges on the two particles, and ε_C is the dielectric constant.

In MD simulation of organic materials, e.g. n-alkane, the all-atom force fields, such as OPLS (Optimized Potentials for Liquid Simulations) [42], COMPASS (Condensed-phase

Optimized Molecular Potentials for Atomistic Simulation Studies) [43] and ReaxFF (reactive force field) [44], have been applied to describe the thermodynamic properties by considering the motions of all the atoms in the molecular system. In addition, the united atom force field, approximately treating the methylene (–CH_2–) and the methyl (CH_3–) as groups of atoms, also provide robust macroscopic thermodynamic properties of n-alkane molecules due to the large mismatch between the high bond-stretching frequencies of the C–H bonds and low oscillating frequencies. Various united atom force fields, such as TraPPE (Transferable potentials for phase equilibria) [46], SKS (Smith, Karaborni and Siepmann) [47] and NERD (Nath, Escobedo and de Pablo-revised) [48] exist for n-alkanes MD simulations and have similar functions for describing the pairwise interaction, bond stretching, angle bending and dihedral torsion of such molecules.

3.1.3 Solving MD governing equation

To describe the evolution of a molecular system, it is required to solve the Newton's equation at each time step and determine the new positions of particles. One of the widely-adopted methods is the Verlet algorithm, that starts from a Taylor series expansion of the position **r** of the particle *i* at the time step t+Δt, that is expressed as:

$$\mathbf{r}_i(t+\Delta t)=\mathbf{r}_i(t)+\frac{d\mathbf{r}_i(t)}{dt}\Delta t+\frac{1}{2}\frac{d^2\mathbf{r}_i(t)}{dt^2}\Delta t^2+\frac{1}{6}\frac{d^2\mathbf{r}_i(t)}{dt^2}\Delta t^3+o(\Delta t^4) \quad \text{Eq. (3.5)}$$

where the quantity Δt is the time step and $o(\Delta t^4)$ presents terms of order 4 or higher in Δt.

Meanwhile, the equation for the particle's position at the time step t-Δt is given by:

$$\mathbf{r}_i(t-\Delta t)=\mathbf{r}_i(t)-\frac{d\mathbf{r}_i(t)}{dt}\Delta t+\frac{1}{2}\frac{d^2\mathbf{r}_i(t)}{dt^2}\Delta t^2-\frac{1}{6}\frac{d^2\mathbf{r}_i(t)}{dt^2}\Delta t^3+o(\Delta t^4) \quad \text{. Eq. (3.6)}$$

The summation of Eq. (3.5) and Eq. (3.6) is:

$$\mathbf{r}_i(t+\Delta t) \approx 2\mathbf{r}_i(t) - \mathbf{r}_i(t-\Delta t) + \frac{d^2\mathbf{r}_i(t)}{dt^2}\Delta t^2 = 2\mathbf{r}_i(t) - \mathbf{r}_i(t-\Delta t) + \frac{\mathbf{f}_i(t)}{m_i}\Delta t^2, \qquad \text{Eq. (3.7)}$$

where **f** is the force on the particle *i* and is also a function of positions of the particles. Therefore, the calculation of new positions of all particles can be obtained from their previous positions. Meanwhile, the velocity **v** of the particle *i* can be determined by

$$\mathbf{v}_i(t+\Delta t) = \frac{\mathbf{r}_i(t+\Delta t) - \mathbf{r}_i(t-\Delta t)}{2\Delta t}. \qquad \text{Eq. (3.8)}$$

The MD simulation always initiates with a random seed to provide a Maxwell-Boltzmann distribution of particles' velocities which fits the initial temperature of the system. Combined with the initial velocities of all the particles, the positions of all particles are updated by adjusting them into their new positions at each time step. The time step is normally chosen to be of the order of 0.5 femtosecond and depends on the atomic vibrations in the MD simulations. All simulations in this dissertation were performed with the large-scale atomic/molecular massively parallel simulator (LAMMPS) molecular dynamics package [49]. The limitation of the computational resource constrains the size of the simulation box and the number of atoms. Normally, a parallelized computer can deal with a simulation involving ~100,000 atoms and 30 nm^3 volume of the simulation box. It is still a very small size compared to the materials in a practical physical case. In addition, it inevitably introduces a strongly artificial boundary effect since a large portion of atoms in the simulation box are at the surface of the simulation box. In order to minimize the effects from the surface atoms, a periodic boundary condition is always applied. As illustrated in Figure 3-1, when an atom moves out through one side of the simulation box with a periodic boundary condition, it simultaneously moves in from the other side of the simulation box.

3.1.4 Molecular dynamics ensembles

The system properties in statistical mechanics are built from its microscopic states. Subject to the macroscopic constraints, three equilibrium ensembles, namely microcanonical (NVE), canonical (NVT) and isothermal-isobaric (NPT) are developed. An isolated system with a volume V, a total number of particles N, and a total energy of E is described as the NVE ensemble in which the constants of the volume, number of particles and energy is achieved by the Newton's equation of motion. The NVT is an ensemble with fixed number of particles, volume and temperature T. A thermostat is used in NVT simulations to keep the temperature at a specific value by adding several dynamic variables which are coupled to the particle velocities. The NPT ensemble maintains constant temperature, pressure and number of particles, which is useful to provide an equilibrium condition for the molecules. The NVT and NPT are performed in MD simulations by time integration of the Nosé-Hoover style non-Hamiltonian equations of motion[50].

3.1.5 Thermal transport

The calculation of the thermal conductivity is performed by using the non-equilibrium MD (NEMD) simulation. Through the Fourier's equation,

$$q = -\kappa \nabla T \quad , \qquad \text{Eq. (3.9)}$$

the thermal conductivity, κ, of the molecular system can be determined by the known constant heat flux, q, and the ensuing temperature gradient, ∇T, fitted from the temperature profile. The resulting temperature gradient in the simulation box is realized by exchanging a constant kinetic energy among the atoms in the regions of the heat sink and heat sources which are set at the center and two sides of the simulation box, respectively. As illustrated in Figure 3-2, a typical temperature profile of n-alkanes in an NEMD simulation is illustrated. A slight asymmetry of the temperature profile is observed in the figure even though the time averaged values have been considered. This asymmetry is originated from the size effect of the simulation box. In order to weaken this effect on the thermal conductivity of the mixture of n-alkanes, the thermal conductivities for different simulation box lengths (*L*) are calculated by using the NEMD method with the average of several ensembles. The values of the thermal conductivities corresponding to different simulation box lengths are then plotted as $1/k$ vs. $1/L$. Thus, the macroscopic thermal conductivity can be determined by extrapolating the values to $1/L = 0$. Considering the anisotropic effect on thermal conductivity, the thermal conductivity tensor of n-alkanes should be addressed. The details can be founded in the analysis of Ref. [51].

3.2 Phonon Boltzmann Transport Equation

Phonons, as the quanta of lattice thermal excitations, are the key thermal energy carriers in electronic insulators. The phonon Boltzmann transport equation (BTE) has gained some renewed interests as the default choice of the transport theory to predict the lattice thermal conductivity of crystalline solids because all the necessary inputs are readily derived from the first principles. The phonon BTE theory is valid within the phonon gas approximation such that each mode oscillates at a harmonic frequency, ω, at a thermal equilibrium and the ensemble-averaged number of phonons at this mode follows the Bose-Einstein distribution, i.e.

$$n_{eq}(\omega) = \langle n \rangle_{eq} = \frac{1}{e^{(\hbar\omega/k_B T)} - 1}, \qquad \text{Eq. (3.10)}$$

where $\hbar$ is the reduced Planck constant. In the presence of a constant temperature gradient ∇T, the phonon number n_α for $\alpha = 1, 2, \ldots, \mathrm{N}$, is deviated from $n_{eq,\,\alpha}$ as a result of thermal diffusion. At steady-state, the BTE for the phonon number at mode α is expressed by:

$$\mathbf{v}_\alpha \cdot \nabla n_\alpha = \left(\frac{dn_\alpha}{dt} \right)_{scattering} . \qquad \text{Eq. (3.11)}$$

The left-hand term stands for the phonon diffusion, where $\mathbf{v}_\alpha$ is the group velocity of mode α. The right-hand term is the scattering term, which includes the incidents of the phonon-phonon, phonon-electron, or phonon-defect scatterings. In addition, the phonon heat flux in *x*-direction, *q*, is calculated by considering the all phonon mode as:

$$q_x = \frac{1}{V} \sum_\alpha n_\alpha \hbar \omega_\alpha v_{\alpha,x} , \qquad \text{Eq. (3.12)}$$

where V is the crystal volume. Once Eq. (3.11) is solved using a linearized method, then combining with Eq. (3.9) and Eq. (3.12), the thermal conductivity tensor can be represented as:

$$\kappa_{IJ} = \sum_\alpha c_\alpha v_{\alpha IJ}{}^2 \tau_\alpha , \qquad \text{Eq. (3.13)}$$

where τ_α is the phonon lifetime and c_α is the specific heat of phonon, expressed by:

$$c_\alpha = \frac{dE_\alpha}{dT} = \hbar\omega_\alpha \frac{dn_{\alpha,eq}}{dT} = -\frac{\hbar\omega_\alpha}{k_B T^2} n_{\alpha,eq}(n_{\alpha,eq}+1) . \qquad \text{Eq. (3.14)}$$

Therefore, the calculation of the lattice thermal conductivity is directly linked to the phonon properties, which contains two parts: (1) the dispersion relation of phonons from the atomic force constant and (2) the scattering matrix from the perturbation theory.

3.2.1 Harmonic and anharmonic lattice dynamics

Because atoms of a solid vibrate around their respective equilibrium lattice points, the Taylor series expansion of its potential energy E_U around its equilibrium state can be expressed by:

$$\begin{aligned} E_U = E_{U_0} &+ \sum_i \sum_I \frac{\partial E_U}{\partial u_i^I} u_i^I + \frac{1}{2!} \sum_{i,j} \sum_{I,J} \frac{\partial^2 E_U}{\partial u_i^I \partial u_j^J} u_i^I u_j^J \\ &+ \frac{1}{3!} \sum_{i,j,k} \sum_{I,J,K} \frac{\partial^3 E_U}{\partial u_i^I \partial u_j^J \partial u_k^K} u_i^I u_j^J u_k^K + \cdots \end{aligned} , \qquad \text{Eq. (3.15)}$$

where *i*, *j* and *k* are indices of atoms and *I*, *J* and *K* present the Cartesian coordinates (*x*, *y* and *z*). E_{U_0} is the equilibrium potential energy and *u* is the small displacement of the atoms. The second- and third-order derivatives of the potential energy are known as the harmonic and cubic force constants. The first-order derivative is zero if all the atoms are at the equilibrium state. The first principles calculation based on density function theory are recently applied to obtain the equilibrium atomic position for the calculation for atomic force constants, which are available by software packages such as VASP [52] and quantum espresso [53].

3.2.2 Phonon-phonon scattering mechanism

The phonon scattering rate, $w_{i\to f}$, from the initial state *i* and final state *f*, for both scattering types is given by the Fermi golden rule as:

$$w_{i\to f} = \frac{2\pi}{\hbar} |\langle f \,|\, \Delta\hat{V} \,|\, i\rangle|^2 \, \delta(E_i - E_f) \quad , \qquad \text{Eq. (3.16)}$$

where $\Delta\hat{V}$ denotes the difference of the true lattice Hamiltonian and the harmonic lattice Hamiltonian.

In a perfect bulk non-metallic crystal, the $\Delta\hat{V}$ is the anharmonic potential expressed in Eq. (3.15). The lowest order anharmonic term in Eq. (3.15) is the 3rd order lattice anharmonic force constants, which lead to three-phonon interactions. This three-phonon interaction contributes the majority of incidents of the phonon-phonon scattering in many solids. As illustrated in Figure 3-3, three-phonon interactions have two types: (1) one phonon splits into two phonon modes or (2) two phonons combine to form one phonon. Both transitions require conservation energy, $\hbar\omega$, and momentum, $\hbar\mathbf{q}$, of phonons, thus:

$$\mathbf{q}_\alpha = \mathbf{q}_\beta + \mathbf{q}_\gamma + \mathbf{G} \text{ and } \omega_\alpha = \omega_\beta + \omega_\gamma \quad \text{(type 1),} \qquad \text{Eq. (3.17)}$$

$$\mathbf{q}_\alpha + \mathbf{q}_\beta = \mathbf{q}_\gamma + \mathbf{G} \text{ and } \omega_\alpha + \omega_\beta = \omega_\gamma \quad \text{(type 2),} \qquad \text{Eq. (3.18)}$$

where **G** is the reciprocal lattice vector or zero vector, corresponding to an Umklapp process or a normal process, respectively.

Quantitative evaluation of all the possible configurations of three-phonon scattering events described in Equations Eq. (3.17) and Eq. (3.18) requires a large amount of computational resource, i.e. CPU time and RAM memories. Fortunately, a couple of efficient implementations, such as ShengBTE [54] or phonon3py [55], have been developed to allow users to compute the lattice thermal conductivity of a crystal using only first-principles calculated harmonic force constants and 3rd order anharmonic force constants, i.e. without any adjustable parameters. A workflow for thermal conductivity calculation is illustrated Figure 3-4.

3.3 Post-processing

The post-processing of the simulated data (summation of individual atomistic heat currents, autocorrelations of individual atomistic velocities and time-series analyses of coupling-decoupling processes, etc.) in this dissertation is mainly performed by utilizing the Python opensource programing language (version 3.6.5). The matrix calculations and data manipulations reported here relied on the NumPY package. It is generally believed that the Python language provides a more convenient and flexible post-processing platform compared to other alternatives.

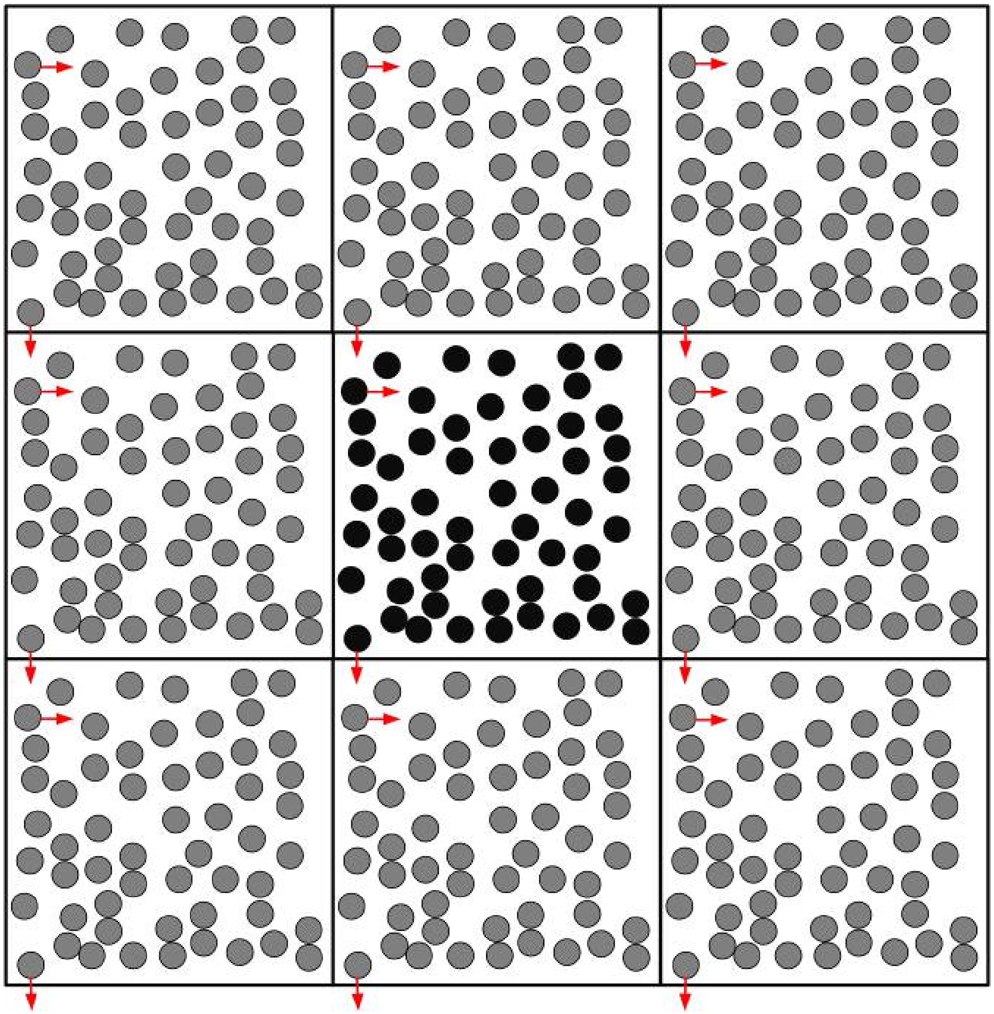

Figure 3-1 Illustration of a two-dimensional MD simulation box containing black points (molecules) incorporating periodic boundary condition on four sides. The gray points are the virtual images of the black ones.

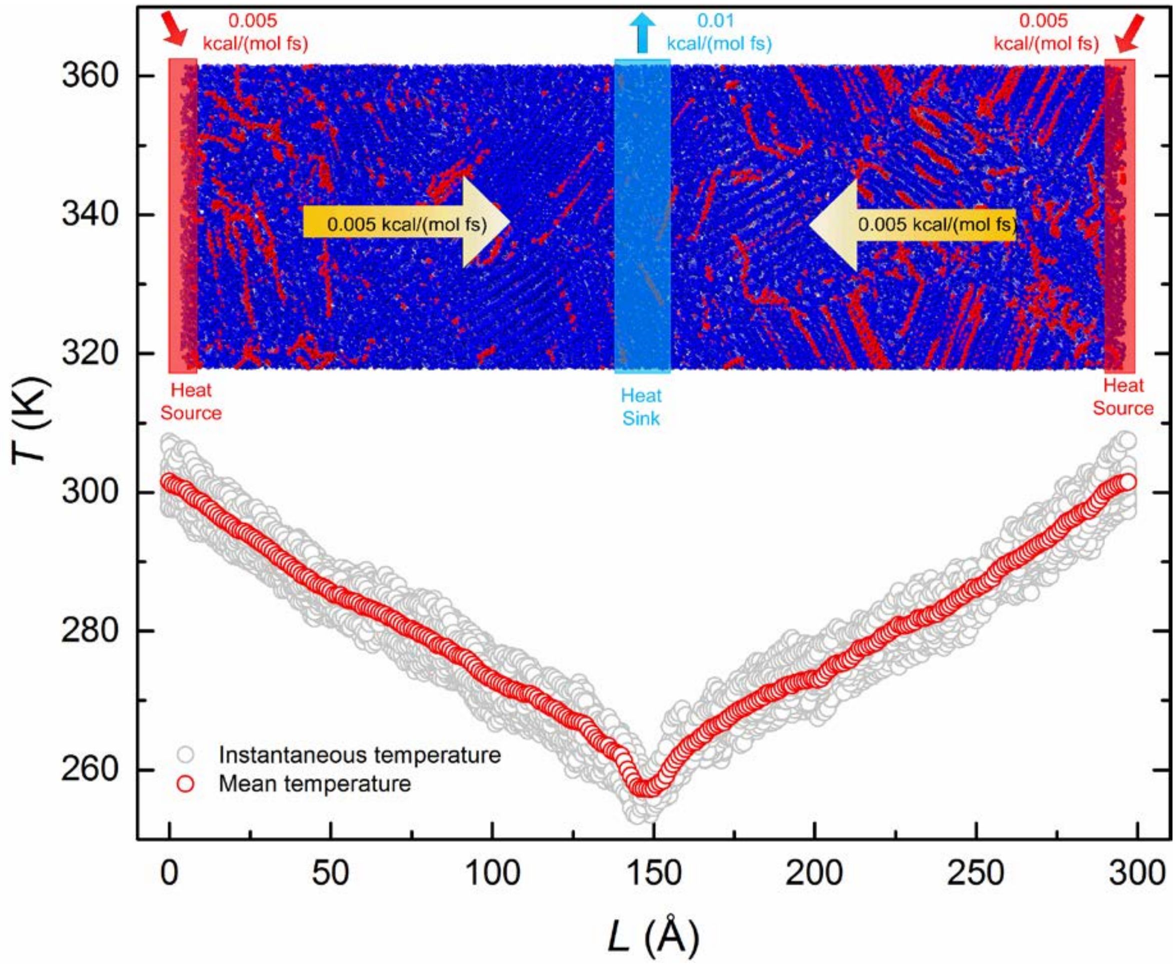

Figure 3-2 A typical temperature distribution of n-alkanes in an NEMD simulation with an exchange rate of 0.01 kcal/(mol K) between the heat source and sink.

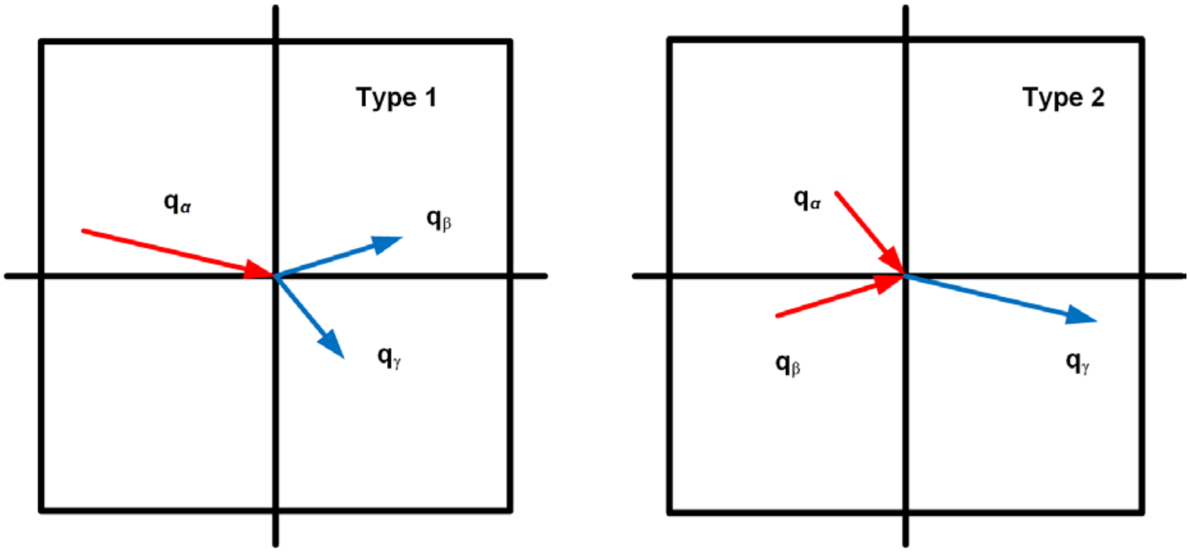

Figure 3-3 Schematic diagrams of two types of three-phonon scattering processes within a crystalline solid

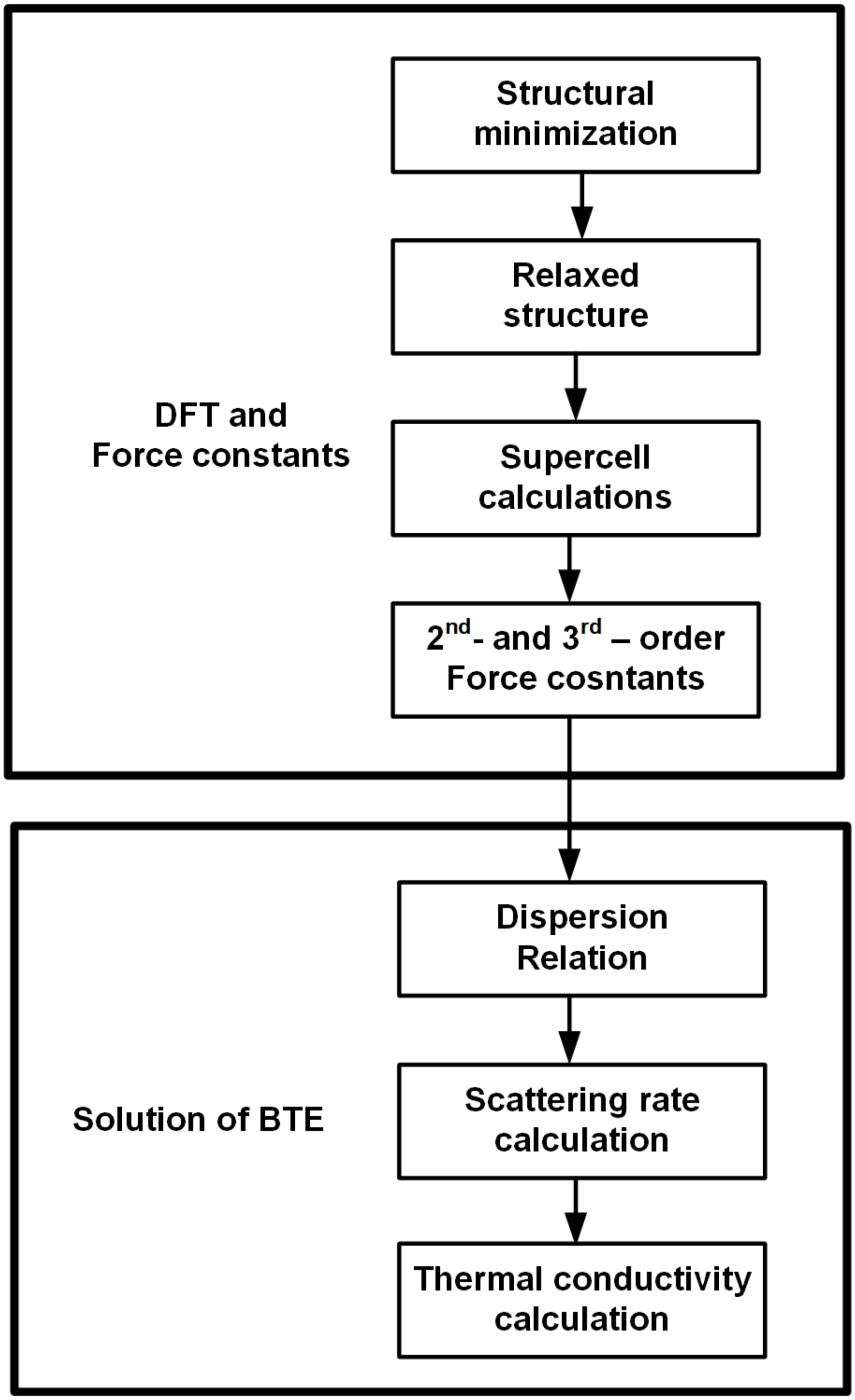

Figure 3-4 Workflow for thermal conductivity calculation from the density function theory (DFT) to the Boltzmann transport equation (BTE)

Chapter 4 Thermal Transport of the Mixture of Long-Chain N-Alkanes

In this chapter, the crystallization processes of a binary n-alkane mixtures based on the free surface and the imposed surface potential are firstly conducted. The thermal conductivity of the mixture is then evaluated and analyzed in relation to the orientation factor and the solid ratio of the mixtures.

4.1 Methods

4.1.1 Molecular system and cooling method

In this work, all the MD simulations are performed utilizing LAMMPS. As listed in Table 4-1, the simulation box contains a total number of 1200 n-alkane molecules, a combination of n-eicosane (C20) and n-triacontane (C30), at different values of the number ratio of C30 (n_{C30}). The united-atoms potential is applied to describe the n-alkanes' molecules interaction instead of the all-atoms model due to limited contribution from the high-frequency vibration C-H bond to the macroscopic heat conduction flux. The methylene group ($-CH_2-$) and the methyl group (CH_3-) are treated as the interaction site in the united-atoms potential. The intramolecular bonding, angular and dihedral interactions are described by the NERD (after the authors' names) force field [48]. The summary of the pertinent *LJ* parameters is listed in Table 4-2. In addition, considering the rapid decrease of the van der Waals force with the interatomic spacing increasing, a cut-off length is applied to reduce the required calculations in the MD simulations. This nonbonded interaction potential is calculated by the Lennard-Jones (*LJ*) potential with a 10 Å (~2.5 σ) cut-off distance. The summary of the pertinent *LJ* parameters is listed in Table 4-3.

In MD simulation, the cooling processes (i) on the free surface and (ii) through imposition of the surface potential can be considered as two limiting crystallization schemes due to the marked discrepancy on the structure of the ensuing crystallized n-alkane mixture. The n-alkane mixture is crystallized isotropically on the free surface from a liquid phase to a solid phase. The molecular system is cooled under the isothermal-isobaric ensemble (*NPT*) conditions with the periodic boundary condition applied in all three directions.

In presence of an imposed surface potential, the periodic boundary condition cannot be applied to all three directions. As illustrated in Figure 4-1, an attractive substance modeled by a virtual *LJ* potential is introduced on the bottom surface of the simulation box, while the periodic boundary conditions are applied in the *x*- and *y*-directions. In comparison to the ε value of the *LJ* potential between molecules, a much greater value of $\varepsilon_{surface}$ is assumed to form a relatively strong attractive potential well. In order to minimize the ensuing effect on thermalization of the system, all the molecules are initially placed above the finite distance $\sigma_{surface}$ from the *LJ* well and a 5 Å cut-off distance of this potential is set to make sure that this potential can only interact with the bottom-most molecules. A repulsive wall is set on the top surface of the simulation box to prevent the escape of molecules during the simulation. The canonical ensemble (*NVT*) are conducted for the cooling processes of the n-alkanes mixture with the imposed surface potential approach. Both cooling methods are run at a cooling rate 1 K/ns. The value of the time step used in numerical integration of the governing equations was 0.5 fs in all simulations.

4.1.2 Calculation of the thermal conductivity

The calculation of the thermal conductivity of the n-alkanes mixture is conducted by using the non-equilibrium MD (NEMD) simulation and following the method outlined in Section 3.1.5. The resulting temperature gradient in the simulation box is realized by exchanging a constant kinetic energy (0.01 kcal/(mol fs)) between the atoms in the regions of the heat sink and heat sources which are set in the center and two sides of the simulation box, respectively. The solid structure crystallized from the liquid phase is firstly equilibrated under *NPT* at 270 K and atmospheric pressure for 3 ns (6 million steps). The molecular system is then applied the heat flux under microcanonical ensemble (*NVE*) for 3 ns (6 million steps) to reach the steady-state. The mean temperature profile is averaged for another 2 ns (4 million steps) of simulation. In order to weaken the simulation box length dependence of the thermal conductivity of the mixture of n-alkanes, the thermal conductivities of the mixture n-alkanes for different simulation box lengths (L) are calculated by using the NEMD method. Computed values of the thermal conductivities corresponding to different simulation box lengths are plotted as $1/k$ vs. $1/L$. The macroscopic thermal conductivity can then be determined by extrapolating the values to $1/L = 0$.

4.1.3 Orientation factor and the solid ratio

Due to the randomness of the distribution of the orientation of the molecular chains, an "orientation factor" is defined to quantify the whole molecular system's orientation,

$$S = \langle | \cos(\theta_i) | \rangle, \qquad \text{Eq. (4.1)}$$

where θ_i is the angle between the end-to-end vector of each individual molecule i and the heat flux direction with | | indicating the absolute value and ⟨ ⟩ standing for the ensemble average for all the molecules (Figure 4-2).

The orientation factor can be used to analyze the collective effect of the whole molecular system's orientation on the value of thermal conductivity. In addition, a crystallization criterion determined by the ratio of end-to-end distance over the fully-stretched length is defined to provide a quantitative measure of the solid morphology [22]. For a single n-alkane chain, if the ratio between the end-to-end distance and full-stretched length is greater than 0.9, it is defined as a straight molecule (all-trans-conformation) and is crystallized. Moreover, a crystallized chain must be found in a bundle with a minimum 3 nearby straight chains. The "solid ratio" representing crystallinity is calculated simply as the ratio of the number of straight molecule over the number of all molecules.

4.2 Results and Discussion

4.2.1 Phase diagram of the n-alkane mixture

As illustrated in Figure 4-3, the reduced nonbounded potential energy of n-alkane mixtures at different n_{C30} is changing with temperature. Each data point is averaged from 10 million steps (5 ns). It is shown clearly that n-alkane mixtures exhibit a reduction of the degree of supercooling during crystallization following the *imposed* surface potential route. In effect, the existence of the imposed surface potential acting as a nucleation plane decreases the energy barrier for crystallization. In Figure 4-4, several snapshots of the solid molecules during respective crystallization schemes are presented to illustrate the instantaneous state of the molecular systems following the free surface and the surface potential routes. As illustrated in Figure 4-4 (a) for the free surface approach, the onset of solidification is visible as seen at three sites of the simulation box when small molecular blocks are formed by several solid n-alkanes aggregating and pointing in the same direction. This is followed by more solid molecules starting to aggregate on the initially-formed molecular blocks and the size of the molecular blocks increases. In effect, several molecular blocks aligned in different directions are formed in the simulation box as the temperature goes down slowly. When the temperature of the molecular system reaches to the target cooling temperature, a solid n-alkanes mixture is formed with a certain orientation factor. In Figure 4-4 (b), the evolution of the mixture in response to the imposed surface potential route during the crystallization processes is presented. At early time instant of the top row, several molecules form a recognizable lamellar structure and are constrained within a small distance from the bottom surface due to the strongly attractive potential well. Gradually, the molecules of C20 and C30 “join” on the lamellar structure and the lamella structure grows. The final structures ensuing from the free surface and imposed surface potential routes shown on the bottom rows of Figure 4-4 are distinctly different.

The values of the orientation factor of the molecular systems crystallized following both routes are illustrated in Figure 4-5. There is a clear discrepancy of the values of the orientation factors following these two cases. The surface potential treatment forces the molecules “laying down” and orienting randomly in the horizontal direction on the *x*-*y* planes. As a result of the existence of the imposed surface potential during crystallization of the mixtures, the orientation factor of the molecular system should be close to zero in the *z*-direction. The values being around 0.1 are the result of incomplete stretching for several molecules. With the free surface treatment of the system, the values of the orientation factor of each molecular block in an infinitely large simulation box should be equally distributed due to the stochasticity of the formation of the initial molecular bulks. Hence, the ensemble average orientation factor in an n-alkane molecular system is equal to 0.5.

During freezing, the solid ratio is increasing as cooling proceeds (Figure 4-6). The solid ratio of the n-alkane exhibits rapid rising trend when it is cooled from 310 K to 280 K following the imposed surface potential route, illustrating crystallization of the mixture from a liquid phase to a solid phase. However, after the temperature reaches 280 K, the solid ratio of the mixture is kept around 0.75 although the temperature keeps decreasing to 240 K. Following the free surface approach, crystallization process mainly happens in the range 275 K to 260 K and a lower solid ratio is formed in the final structure.

4.2.2 Thermal conductivity of the n-alkanes mixtures

As illustrated in Figure 4-7, the inverse of the thermal conductivity of the molecular system is plotted against the inverse of the simulation box length in the imposed heat flux direction (z-direction). The extrapolation of these values to $1/L = 0$ gives the macroscopic thermal conductivity with the consideration of the size of the simulation box. In the meantime, the orientation factor is extracted from the final structure of the molecular systems. Since the mobility of molecular chains at 270 K is higher than that at the lower temperature, the orientation factors of the n-alkane mixtures while performing the calculation of thermal conductivity are higher than the mixture for the same n_{C30} system crystallized immediately from the liquid phase. In addition, replication of the simulation box during performing the calculation of thermal conductivity provides extra space in the z-direction for the cases crystallized following the imposed surface potential approach, which leads to an extra increase of the orientation factor. The macroscopic thermal conductivities of the n-alkane mixtures for different values of n_{C30} are illustrated as a function of the orientation factor in Figure 4-8. It is clearly observed that the orientation factor is still the main contribution to the values of the thermal conductivity of the molecular system over the wide range of the number ratio of C30 covered. Higher orientation factor in a system always leads to a high thermal conductivity of the n-alkane mixture, being consistent with the findings for molecular system of pure n-alkanes of ideal crystals. The thermal conductivity of the pure n-alkane ideal crystal systems, e.g. C20 and C30, [65] are also included in Figure 4-8. The single crystal system of the pure n-alkanes can provide molecular structures with the maximum and minimum orientation factors by replicating the molecular structure in a certain direction. The differences in the thermal conductivities reflect the geometrical characteristics of intermolecular interactions occurring in individual single crystals. The combination of the weak van der Waals force between the methylene groups in adjoin molecules and the low packing density on the plane transverse to the direction of molecular chains in the crystal, exhibiting a low thermal interfacial conductance, accounts for the small value of the thermal conductivity transverse to the direction of molecular chains. Along the molecular chain axis, although similar weak van der Walls forces are responsible for the methyl group layer between molecular blocks, the much longer molecular dimension in the chain direction markedly decreases the number of the thermal interfaces, allowing fewer sites of weak interaction per unit length to occur than for the transverse direction. This anisotropic property of single crystal provides the theoretical highest and lowest thermal conductivities attainable.

Difference of thermal conductivity between the n-alkane mixtures with small orientation value (~0.1) and the stacked lamellae suggests that the solid ratio of the molecular system also plays an important role on thermal transport. The n-alkane mixtures crystallized following the imposed surface potential route have low solid ratio value even though they are at low temperature, suggesting that not all the molecules are in the fully-stretched form and contributing to thermal transport while the molecular system is in the solid state. These folded chains, being in a liquid-like state, mainly reside in the small regions between the stacked lamellae structures in the n-alkanes mixtures crystallized following the free surface approach (Figure 4-9). The stacked lamellas, based on the initial fully-stretched molecules, are growing as temperature is lowered. Therefore, the molecules in the regions between those stacked lamellas have a probability to be constrained from becoming fully-stretched due to the low mobility of these chains at low temperatures. These folded chains locally restrain thermal transport across the interface between the stacked lamella structures and increase the number of the effective thermal interfaces of the entire system.

4.3 Conclusions

In summary, the effect of the morphology of the n-alkane mixtures at different n_{C30} on their thermal conductivity are studied by performing MD simulations. The n-alkane mixtures are crystallized from liquid phase to solid phase following the free surface and the imposed potential surface routes. Comparing to the random ordering of molecular chains resulting from the free surface approach during crystallization, a dominant layering of molecules can be observed for the system undergoing freezing following the imposed potential surface route. Determination of thermal conductivity based on those solid structures of the n-alkane mixtures suggests the strong correlation between the orientation factor and the thermal conductivity of the mixtures but a negligible influence of the number ratio of C30 on thermal conductivity of the mixtures. In addition, the solid ratio also plays a significant role on the thermal conductivity of n-alkane mixtures with small orientation factor values by adjusting the number of thermal interfaces of the entire molecular system.

Table 4-1 Details of the n-alkanes mixtures at different number ratio of C30 (n_{C30})

n_{C30}	C20	C30
0	1200	0
0.17	1000	200
0.33	800	400
0.5	600	600
0.67	400	800
0.83	200	1000
1	0	1200

Table 4-2 Summary of the NERD united atom potential parameters

Interaction	Form	Parameters
Bond	$\frac{U(r)}{k_B}=\frac{K_r}{2}(r-b_{eq})^2$	K_r = 96,500 K/Å^2 b_{eq} = 1.53 Å
Angle	$\frac{U(\theta)}{k_B}=\frac{K_\theta}{2}(\theta-\theta_{eq})^2$	K_θ= 62,500 K/rad^2 θ_{eq} = 114°
Torsional	$\frac{U(\phi)}{k_B}=U_1(1+\cos\phi)+U_2(1+\cos 2\phi)+U_3(1+\cos 3\phi)$	

b_{eq}: Equilibrium bond length

k_B: The Boltzmann constant 1.3781×10^{-23} J/K

r: Distance between atoms

θ_{eq}: Equilibrium angle

θ: Bond angle

ψ: Torsional angle

Table 4-3 Parameters of the Lennard-Jones model for various pair potentials

Interaction	Form	Parameters	
Nonbonded	$U(r) = 4\varepsilon\left[\left(\frac{\sigma}{r}\right)^{12} - \left(\frac{\sigma}{r}\right)^{6}\right]$	$CH_2 – CH_2$	ε = 0.0907 kcal/mol σ = 3.93 Å
		$CH_3 – CH_3$	ε = 0.2059 kcal/mol σ = 3.91 Å
		$CH_3 – CH_2$	$\varepsilon = (\varepsilon_{\mathrm{CH_2}} + \varepsilon_{\mathrm{CH_3}})^{1/2}$ $\sigma = \frac{\sigma_{\mathrm{CH_2}} + \sigma_{\mathrm{CH_3}}}{2}$
Surface Potential	$U_{\mathrm{surface}}(r) = 4\varepsilon_{\mathrm{surface}}\left[\left(\frac{\sigma_{\mathrm{surface}}}{r}\right)^{12} - \left(\frac{\sigma_{\mathrm{surface}}}{r}\right)^{6}\right]$		$\varepsilon_{\mathrm{surface}}$ = 10 kcal/mol $\sigma_{\mathrm{surface}}$ = 3 Å

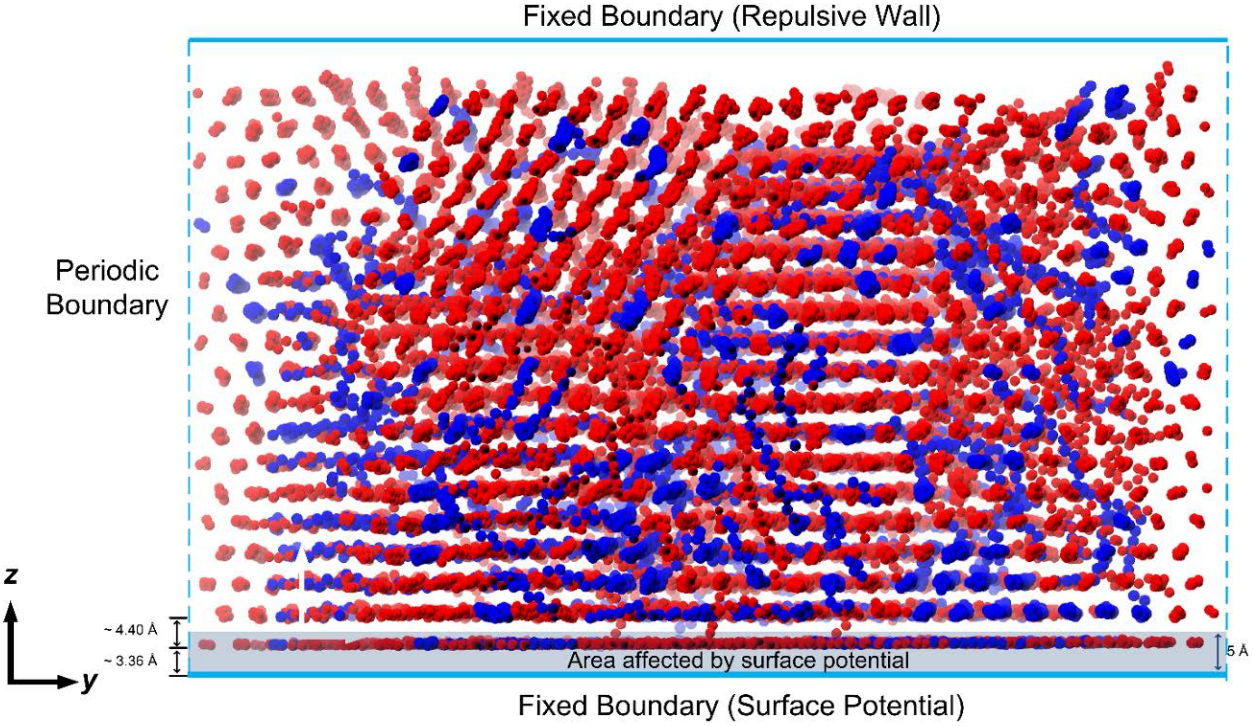

Figure 4-1 Schematic diagram of the molecular system cooling on the surface potential (*z* = constant). The periodic boundary condition is applied in the *x*- and *y*-directions. A potential well acting as an attractive substance is set on the bottom of the simulation box and a repulsive wall is set on the top. (Red and blue spheres represent the C20 and C30 atoms, respectively)

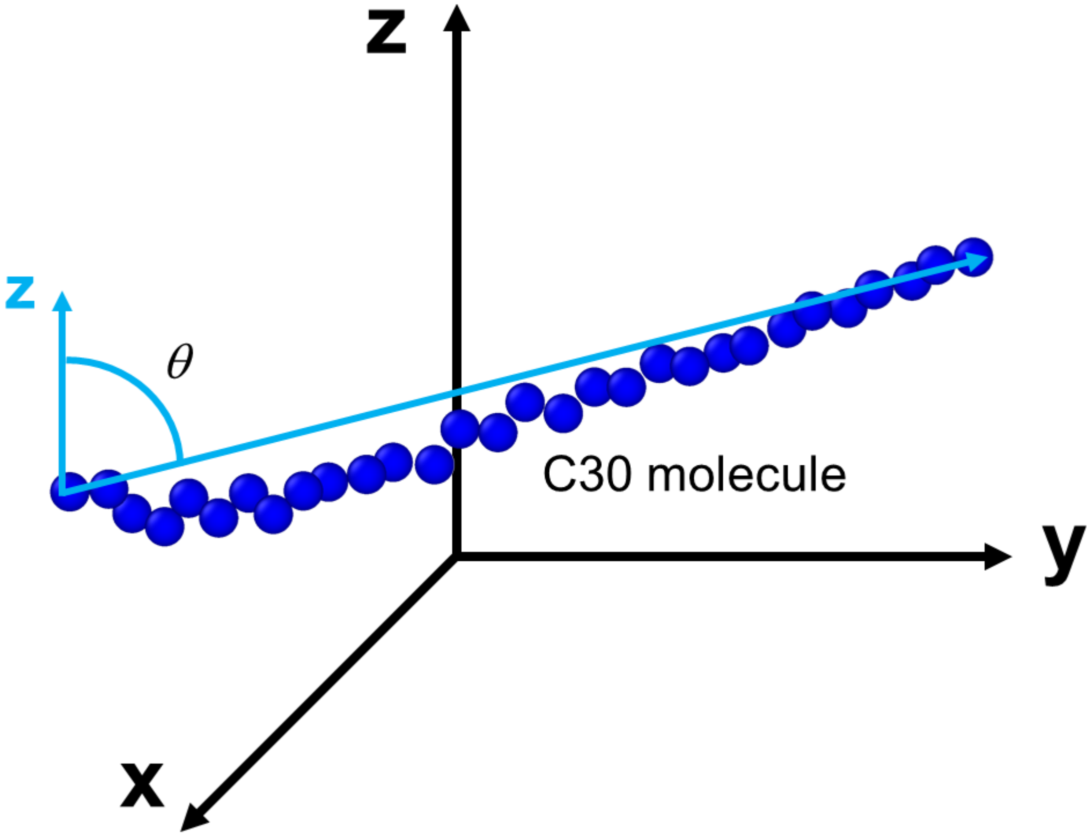

Figure 4-2 Schematic diagram of the end-to-end vector angle for a single molecule used in determining the orientation factor

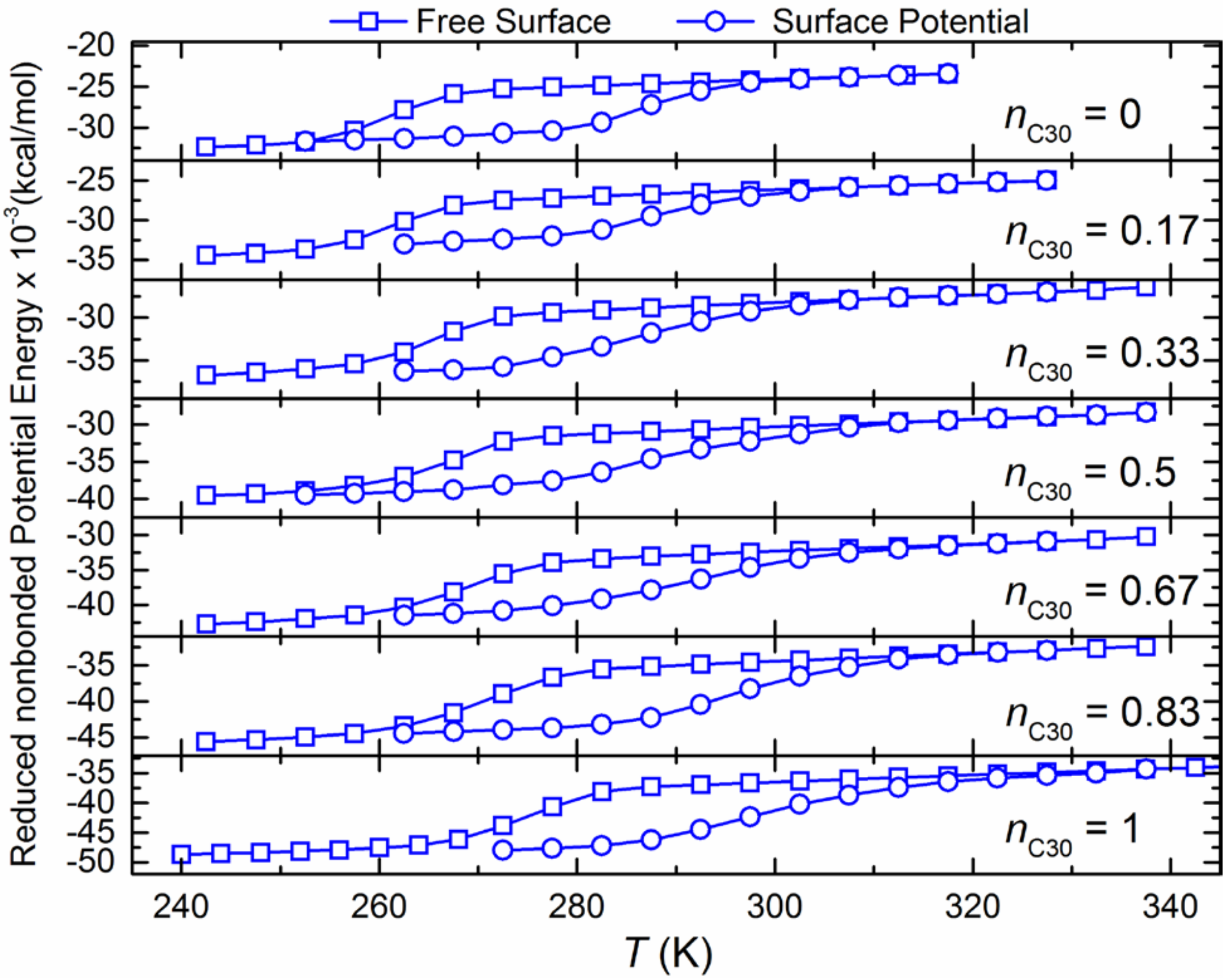

Figure 4-3 The reduced nonbonded potential energy of the n-alkane mixtures at different n_{C30} following the imposed surface potential and the free surface schemes during cooling processes (1 K/ns) from the liquid phase to the respective solid phase.

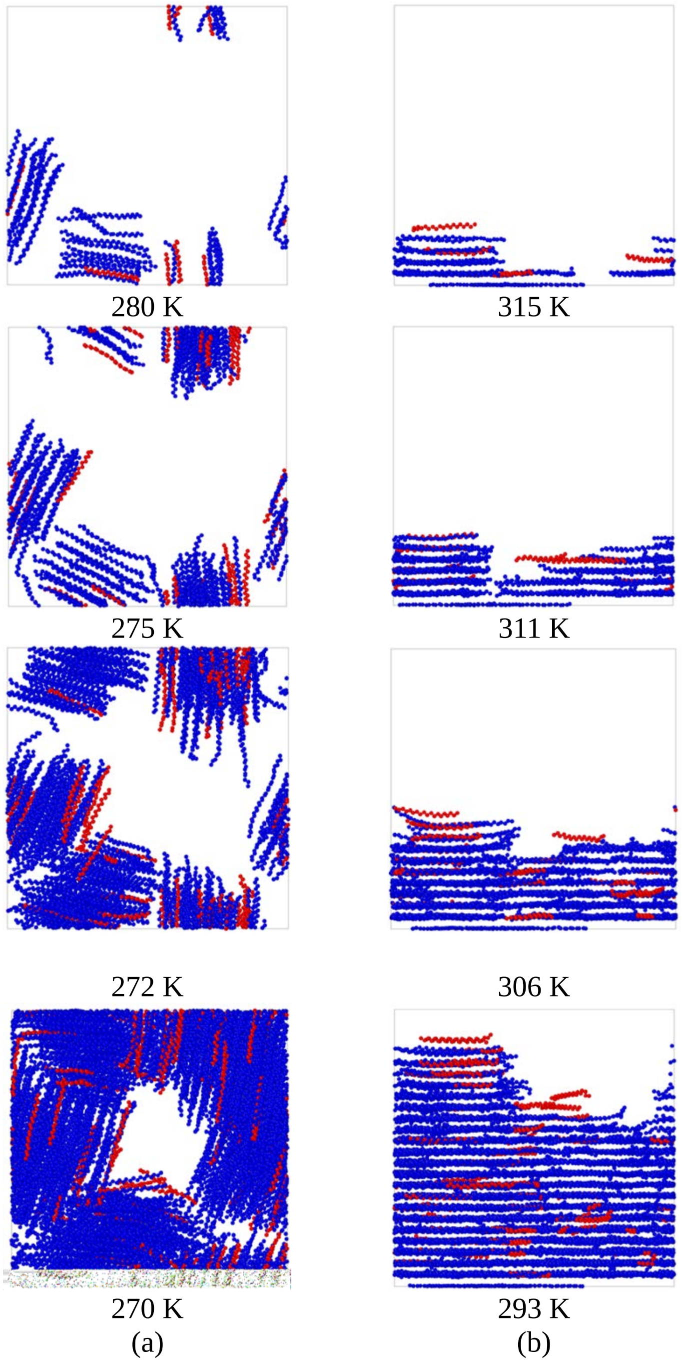

Figure 4-4 Snapshots of the n-alkanes mixtures ($n_{C30} = 0.83$) during the cooling processes following (a) the free surface and (b) the imposed surface potential. (C20 is represented by red spheres and C30 is represented by blue spheres)

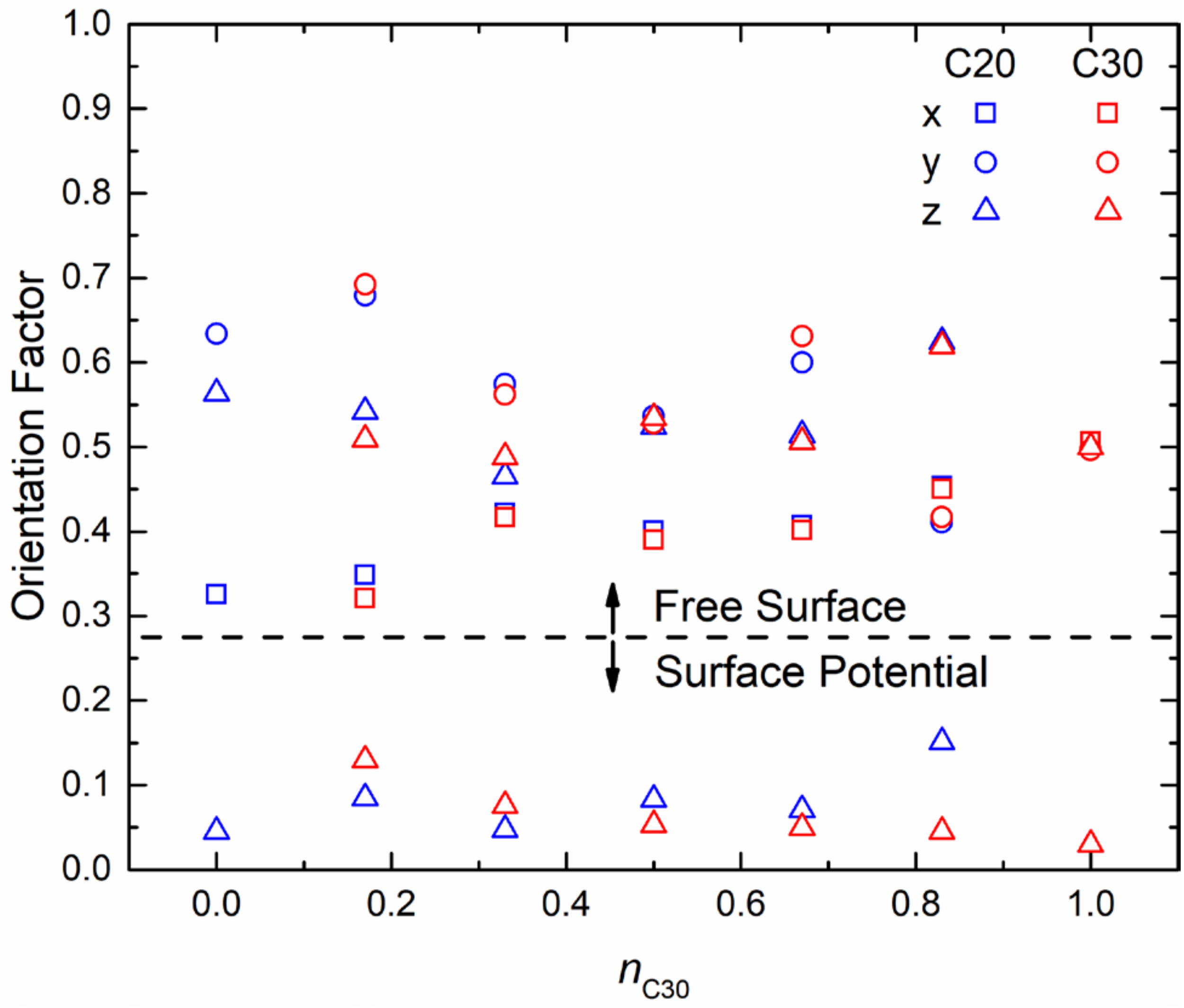

Figure 4-5 Orientation factor of each component in the n-alkane mixture resulting from the free surface and the imposed surface potential routes. (Only the orientation factor in the *z*-direction are presented for the cases with the imposed surface potential)

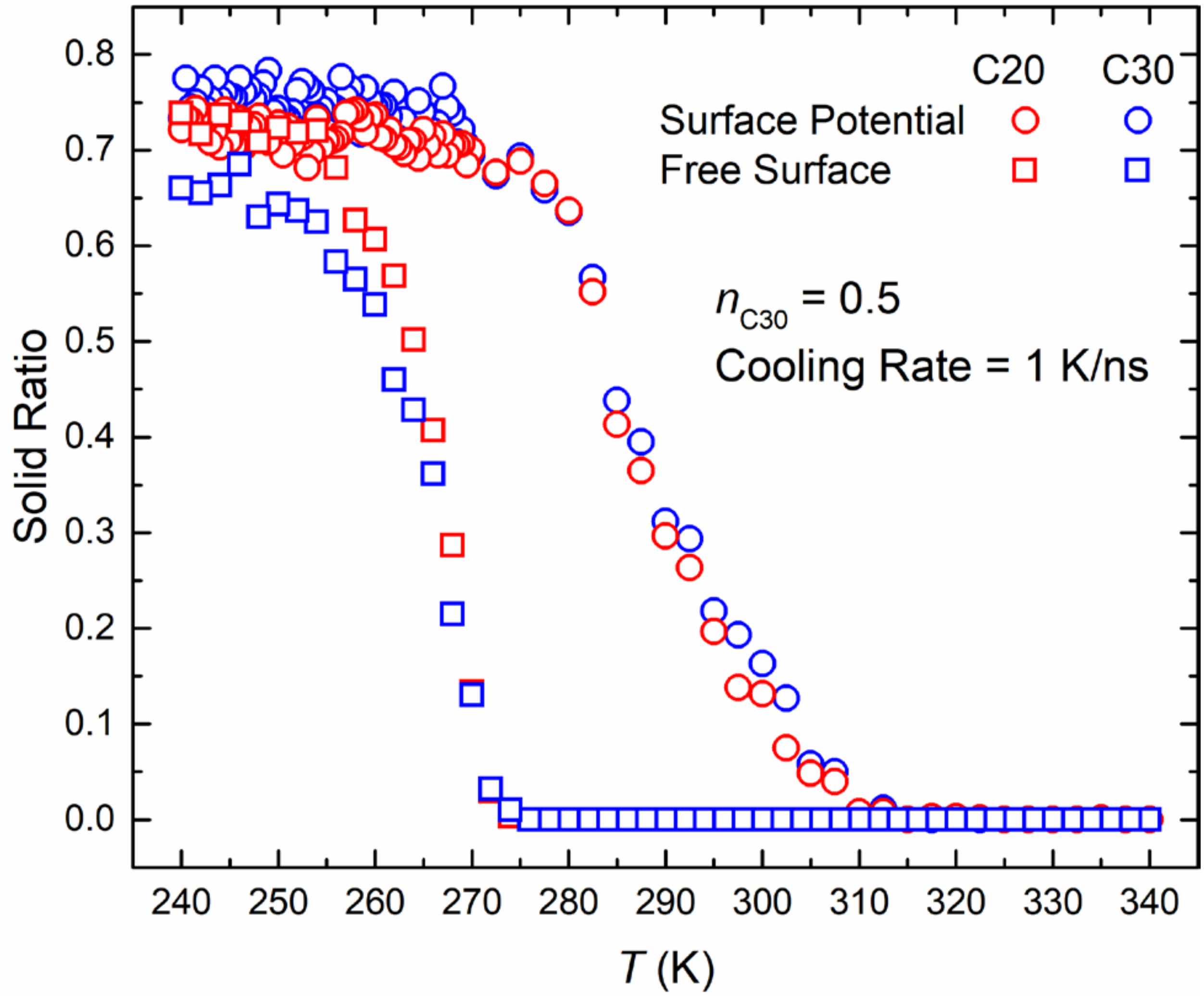

Figure 4-6 Solid ratio of the n-alkane mixture (n_{C30} = 0.5) during cooling process (1 K/ns) following the free surface and the imposed surface potential routes

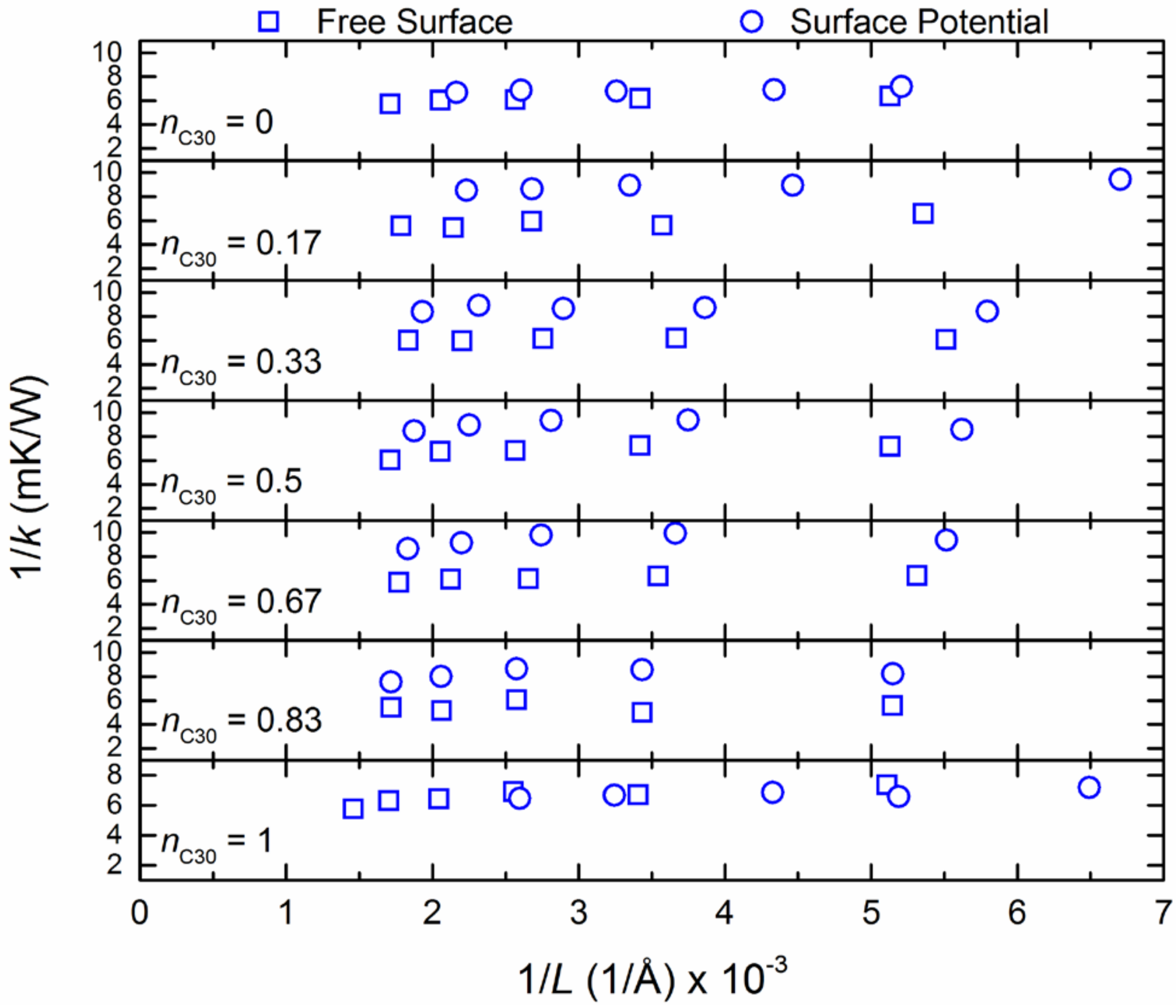

Figure 4-7 Inverse of the thermal conductivity in the *z*-direction versus inverse of the multiple lengths of stacked layers for the n-alkane mixture in the solid phase crystallized following the free surface and the imposed potential surface approaches.

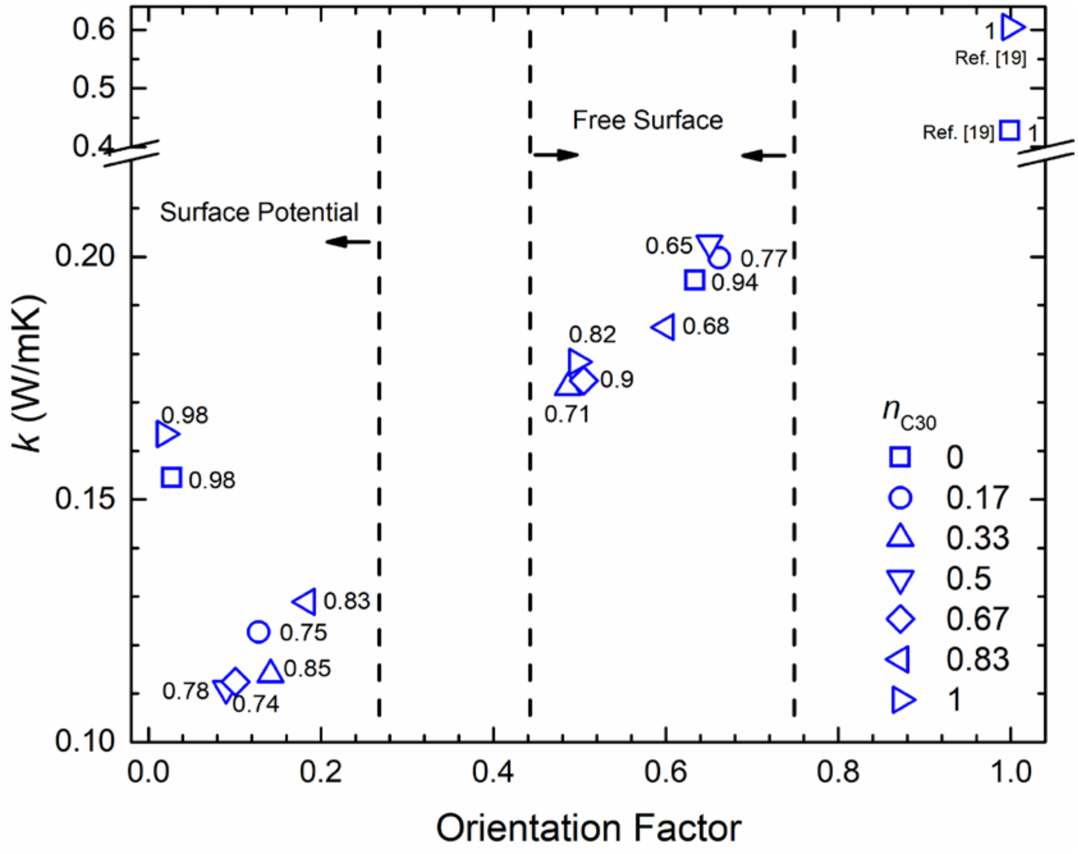

Figure 4-8 Correlation between the orientation factor and the thermal conductivity of the n-alkane mixtures at different n_{C30} (solid ratio of each case is labelled next to each symbol)

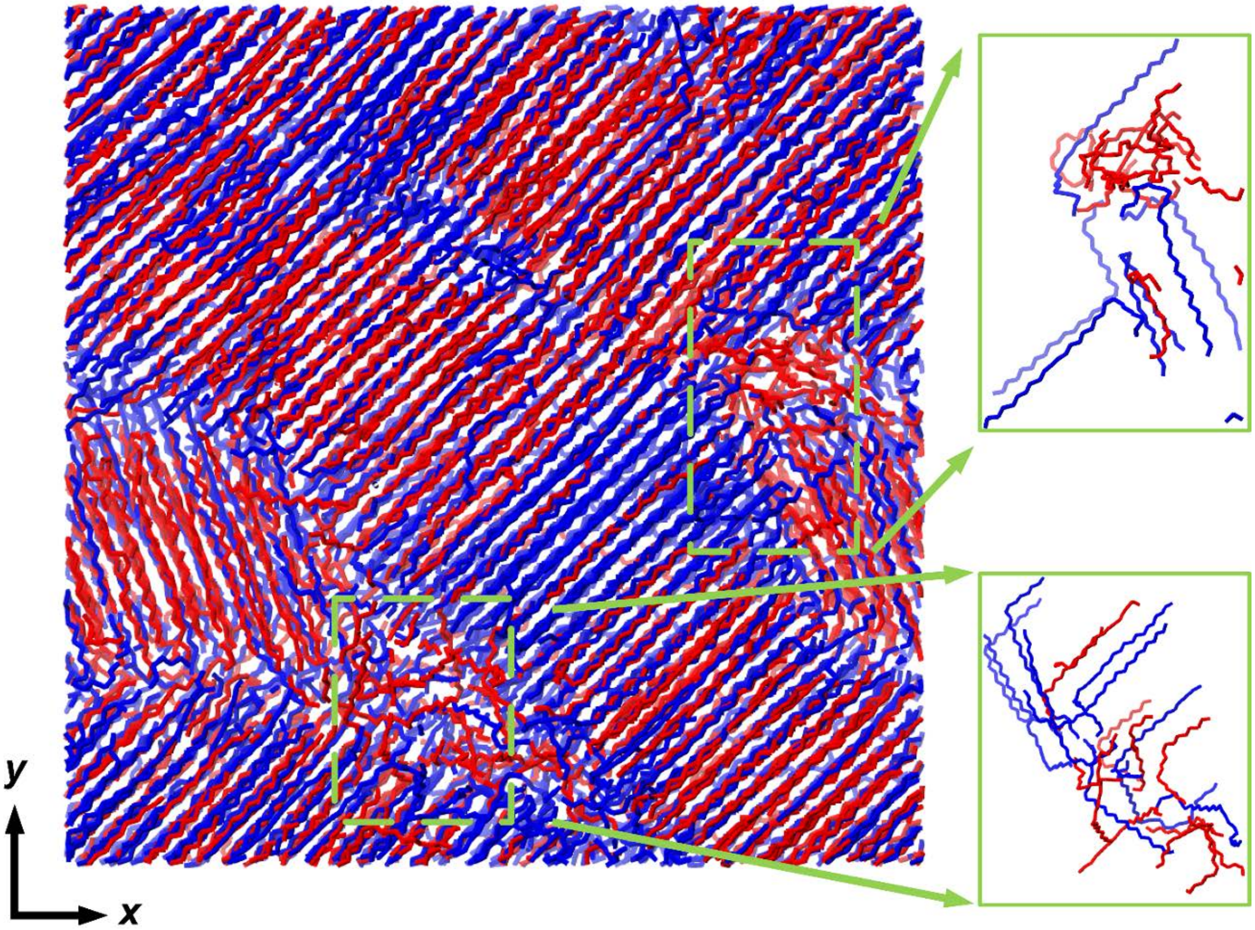

Figure 4-9 A top view of the n-alkane mixtures

(the blue lines represent the C30 molecules and the red lines represent the C20 molecules; the green boxes are regions where the molecules are folded)

Chapter 5 Thermal Coupling-Decoupling Mechanism

Due to the difficulty in direct measurement/observation of temperature distribution and/or heat fluxes at the nano-meter scale [56], molecular dynamics (MD) simulations have been applied to provide non-continuum theoretical models to understand structural, dynamical, and heat transfer properties. In particular, non-equilibrium MD (NEMD) techniques have been widely adopted to directly evaluate TIC (G_k), namely the ratio of the imposed net heat flux density (q) and the simulated temperature jump across an interface (ΔT): $G_k = q/\Delta T$ [58][59][60][61][62][63][64][65][66]. The values of TIC depend on the interface morphology, which is sensitive to specific synthesis and processing conditions. Motivated by a recent study [30], suggesting that some nano-fillers may lead to formation of partially-ordered structures by arranging all molecules in one direction during crystallization and reported experimentally-processed single crystal of n-eicosane (Figure 5-1 [67]), an ideal n-eicosane crystal model with perfectly-aligned molecules at the interfaces [65] has been extended to evaluate the upper limit of κ in n-alkanes in particular and soft-materials in general. In this chapter, the concept of ideal n-eicosane crystals is adopted to model the molecular structures of n-eicosane using super-cell systems with 10 molecular blocks (154 molecules each) orderly-aligned along the x-direction. Identical to the previous chapter, MD simulations are carried out with the LAMMPS package at the level of "united atoms" (UA) approximation, and with the NERD type of force field potential and the Lennard-Jones (LJ) potential for the intra- and inter-molecular forces, respectively.

5.1 Molecular Structure Details

The molecular structures of solid n-eicosane are simulated using super-cell models of the size of ten molecular blocks. Each molecular block consists of 154 n-eicosane molecules closely-packed on the y-z plane, and these 154-molecule blocks (with the periodic boundary conditions on the *y*-*z* plane) are aligned along the *x*-direction to form a crystal. These molecular blocks are labeled as blocks I, II, III and so on, with the last (right-most) block connected to the first block (the left-most) block through the periodic boundary condition of a super-cell model.

The MD time step was set as 0.5 fs. The systems were initially equilibrated under isothermal-isobaric ensemble (NPT) using the Nose-Hoover method at 1 atmosphere pressure and four different temperature points, i.e. 150 K, 200 K, 250 K and 300 K for 10 million steps (5 ns). Then, an NEMD simulation algorithm is adopted to impose transfer of kinetic energy from the heat sink to the heat source at the rate of 0.01 kcal/mol/fs for 10 million steps (5 ns) to simulate molecular configurations under the steady-state condition. Data at thermal equilibrium were collected from averaging every 20 steps (10 fs) for 1 million steps (0.5 ns) under micro-canonical ensemble (NVE). The temperature profiles under the steady-state condition were evaluated from the last 5 million steps.

Figure 5-2 illustrates a snapshot of the atomistic structure of the simulated n-eicosane crystal thermally equilibrated at 1 atmosphere pressure and 150 K temperature. Each n-eicosane molecule chain consists of 18 methyl ($–CH_2–$) UAs (shown as gray solid balls) and 2 methylene ($CH_3–$) UAs (shown as red solid balls). We label all the UAs in each chain from 1 to 20 based on their position (i.e. labels 1 and 20 for a methylene and 2-19 for a methyl). The atom-atom bond lengths are found to be temperature-independent, with the average value of one bond around 1.53 Å. Thermal fluctuation in bond lengths is also small, i.e. a standard deviation of the bond length was of the order 10^{-3} Å. At the same time, the thermal excitations are noticeable in the forms of collective translation and bond bending/twisting. We highlight two characteristic lengths, the interfacial/inter-block gap distance, $l_{\text{interface}}$, and the "end-to-end" molecular chain length, l_{molecule}.

The theoretical temperature dependence of the average values of $l_{\text{interface}}$ and l_{molecule} are shown in Figure 5-3. The MD-simulated interfacial gap length between two neighboring molecular blocks $l_{\text{interface}}$ first increases steadily from around 3.4 Å at 150 K to 3.7 Å at 250 K, and then rapidly increases beyond 260 K, exhibiting signs of melting. The magnitude of $l_{\text{interface}}$ is consistent with many length scales associated with weak vdW type of bonding in carbon-based solids. For example, in graphite, the interlayer distance between two graphene sheets in graphite is also of the order of 3.4 Å. However, the nearly 10% increase in $l_{\text{interface}}$ from 150 K to 250 K is rather unusual in any solid material. This unusual large temperature dependence of $l_{\text{interface}}$ correlates with the inverse temperature dependence of l_{molecule}. The thermal excitations related to the bond angle bending motion typically only add a broadening of l_{molecule} around its mean value, but do not significantly alter the mean value of l_{molecule}. The inverse temperature dependence of l_{molecule} is found to be caused by the enhanced curving and twisting of nano-meter long molecular chains at the elevated temperatures. It is obvious that the interfacial structures and dynamics are strongly influenced by the intra-molecular thermal excitations. Although each molecule is statistically equivalent over a long period of time, the instantaneous atomic configurations can be quite different among neighboring molecules due to the intra-molecular thermal excitations.

A closer examination of the motion of individual interfacial atoms suggests that the time evolution of the *x*-coordinate of one of these CH_3– united atoms can be described with two scales, one with the smaller sub-Angstrom length scale and shorter sub-Pico-second time scale, and the other one with long 3-4 Å length scale and slower a few Pico-second time scale. The smaller/shorter position fluctuation is a common feature for oscillation type of thermal motions. For this CH_3– atom, it is likely attributed to the bond angle bending motions. The larger/longer position fluctuation suggests weakly restoring or hopping type of thermal motions that associate with flat energetic landscapes with multiple local equilibrium in the configuration space. More importantly, comparing the motion of one interfacial atom (Figure 5-4(a)) with that of its neighboring interfacial atoms (Figure 5-4(b), one from the same side of the interface, the other on the opposite side of interaction), we do not find any strong correlations among their motions. This suggests the weaker vdW type inter-molecular forces only play a minor role on the dynamics of CH3– atoms at interfaces, while the much stronger intra-molecular forces exert a dominant influence on the interfacial dynamics. As a result, we find a relatively marked and temperature-dependent interfacial roughness (Figure 5-4 (c) and (d)). It is worth noting that the interfacial roughness in the conventional lattice-to-lattice interfaces typically has little temperature dependence after thermal annealing.

5.2 Microscopic Heat Current

Figure 5-5 shows the NEMD temperature profile of a molecular model with 30,800 united-atoms, initially equilibrated at the pressure of 1 atm and the temperature of 300 K. In comparison to the TIC values of the dissimilar solid-solid interfaces [68][69][70][71][72][73], the NEMD results of the TIC between the neighboring ideal crystal blocks of the n-eicosane are illustrated in Figure 5-6. The TIC values between the rigid solid-solid interface are commonly predicted by the phonon acoustic mismatch mode and the phonon diffuse mismatch model. Due to the existence of the same n-eicosane blocks at both sides of the interface, the presence of overlapped vibration modes cannot be handled by the mismatch models. In addition, as the temperature increases, the decrease of the TIC value for n-eicosane contrasts the reported increase of the TIC values for the rigid solid-solid interfaces, which means that a new explanation of the TIC needs to be developed.

In contrast to the conventional constant gradient temperature profiles observed in bulk materials systems, the NEMD simulations yield a characteristic temperature profile with essentially uniform temperature distribution within each molecular block and noticeable temperature changes at the molecular interfaces. This edge-curved step-function-like temperature profile indicates that molecular vibrations propagate ballistically back-and-forth within a single molecule and that only a small fraction of these ballistic currents propagates through these molecular interfaces even though molecular vibrations on the opposite sides of an interface are essentially identical. More details can be found in the Appendix I.

To unveil the dynamic details at the atomistic scale, we further define the time-dependent interfacial heat current $Q_{\mathrm{int}}(t)$ as the instantaneous rate of total work, W, performed on atoms on the right, R, side of the interface exerted by the atoms from the left, L, side of the interface:

$$Q_{\mathrm{int}} = W_{L\to R} - W_{R\to L} = \sum_{i\in R} q_{\mathrm{atom}}^{(i)} - \sum_{i\in L} q_{\mathrm{atom}}^{(i)} = \frac{1}{2}\sum_{i\in R} \mathbf{f}_{L\to i}\cdot\mathbf{v}_i - \frac{1}{2}\sum_{i\in L} \mathbf{f}_{R\to i}\cdot\mathbf{v}_i \qquad \text{Eq. (5.1)}$$

where $\mathbf{v}_i$ represents the instantaneous velocity of an atom on the R or L side of the interface, and $\mathbf{f}_{L,R\to i}$ is the vdW force from all the atoms on the opposite side of the interface imparted to that atom. Under the steady-state condition, the time-averaged $\overline{Q_{\mathrm{int}}(t)}$ converges to the imposed heat current of 0.005 kcal/mol/fs. The quantity q_{atom} represents the instantaneous thermal energy exchange between a single atom and all the atoms on the other side of the molecular interface.

Our analysis shows that the total interfacial heat transfer in n-eicosane is predominantly achieved through the interaction between the end-atoms (i.e. the CH_3– atoms at the end n-eicosane chains) in the two adjacent blocks. As illustrated in Figure 5-7, the heat current across the interface can be verified by the time-average of the heat current across the interface at 150 K, 200 K, 250 K and 300 K. All four mean values of the heat current across the interface is around 0.005 kcal/mol/fs, which is consistent with the imposed heat current value. In addition, the summation of the heat current of all the atoms at each atomic layer (III-18, III-19, III-20, IV-1, IV-2 and IV-3) at 150 K and 300 K are illustrated in Figure 5-8. The intensity of the summation of the heat current of all 154 atoms in each atomic layer in both blocks decays as the distance between the corresponding atomic layers increases. This distance effect on the heat current across the interface is so strong that the observed heat transfer across the interface is only conducted by the interaction between the neighboring layers of the end-atoms (CH_3– groups in atomic layers 1 and 20) in the two adjacent blocks. Although the distance between the two atomic layers decreases as temperature is lowered to 150 K, this effect still dominates the heat transfer across the interface. Therefore, the study of microscopic heat transfer across the interface can be achieved exclusively by focusing on the performance of these end-atoms.

Since all the end-atoms, also referred as the interfacial atoms, are statistically equivalent, the ergodic assumption is valid with $\langle q_{\mathrm{atom}} \rangle = \overline{Q_{\mathrm{int}}(t)}/154 = 226$ pW. Therefore, the interfacial heat flow can be analyzed at the level of a single molecular chain for gaining new insights on the correlation between the microscopic dynamics and the thermal energy fluctuations at equilibrium conditions, and the interfacial heat transfer processes at non-equilibrium steady-state conditions. To correspond to the analysis of atomic interfacial heat current $q_{\mathrm{atom}}(t)$, we define the single molecule thermal conductance,

$$\gamma_k = \frac{\langle q_{\mathrm{atom}}(t) \rangle}{\Delta T} \; . \qquad \text{Eq. (5.2)}$$

As γ_k characterizes the rate of the interfacial heat transfer of individual molecules, the values of γ_k in industry-grade n-eicosane that consists of randomly aligned molecules likely correlate with the alignment angles between the molecule chains and the normal direction of the interface, and the conventional G_k reflects an ensemble average value of individual values of γ_k. For ideal crystals with identical value of γ_k for all the molecules, $G_k = 154\ \gamma_k/S$, where S is area of the cross-section of the supercell models.

To extract the temperature discontinuity ΔT from the NEMD simulations, we focus on the molecular interface between blocks III and IV to minimize the artifacts induced by the relatively small distance (less than 14 nm) between the heat source and heat sink in the molecular system. At 300 K, ΔT is found to be 11.3 K, and it consists of two distinct components: a temperature jump/drop less than one Kelvin between interfacial end-atoms and their nearest distance neighbors in the identical molecule over the length scale of one Carbon-Carbon bond length, and a temperature discontinuity of a few Kelvins across a spatial gap about 0.3 nm. The contrast in the magnitudes of two ΔT components manifests the fact that an interfacial end-atom is more readily thermalized with its neighbors on the same side of the interfaces via strong Carbon-Carbon bonding forces than with other atoms on the opposite side of the interface via weak vdW forces. As a result, we predict a γ_k of 20 pW/K at 300 K for a molecule aligned normally to the interface, which corresponds to a G_k of 107 MW/m^2/K and an effective κ along the alignment direction of 0.3 W/mK.

5.3 Thermally Coupling-Decoupling Mechanism

To complement the simulations of steady-state temperature profiles, we calculate the instantaneous atomic heat flux $q_{\text{atom}}(t)$, as defined in Eq. (5.1), using the MD-simulated velocity and interfacial force of individual end-atoms. Figure 5-9 shows that $q_{\text{atom}}(t)$ is modulated by the vdW forces and it has two distinct patterns of cross-interface heat exchange. The first pattern of relatively large, pulse-like $q_{\text{atom}}(t)$ occurs when the interfacial end-atom is subject to an oscillating repulsive-attractive interfacial force, while the second pattern of fairly small, noise-like $q_{\text{atom}}(t)$ occurs when the interfacial end-atom is subjected to a small and continuously attractive interfacial force for a period of a few picoseconds or longer. By defining the noise-like heat exchange periods as the uninterrupted time periods with small attractive interfacial forces that last more than 1 pico-second, we estimate that the noise-like heat exchange periods count for nearly 45% of the total time at 300 K. Yet, the accumulated heat current that flows across the molecular interface during these noise-like time periods only accounts for less than 1% of the net interfacial heat transfer. We note that the alternating patterns of interfacial heat exchange emerge only at the atomistic scale, and the total interfacial heat currents (i.e. the summations of all the 154 individual $q_{\text{atom}}(t)$) fluctuate over time with only very short correlation times.

Based on the observation of two alternating heat exchange patterns and the contrast in their contributions to the net heat transfer across an interface, we propose a dynamical fluctuation-induced thermal coupling-decoupling mechanism for the vdW forces mediating interfacial heat transfer. Because the length of a single n-eicosane molecule is only of the order of a nano-meter, one molecule can instantaneously move collectively toward one direction due to thermal fluctuation in its molecular dynamics, resulting in a collision-like interaction with the molecules on the opposite side of the interface and rapid exchange of kinetic energy among them. During this collision process, the ballistic currents on both sides of the interfaces are thermally coupled to allow a net heat flow from the higher temperature side to the lower temperature side. However, the attractive vdW forces are anharmonic, and have a small maximum value, allowing the molecules to escape the regime of restoring forces and be subject to only very small (or even zero) attractive interfacial vdW forces for extended periods of time. Before dynamic fluctuations “kick” the molecule back into collision with the other molecules on the opposite side of the interface, this molecule is essentially thermally decoupled from those molecules on the opposite side of the interface, and no net energy is transferred across the interface through this molecule. To quantify the heat exchange properties at the atomistic scale, we propose two new microscopic parameters. The first parameter, defined as thermal coupling ratio, α_c = thermally coupled time / total time, represents the probability of the molecule being thermally coupled with the molecules on the opposite side of the interface. This α_c parameter also reflects the rigidity/flexibility of a molecular interface, as it should approach 1 for conventional rigid lattice-to-lattice interfaces with quasi-harmonic restoring forces. The second parameter is proposed to quantify the strength of thermal coupling. It has long been speculated that the efficiency of interfacial heat transfer correlates with the strength of interfacial forces. However, because the weak vdW forces that are intrinsically anharmonic, the harmonic spring constant concept is less relevant. Instead, we propose using the standard deviation (σ_c) of the pulse-like q_{atom} fluctuation during the thermally-coupled time periods to quantify the effectiveness of interfacial heat transfer that is mediated with the weak and anharmonic forces. This concept of σ_c is applicable for the conventional lattice-lattice interfaces in principle.

Furthermore, additional NEMD calculations with a different energy transfer rate (0.02 kcal/mol/fs) or with different n-alkane chain lengths (see Appendix I.2) are performed, concluding that the values of both parameters, α_c and σ_c, do not vary significantly among the studied NEMD energy transfer rates and the molecular chain lengths. These two newly-proposed interfacial heat exchange parameters manifest the intrinsic dynamical fluctuation at flexible interfaces and they can be evaluated using EMD simulations, where the temperature is more readily defined and the overall computational loads are significantly smaller. Figure 5-10 illustrates the extracted α_c and σ_c parameters as functions of temperature using a series of EMD simulations from 150 K to 300 K. As the thermal fluctuation increases with temperature, α_c decreases from 0.85 at 150 K to about 0.57 at 300 K. At the same time, the σ_c is roughly linearly proportional to temperature. As a comparison, the standard deviation (σ_d) of the noise-like q_{atom} fluctuation during the thermally-decoupled time periods not only is significantly smaller than σ_c, but also shows much smaller temperature dependence. More importantly, the values of the single molecule thermal conductance γ_k based on the classical NEMD at four temperatures, 150 K, 200 K, 250 K and 300 K, have an interesting linear correlation with $\alpha_c\ \sigma_c\ /\ T$ (Figure 5-11 a). Based on the linear correlation, we propose a general theoretical model of single molecule TIC of a soft (i.e. "non-welded") molecular interface based on the thermal coupling-decoupling mechanism of cross-interface heat transfer:

$$\gamma_k = \alpha_c \gamma_c + (1-\alpha_c)\gamma_d \approx \alpha_c \gamma_c . \qquad \text{Eq. (5.3)}$$

Within this thermal coupling-decoupling theory, the effective single molecule TIC during the thermal decoupling time periods is approximately zero, i.e. $\gamma_d \approx 0$. The effective single molecule TIC during the thermal coupling time periods γ_c, which represents the upper limit value of γ_k in the case of rigid 100% thermal coupling, is proportional to σ_c/T. The magnitude and the temperature dependence of σ_c likely correlate with effective interfacial bonding strength during the thermally coupled time periods. In the case of n-eicosane, the fitted coefficient of proportionality is 0.332, i.e. $\gamma_c = 0.332\sigma_c\ /\ T$. This coefficient possibly manifests the level of mismatch between a single molecule and the block of molecules on the opposite side of the soft molecular interface during the thermally coupled time periods. As discussed in the "Molecular Structure Details" section, the instantaneous atomic configuration of a single molecule can be quite different from those on the opposite side of the interfaces due to intra-molecular bond bending/twisting.

Based on the thermal coupling-decoupling model Eq. (5.3), we plot the predicted single molecule conductance γ_k of a single crystal of n-eicosane, the G_k of an ideal interface, and the corresponding effective κ along the alignment direction from 150 K to 300 K in Figure 5-11 b, c and d. A key prediction of the thermal coupling-decoupling theory is that the temperature dependence of TIC depends on both the temperature dependence of σ_c and the temperature dependence of α_c. At the onset of melting in a phase change material, the change in α_c has a significant effect on the TIC. Our theoretical model suggests that the intrinsic temperature dependence in bulk κ has a small, yet inverse temperature dependence near the melting temperature. This inverse temperature dependence is largely caused by a significant increase of the duration of the thermally-decoupled time periods at the onset of melting processes in n-eicosane.

5.4 Summary

In summary, we combine MD simulations and a time-domain analysis of interfacial heat current flowing through a single molecule to study heat transfer across a vdW force-bonded flexible interface in n-eicosane. The nearly flat temperature distribution at a nano-meter scale in the NEMD simulations suggests that the heat current in a perfect n-eicosane crystal is both ballistic and spatially confined. The abrupt temperature changes at the both ends of n-eicosane molecules suggest that only a small portion of intra-molecule ballistic currents tunnel through the flexible molecular interfaces that are connected with the vdW forces. Based on a dynamic fluctuation-induced thermal coupling-decoupling model, we quantify the interfacial heat exchange properties of a single molecule with two parameters, α_c and σ_c. It was demonstrated that the single molecule thermal conductance correlates linearly with $\alpha_c \sigma_c / T$. Based on the NEMD simulations and the newly-proposed interfacial heat transfer model, we predict that when an n-eicosane molecule is aligned normal to a flexible molecular interface, its single molecule thermal conductance γ_k is roughly 19.9 *p*W/K at 300 K and has a small yet inverse temperature dependence near the melting temperature. Future studies on how the alignment angle between a single molecular chain and the normal direction of an interface affect parameters α_c and σ_c is the next step to quantify the morphology-G_k relation. The origin of the linear correlation between γ_k and $\alpha_c \sigma_c / T$ and the material/interface properties that regulate the proportionality constant are not yet understood. This atomistic-scale thermal coupling-decoupling phenomenon and the corresponding linear correlation relation should be further tested in other flexible molecular interfaces of soft materials that are bonded with weak and anharmonic interfacial forces at the temperature regime near the melting temperatures.

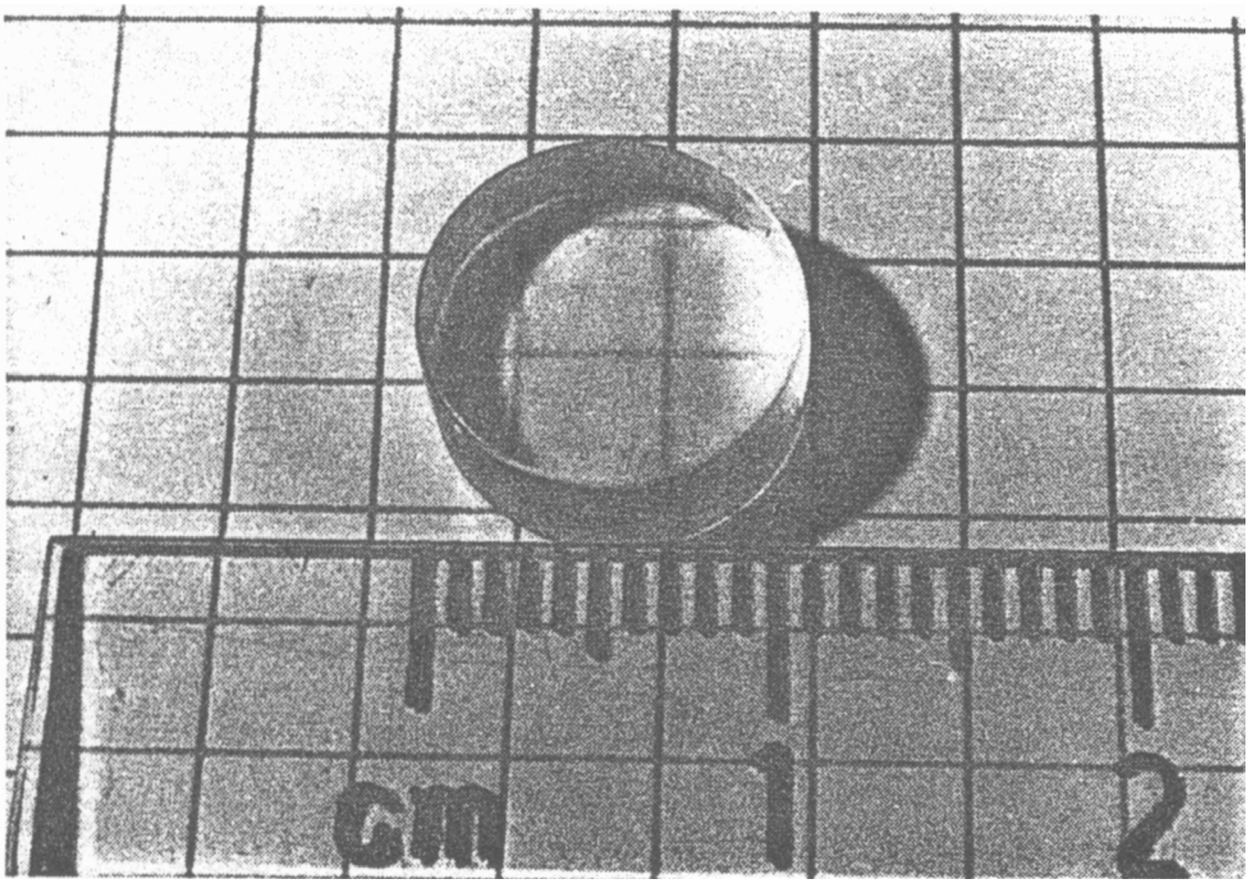

Figure 5-1 An n-Eicosane single crystal grown by the Bridgman technique. [67]

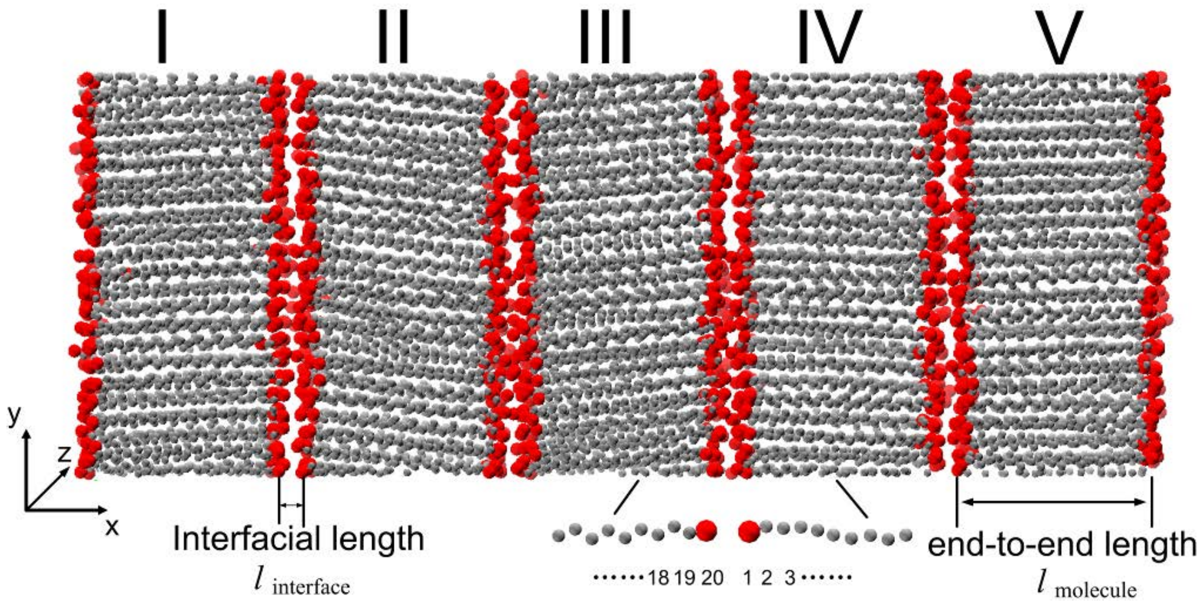

Figure 5-2 Snapshot of five blocks of $C_{20}H_{42}$ molecules in an ideal crystal, with each block consisting of 154 molecules closely-packed on the *y*-*z* plane. Each united atom (UA) in a $C_{20}H_{42}$ molecule chain is labeled from 1 to 20, from left to right. The UAs with indices of either 1 or 20 (shown as the red solid balls) are the CH_3– groups identifying the molecular interfaces. The UAs with indices from 2 to 19 (shown as grey solid balls) are the –CH_2– groups.

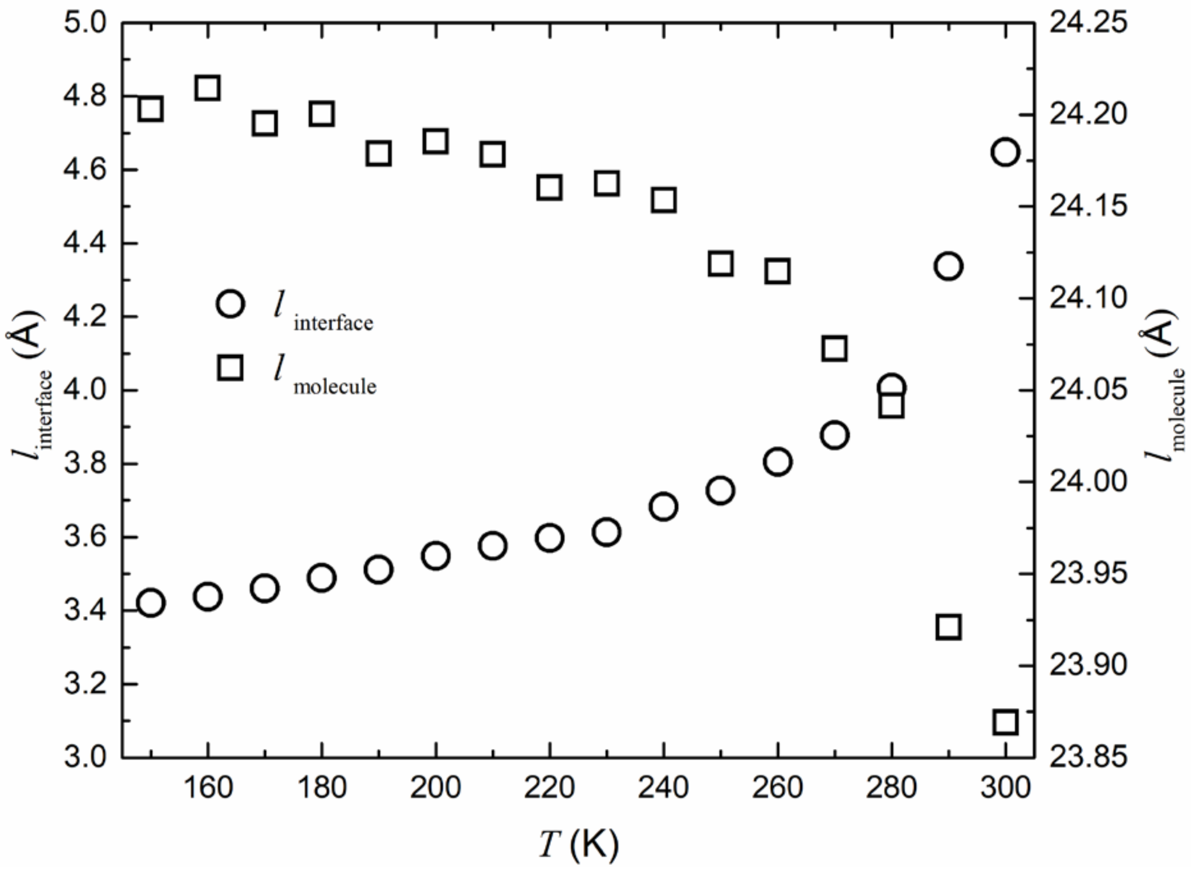

Figure 5-3 Temperature dependence of the average values of $l_{interface}$ and $l_{molecule}$

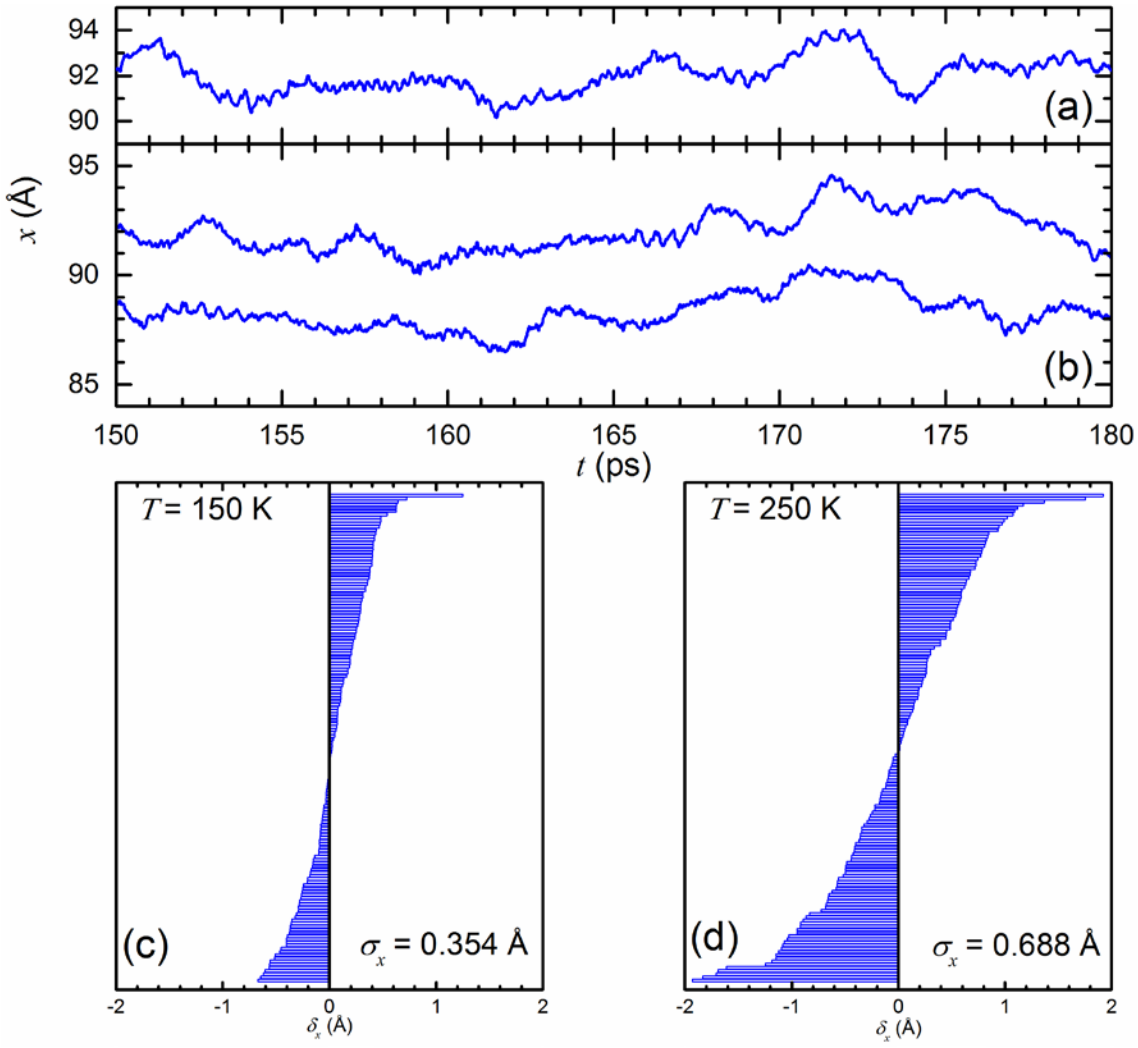

Figure 5-4 The *x*-direction motion of (a) one interfacial atom and (b) its neighboring interfacial atoms (one from the same side of the interface, the other on the opposite side of interaction). The distribution of the difference between the *x* position of each of the interfacial atoms and the mean value of *x* position of all the interfacial atoms at (c) 150 K and (d) 250 K.

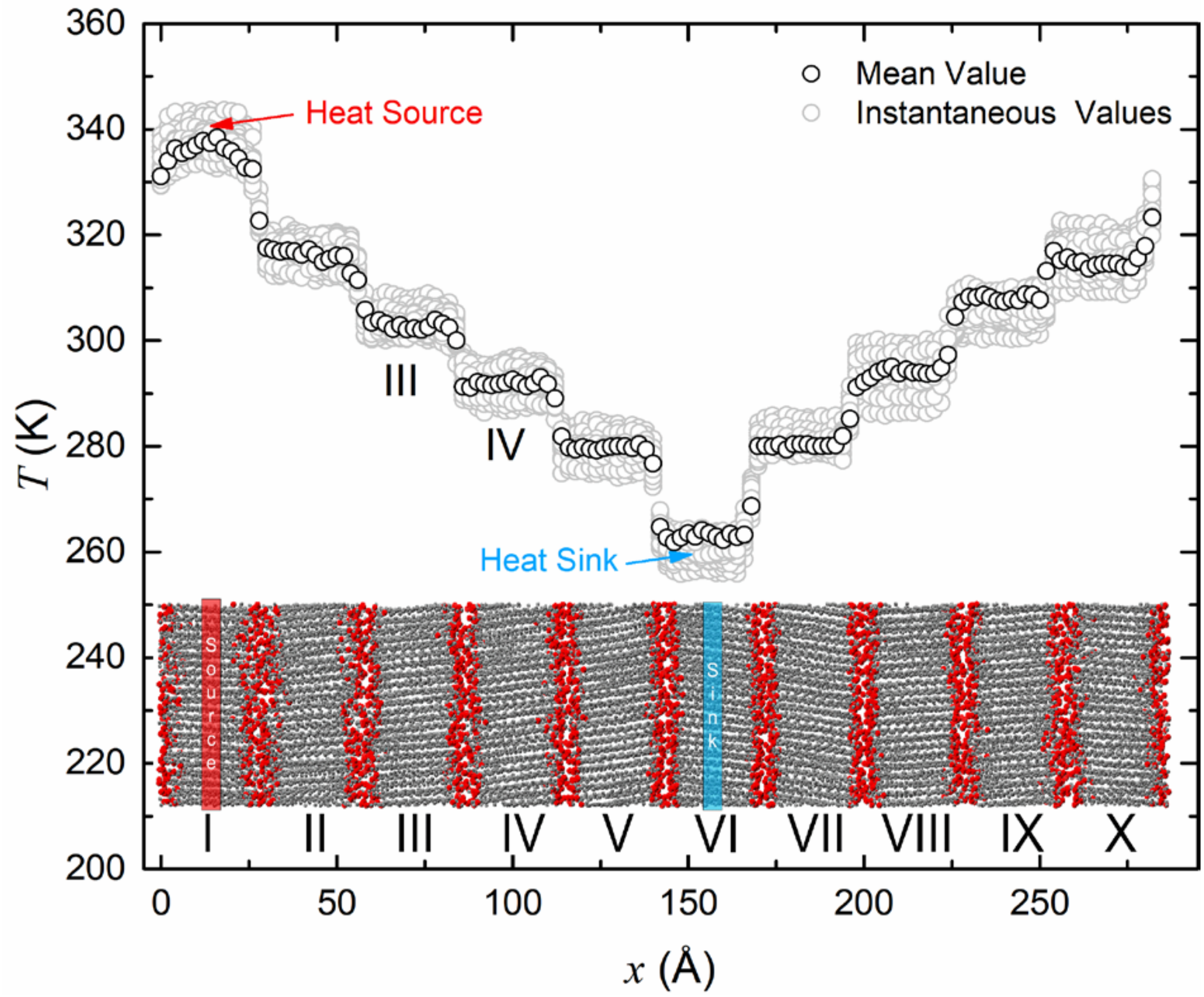

Figure 5-5 Temperature profile of an NEMD-simulated steady-state of a 10-block n-eicosane supercell model. The grey (light) and the red (dark) balls represent the CH_2 and CH_3 groups, respectively.

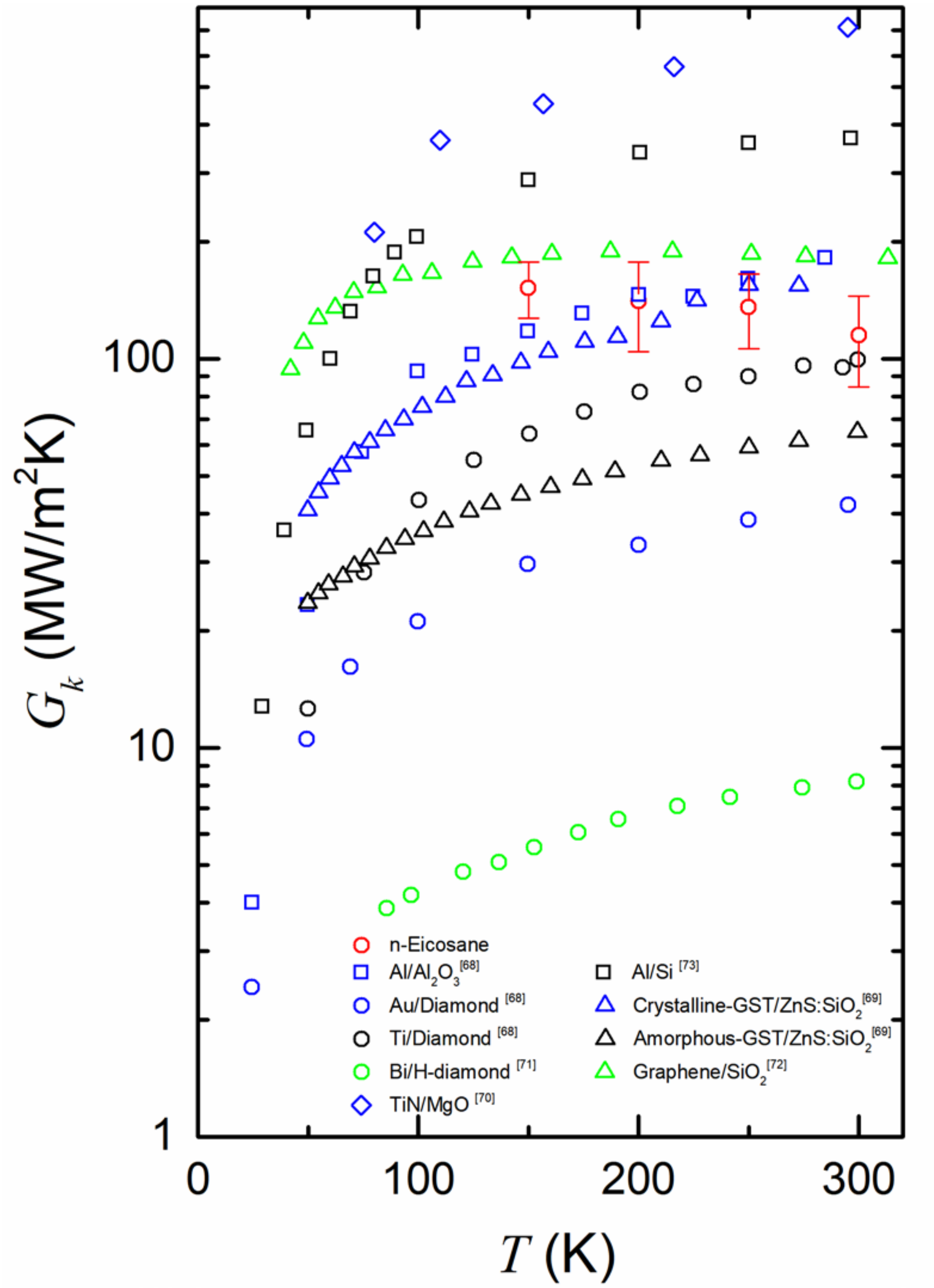

Figure 5-6 Interfacial thermal conductance values from the ideal crystal of n-eicosane in comparison to various solid-solid interfaces at different temperatures.

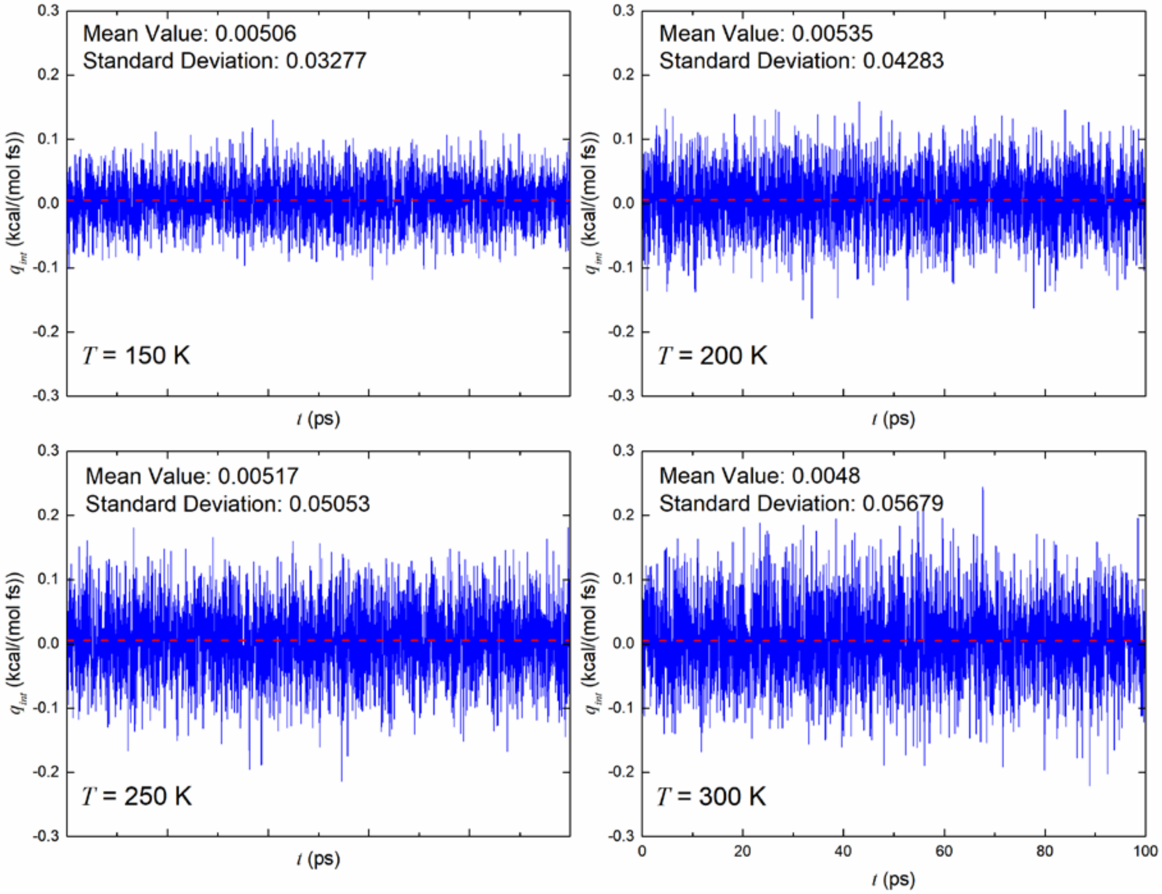

Figure 5-7 Heat current across the interface at different temperatures.

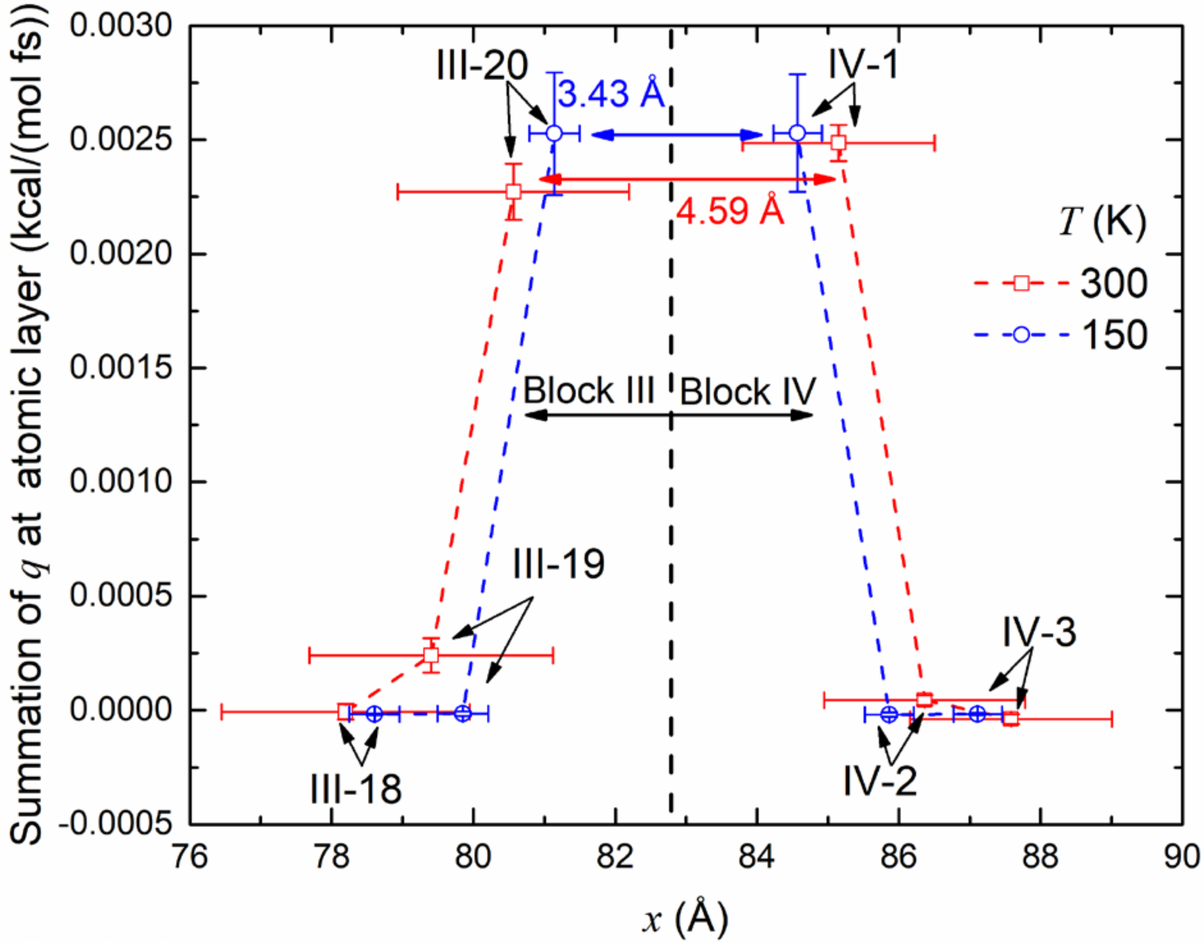

Figure 5-8 Heat current transported between atoms within different layers of blocks III and IV at 150 K and 300 K (*q* represents the general heat current across the interface from one block to its neighboring block).

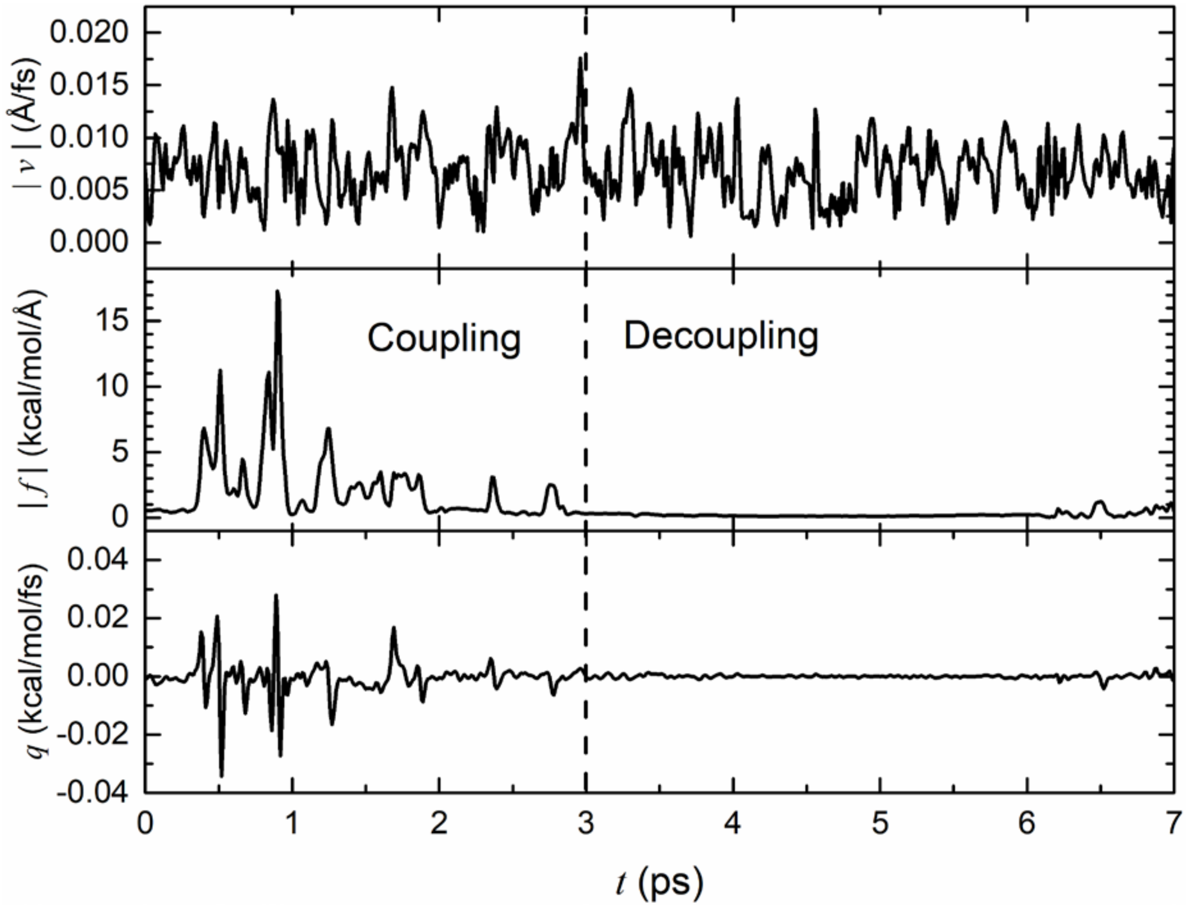

Figure 5-9 Fluctuations of the instantaneous velocity, the vdW force on the CH_3– group in block IV from block III, and the corresponding single-molecule interfacial heat current, over a representative time period of 7 ps. The vertical dash-line indicates the transition from a period of pulse-like thermal energy exchange to a period of noise-like thermal energy exchange.

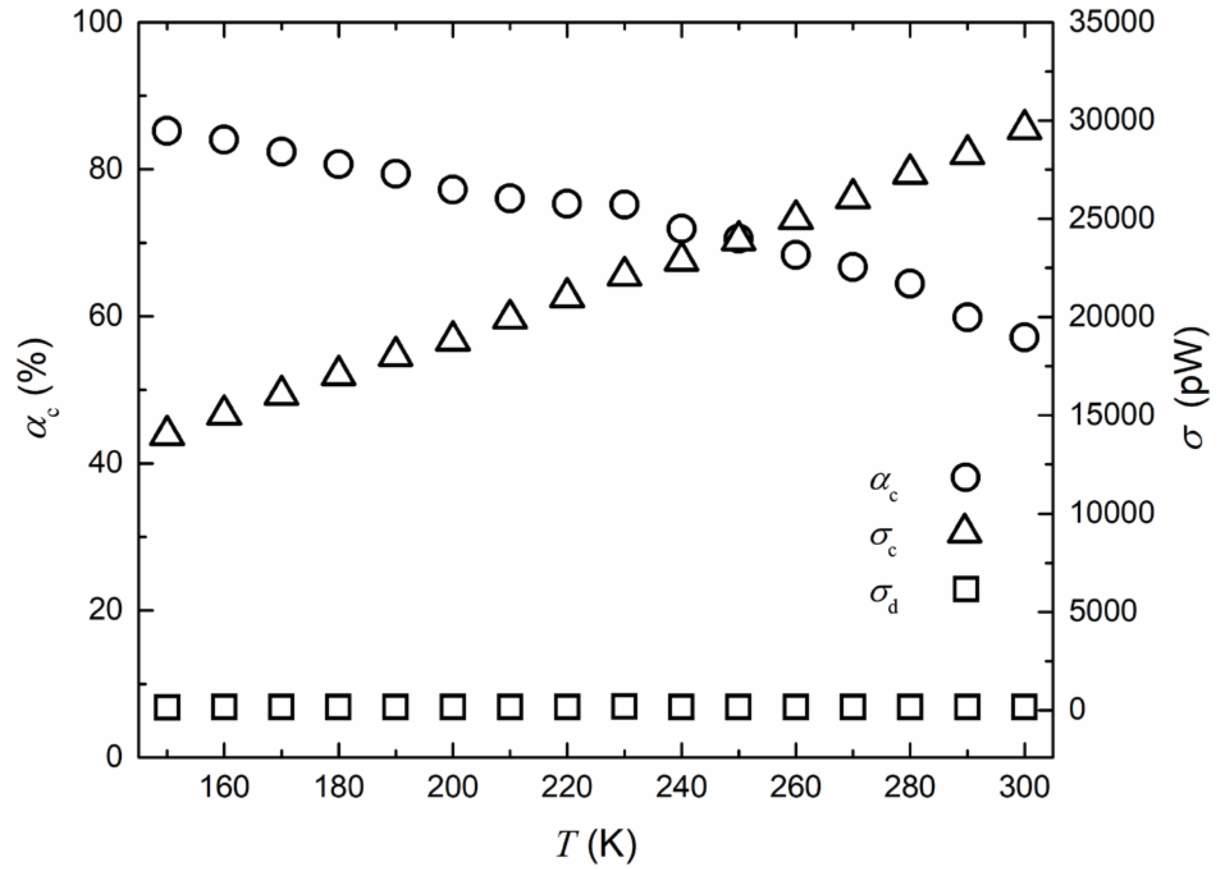

Figure 5-10 Temperature dependence of two microscopic interfacial heat exchange parameters: the collision rate α_c (○) and the standard deviation of the pulse-like heat currents σ_c (△) during the thermally-coupled periods. For comparison purposes, we also include results of standard deviation of the noise-like heat currents σ_d (☐) during the thermally-decoupled time periods.

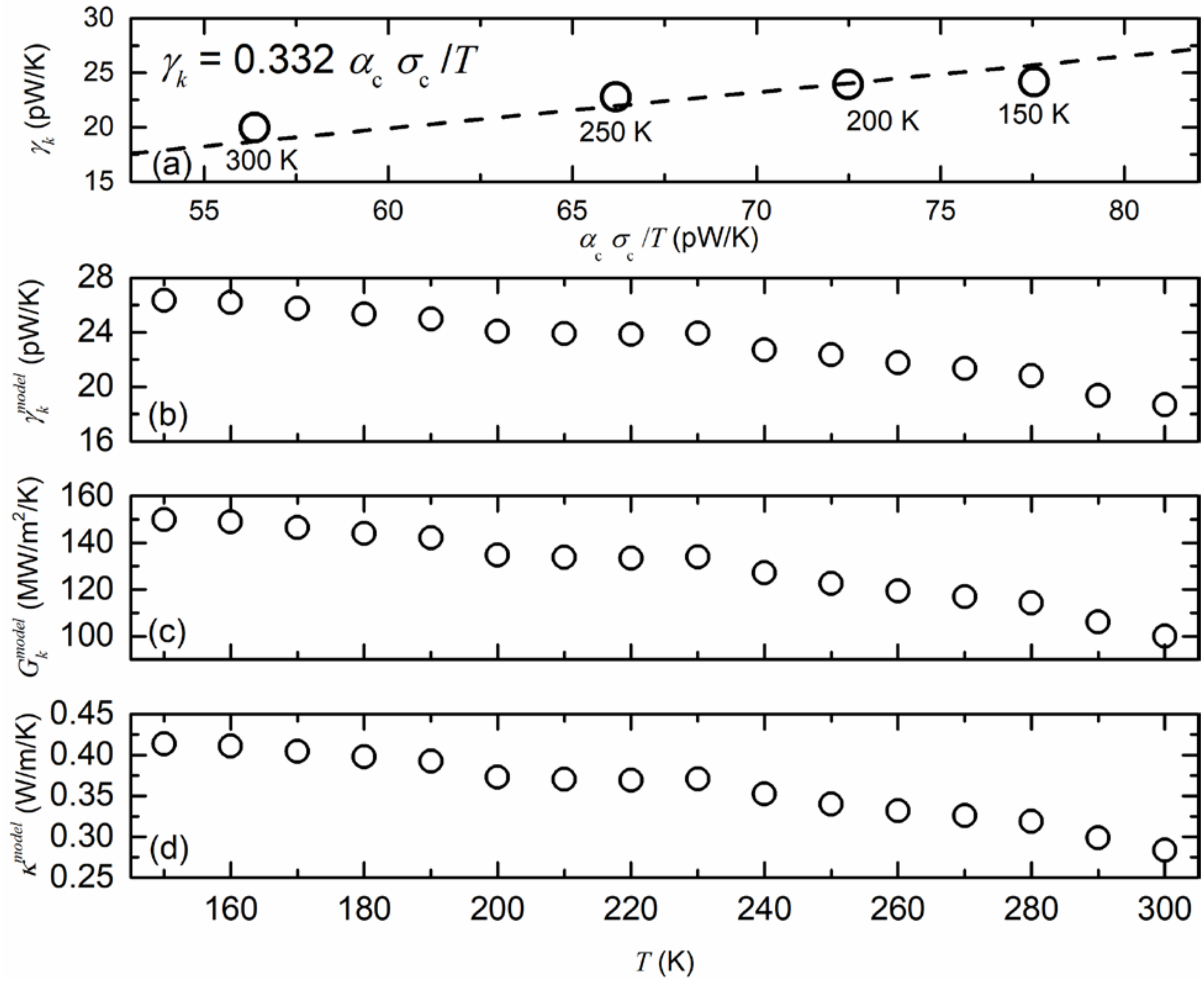

Figure 5-11(a) A nearly linear correlation between the values of the single molecule thermal conductance γ_k and $\alpha_c\ \sigma_c\ /\ T$ in n-eicosane between 150 K and 300 K. Model-predicted temperature dependence of (b) the single molecule thermal conductance γ_k when a molecule aligns normally to an interface, (c) thermal interfacial conductance G_k of a perfectly-aligned interface, and (d) the effective thermal conductivity κ along the alignment direction.

Chapter 6 Fokker-Planck equation for lattice vibration: Stochastic dynamics and thermal conductivity

6.1 Introduction

A schematic plot of a typical temperature dependence of lattice thermal conductivity (κ_{Latt}) in crystals is shown in Figure 6-1. Within the PG approximation, the phonon BTE predicts that κ_{Latt} of a crystal decays to zero with increasing temperature, T, at the rate of $1/T$ or faster. However, experimental measurements [74][75] reveal that the deviation from the $1/T$ scaling become noticeable as T approaches the melting temperature, T_{melt}, of the lattice, with κ_{Latt} eventually reaching a low constant value. The omnipresence of these minimal thermal conductivities (κ_{min}) [76] in all crystalline lattices suggests that as a lattice approaches its T_{melt}, the increasingly strong anharmonic coupling among vibrational modes causes the breakdown of the PG model. Such breakdown might occur at moderate temperatures in relatively soft solids with large thermal expansion [77][78] or in the high temperature phases of solids whose 0 K phonon spectra contain imaginary frequencies [79]. In addition, the phonon BTE incorporates the concept of phonon group velocity, which is not properly defined in nonperiodic solids such as alloys, glass, or amorphous semiconductors [80], even at the conditions where all the vibrational modes remain quasiharmonic [81].

When the accuracy of the phonon BTE theory is in question, the statistical linear response transport theory [82] is often combined with equilibrium molecular dynamics (MD) simulations to predict thermal transport properties [83][84][85][86]. For example, the Green-Kubo (GK) formalism states that thermal conductivity is proportional to the time-integral of the auto-correlation function of heat flux [87][88]. Although the GK method is theoretically rigorous and valid beyond the PG approximation, its current implementations, based on the evaluations of atomic trajectories, i.e., displacements and velocities, over a long period of time, usually require much more intensive computational loads. When no reliable empirical force-field interatomic potentials exist, ab initio MD simulations are necessary to simulate the complex lattice vibration. Yet, in practice, typical ab initio MD simulations are often carried out with only relatively short simulation periods (i.e., of the order of a few picoseconds) and using relatively small supercell models (i.e., of the order of a couple of hundred atoms) because their computational loads scale as order N^3, where N is the number of atoms in a supercell model. These numerical finite-size artifacts sometimes impose relatively large uncertainties in the ab initio MD simulation results. Additional approximations are often needed to extract potential energy of each atom from the ab initio total energies of the supercell models to evaluate the correlation function of heat currents using the ab initio MD simulation results [89][90][91][92][93].

More importantly, all the atomic trajectories in MD simulations have to be calculated numerically, even at the weak scattering limit of the PG model. This lack of analytical solutions of atomic trajectories in MD simulations hinders the development of quantitative theoretical models to interpret the simulated current-current correlation functions because it provides little insight on improving/correcting the PG model beyond the weak scattering limit. Ladd et al. [94] proposed a normal mode analysis (NMA) approach to evaluate the phonon lifetimes τ based on the damped oscillator approximation (DOA). Using the extracted phonon lifetimes, they derived the so-called Peierls phonon-transport expression of κ_{Latt}, which is understood to be only an approximate solution of the phonon BTE theory. Nevertheless, these types of NMA methods have been useful to interpret the phonon scattering in a MD simulation, and these methods have been implemented and further developed in recent years by many groups using both empirical potentials and ab initio methods [95][96][97][98]. However, both the DOA and the concept of phonon lifetime/relaxation-time should be adopted only as semiquantitative models because the cross-correlations among different vibrational modes cannot always be neglected. More robust theoretical models or concepts are needed to quantitatively interpret the NMA results of numerical MD simulations.

In this chapter, a time-dependent statistical theory to quantitatively describe the thermal fluctuation and correlation properties of vibrational modes using a Fokker-Planck equation for lattice dynamics is presented. First, this vibration FPE theory does not treat the interactions among different vibrational modes as small perturbations. Instead, the theory includes two general sets of parameters, the drift A and the diffusion B coefficients, to explicitly characterize the mode-mode interactions. The results of this vibration FPE, expressed in terms of a time-dependent probability function of multiple-variable vibrational microstates, provide details of the dynamic relaxation processes of lattice vibration, and are readily used by the linear response transport theory to compute κ_{Latt} beyond the quasiharmonic phonon gas model.

Second, this vibration FPE provides detailed information on the time-correlation properties of physical quantities without requirement of long-time MD simulations. The proposed vibration FPE derives the correlation functions based on the probability function governed by the drift A and diffusion B coefficients, which are defined in terms of ensemble averages at the $\delta t \rightarrow 0$ limit. It is important to emphasize that no a priori forms of correlation functions are assumed in a FPE calculation of correlation functions. As a result, when implemented with first-principles methods, this vibration FPE is promising to be both accurate and efficient to predict κ_{Latt} of novel and complex solids at wide-ranging conditions.

Finally, the κ_{Latt} predicted by the vibration FPE converges to the one from the conventional phonon BTE within the phonon gas model. Because the FPE's parameters of a lattice vibration can be evaluated with either perturbative methods or simulation methods at the PG approximation, the vibration FPE theory establishes a systematical computational methodology to analyze errors of the simple PG model and to delineate the

6.2 Stochastic Dynamics of Lattice Vibration

6.2.1 Fokker-Planck equation

The first fundamental assumption of this proposed Fokker-Planck equation for lattice vibration is that thermal lattice dynamics is a stochastic process at the microscopic level, and the probabilistic transition dynamics from one vibration microstate Γ to other thermally accessible microstates can be modeled with a statistical master equation [82][99]. When a specific microstate Γ^0 is sampled at time $t = 0$, the initial probability function is simply

$$P(\Gamma, t=0 \,|\, \Gamma^0) = \delta(\Gamma - \Gamma^0) \,. \qquad \text{Eq. (6.1)}$$

Regardless of the dynamic details of a stochastic process, the equilibrium ensemble theory constrains that at the long time limit of $t \to \infty$, the probability function evolves into the canonical distribution function:

$$P(\Gamma, t \to \infty \,|\, \Gamma^0) \to P_{eq}(\Gamma) = \frac{e^{\frac{-E(\Gamma)}{k_B T}}}{Z_{eq}(T)} \,, \qquad \text{Eq. (6.2)}$$

where k_B is the Boltzmann constant, T represents temperature, $E(\Gamma)$ denotes the energy of any micro-state Γ, and $Z_{eq}(T)$ denotes the equilibrium canonical partition function of the lattice vibration. The evolution of this probability function $P(\Gamma, t \,|\, \Gamma^0)$ provides a general and quantitative description of lattice thermal relaxation processes, from a single initially sampled micro-state Γ^0 to a set of all the thermally accessible micro-states that correspond to an equilibrium distribution governed by the equilibrium statistics. The ergodic condition in lattice vibration is assumed.

We further adopt the Born-von-Karman periodic boundary condition [7] to specify the vibrational micro-states with total N vibration modes, with N→∞ for an infinitely large crystal. Using the numbers of phonons at these modes, i.e. n_α with α=1, 2, 3 ⋯,N, we specify a vibrational micro-state with a set of N-dimensional state-variables $\Gamma = \{n_1, n_2, \cdots, n_N\}$. Through the Kramers-Moyal expansion of the master equation, the time-evolution of this probability function $P(\Gamma, t \mid \Gamma^0) = P(n_1, n_2, \cdots, n_N, t \mid n_1^0, n_2^0, \cdots, n_N^0)$ can be expressed in the form of a FPE [82][99]:

$$\frac{\partial P}{\partial t} = -\sum_{\alpha=1}^{N} \frac{\partial}{\partial n_\alpha}[A_\alpha(\Gamma)\cdot P] + \frac{1}{2}\sum_{\alpha\beta} \frac{\partial^2}{\partial n_\alpha \partial n_\beta}[B_{\alpha\beta}(\Gamma)\cdot P] \qquad \text{Eq. (6.3)}$$

The assumption of a FPE is that the third-order expansion coefficients are approximately zero. According to the Pawula theorem, all the higher order expansion coefficients are zero if the third-order expansion coefficients are zero [99]. Within this theoretical framework, the drift $A_\alpha(\Gamma)$ and diffusion $B_{\alpha\beta}(\Gamma)$ coefficients manifest the interactions among vibrational modes, and they are defined as:

$$\begin{aligned} A_\alpha(\Gamma) &\equiv \lim_{\delta t \to 0} \frac{1}{\delta t}\int_0^{\delta t} d\Gamma' \delta n_\alpha(\Gamma, \Gamma') P(\Gamma', \delta t \mid \Gamma) \\ B_{\alpha\beta}(\Gamma) &\equiv \lim_{\delta t \to 0} \frac{1}{\delta t}\int_0^{\delta t} d\Gamma' \delta n_\alpha(\Gamma, \Gamma') \delta n_\beta(\Gamma, \Gamma') P(\Gamma', \delta t \mid \Gamma) \end{aligned} \qquad \text{Eq. (6.4)}$$

In the case that a stochastic lattice vibration can be modeled as a random process of transition from one vibrational microstate Γ to another microstate Γ' with a known rate of transition $w_{\Gamma \to \Gamma'}$, Eq. (6.4) can be approximated as

$$\begin{aligned} A_\alpha(\Gamma) &\approx \int d\Gamma' [n_\alpha(\Gamma') - n_\alpha(\Gamma)] \cdot w_{\Gamma \to \Gamma'} \\ B_{\alpha\beta}(\Gamma) &\approx \int d\Gamma' [n_\alpha(\Gamma') - n_\alpha(\Gamma)] \cdot [n_\beta(\Gamma') - n_\beta(\Gamma)] \cdot w_{\Gamma \to \Gamma'} \end{aligned} \qquad \text{Eq. (6.5)}$$

Within this statistical probability theory (Eq. (6.3)), the dynamic details of a stochastic lattice vibration rely on the knowledge of both drift A and diffusion B coefficients. As formulated in Eq. (6.4), both A and B coefficients can be numerically calculated based on an ensemble of microscopic simulations over a short period of simulation time δt. Since the simulation periods for the parameter evaluation is short, it becomes practical to implement the numerical simulations using accurate yet numerically demanding first-principles methods. The overall computational loads of ensemble average, although still intensive, can be in principle distributed over a cluster of computer nodes to take full advantage of the state-of-the-art parallel high-performance computing platforms. Choosing an appropriate simulation period δt for the parameter calculations is not merely a numeric issue. The size of δt reflects the level of temporal coarse-graining. For example, in a bulk system, δt should be larger than the oscillating periods, as well as the ballistic time periods, to ensure the assumption of a thermal relaxation process. Different values δt might be needed when there are more than one drift/diffusion mechanism. For example, in an amorphous lattice, the drift/diffusion time scale for an extended vibrational mode likely differs significantly from that of a strongly localized vibration mode. Extensive future studies are needed to gain a better understanding of the forms of the A and B coefficients of a vibration FPE.

On the other hand, The general forms for the A and B coefficients defined in Eq. (6.4) imply that the proposed vibration FPE theory does not limit the magnitude of the mode-mode interactions in a lattice to be perturbatively small, nor does it require each mode correspond to a traveling wave with a specific group velocity $\overrightarrow{v_\alpha}$. Consequently, this vibration FPE, as formulated in Eq. (6.3), is valid for lattice vibration with a broad range of mode-mode interactions, including lattice vibration with strong anharmonic modes and/or disorder-induced spatially localized modes. In addition, in the weak scattering case that both initial (Γ) and final Γ' quantum vibration states can be represented by the phonon representation $|n_1, n_2, n_3, \cdots, n_N>$ and $\Delta\hat{V}$ denotes perturbatively small deviations in the vibration Hamiltonian from that of the ideal phonon gas. We can use Fermi's golden rule to calculate the rate of transition:

$$w_{\Gamma\to\Gamma'} = \frac{2\pi}{\hbar} |< n_1', n_2', n_3', \cdots, n_N' \,|\, \Delta\hat{V} \,|\, n_1, n_2, n_3, \cdots, n_N >|^2 \qquad \text{Eq. (6.6)}$$

6.2.2 Thermal relaxation: Fluctuation and correlation

At thermal equilibrium, the instantaneous value of a quantity *X*, either macroscopic or microscopic, fluctuates around its equilibrium value X_{eq}. The dynamical process that brings the fluctuating value of $X(t)$ back toward the X_{eq} is commonly referred as a thermal relaxation process. A self-correlation function of *X*:

$$C_{XX}(t) \equiv \langle \delta X(0) \cdot \delta X(t) \rangle_{eq} = \langle (X(0) - X_{eq}) \cdot (X(t) - X_{eq}) \rangle_{eq} \qquad \text{Eq. (6.7)}$$

is often used to quantify the properties of this thermal relaxation process. When *X* can be expressed in terms of micro-state variables $X(\Gamma)$, we can define a time-dependent expectation value $\overline{X}(t\,|\,\Gamma^0)$ based on the probability function $P(\Gamma, t\,|\,\Gamma^0)$ in the vibration FPE, staring with the initial probability function shown in Eq. (6.1):

$$\begin{aligned}
\overline{X}(t\,|\,\Gamma^0) \quad &\equiv \int d\Gamma P(\Gamma, t\,|\,\Gamma^0) \cdot X(\Gamma), \\
\frac{d\overline{X}(t\,|\,\Gamma^0)}{dt} \quad &\equiv \int d\Gamma \frac{\partial P(\Gamma, t\,|\,\Gamma^0)}{\partial t} \cdot X(\Gamma) \\
&= \sum_{\alpha} \overline{[\frac{\partial X}{\partial n_\alpha} \cdot A_\alpha]}(t\,|\,\Gamma^0) + \frac{1}{2} \sum_{\alpha\beta} \overline{[\frac{\partial^2 X}{\partial n_\alpha \partial n_\beta} \cdot B_{\alpha\beta}]}(t\,|\,\Gamma^0)
\end{aligned} \qquad \text{Eq. (6.8)}$$

Clearly, $\overline{X}(t)$ starts at its initial value of $X(\Gamma^0) = \int d\Gamma \delta(\Gamma - \Gamma^0) X(\Gamma)$ and eventually relaxes back to its equilibrium value of $X_{eq} = \int d\Gamma X(\Gamma) P_{eq}(\Gamma)$ when $P(\Gamma, t\,|\,\Gamma^0) \to P_{eq}(\Gamma)$ at the limit of $t \to \infty$. Similarly, the corresponding time-dependent statistical variance, defined as

$\Delta_X(t\,|\,\Gamma_0) \equiv \overline{X^2}(t\,|\,\Gamma_0) - \overline{X}(t\,|\,\Gamma_0)^2$, relaxes from its initial value of 0 to its equilibrium value $\Delta_{X,eq} = \int d\Gamma(X(\Gamma) - X_{eq})^2 ? P_{eq}(\Gamma) > 0$.

By sampling the initial micro-states Γ^0 with the equilibrium probability function $P_{eq}(\Gamma^0)$, we can re-write the time-correlation function of X, defined in Eq. (6.7), as:

$$\begin{aligned} C_{XX}(t) &= \langle \delta X(\Gamma_0) \cdot \overline{\delta X}(t\,|\,\Gamma_0) \rangle_{eq} \\ &= \int d\Gamma_0 P_{eq}(\Gamma_0)(X(\Gamma_0) - X_{eq}) \int d\Gamma P(\Gamma, t\,|\,\Gamma_0)(X(\Gamma) - X_{eq}), \end{aligned}$$

Eq. (6.9)

where $C_{XX}(t=0) = \Delta_{X,eq}$ and $C_{XX}(t \to \infty) = 0$. A concept of an effective relaxation time (τ_X) of X is frequently adopted as the time integration of the normalized self-correlation function $c_{XX}(t) \equiv C_{XX}(t) / \Delta_{X,eq}$:

$$\tau_X \equiv \int_0^\infty c_{XX}(t) dt,$$

Eq. (6.10)

based on the approximation that $c_{XX}(t) \approx e^{-t/\tau_X}$.

The dynamical correlation between two different quantities X and Y that fluctuate around their prospective equilibrium values (X_{eq} and Y_{eq} can be quantitatively formulated in terms of a cross-correlation function $C_{XY}(t)$:

$$C_{XY}(t) \equiv \langle \delta X(0) \cdot \delta Y(t) \rangle_{eq} = \langle (X(0) - X_{eq}) \cdot (Y(t) - Y_{eq}) \rangle_{eq},$$

Eq. (6.11)

and this cross-correlation function can be re-written using the probability distribution function $P(\Gamma, t\,|\,\Gamma_0)$ of Eq. (6.3) :

$$\begin{aligned} C_{XY}(t) &= \langle \delta X(\Gamma_0) \cdot \overline{\delta Y}(t\,|\,\Gamma_0) \rangle_{eq} \\ &= \int d\Gamma_0 P_{eq}(\Gamma_0)(X(\Gamma_0) - X_{eq}) \int d\Gamma P(\Gamma, t\,|\,\Gamma_0)(Y(\Gamma) - Y_{eq}), \end{aligned}$$

Eq. (6.12)

where $C_{XY}(t \to \infty) \to [\int d\Gamma_0 (X(\Gamma_0) - X_{eq}) \cdot P_{eq}(\Gamma_0)] \cdot [\int d\Gamma P_{eq}(\Gamma) \cdot (Y(\Gamma) - Y_{eq})] = 0$. Since $C_{XY}(t = 0) = \int d\Gamma_0 P_{eq}(\Gamma_0)(X(\Gamma_0) - X_{eq}) \cdot (Y(\Gamma_o) - Y_{eq}) = \langle (X - X_{eq}) \cdot (Y - Y_{eq}) \rangle_{eq}$, the ratio $c_{XY} \equiv C_{XY}(t = 0) / \sqrt{\Delta_{X,eq} \cdot \Delta_{Y,eq}}$ is often referred as the correlation ratio, with $c_{XY} = 0$ being interpreted as that the fluctuations in X and Y are statistically uncorrelated at thermal equilibrium. It is important to emphasize that even at the condition of zero correlation ration, i.e. $c_{XY} = 0$, a cross-correlation function defined in Eq. (6.12) in not always zero at $t > 0$.

Because the self-correlation function formula in Eq. (6.9) is a special case of the cross-correlation function formula in Eq. (6.12) with $X = Y$, we present only the results of the time derivative of a the cross-correlation function here based on Eq. (6.8) and Eq. (6.12):

$$\begin{aligned}\frac{dC_{XY}(t)}{dt} &= \int d\Gamma_0 P_{eq}(\Gamma_0) \delta X(\Gamma_0) \frac{d\overline{\delta Y}(t|\Gamma_0)}{dt} \\ &= \int d\Gamma_0 P_{eq}(\Gamma_0) \delta X(\Gamma_0) \cdot \{ \sum_\mu \overline{[\frac{\partial Y}{\partial n_\mu} \cdot A_\mu]}(t|\Gamma^0) + \frac{1}{2} \sum_{\mu\nu} \overline{[\frac{\partial^2 Y}{\partial n_\mu \partial n_\nu} \cdot B_{\mu\nu}]}(t|\Gamma^0) \}\end{aligned}$$

Eq. (6.13)

where A and B are the parameters (Eq. (6.4)) of the vibration FPE (Eq. (6.3)). Using the definitions of $y_\mu \equiv \frac{\partial Y}{\partial n_\mu} \cdot A_\mu$ and $y_{\mu\nu} \equiv \frac{\partial^2 Y}{\partial n_\mu \partial n_\nu} \cdot B_{\mu\nu}$, we can re-write Eq. (6.13) in terms of the cross-correlation functions between X and y_μ and those between X and $y_{\mu\nu}$:

$$\begin{aligned}\frac{dC_{XY}(t)}{dt} &= \sum_\mu \langle \delta X(0) \cdot y_\mu(t) \rangle_{eq} + \frac{1}{2} \sum_{\mu\nu} \langle \delta X(0) \cdot y_{\mu\nu}(t) \rangle_{eq} \\ &= \sum_\mu \langle \delta X(0) \cdot \delta y_\mu(t) \rangle_{eq} + \frac{1}{2} \sum_{\mu\nu} \langle \delta X(0) \cdot \delta y_{\mu\nu}(t) \rangle_{eq} \\ &= \sum_\mu C_{Xy_\mu}(t) + \frac{1}{2} \sum_{\mu\nu} C_{Xy_{\mu\nu}}(t).\end{aligned}$$

Eq. (6.14)

Furthermore, all the higher order time derivatives of $C_{XY}(t)$ function can also be derived based on Eq. (6.14) in a recursive fashion.

Next, we summarize some key results in the case that X and Y are simply the α-th and β-th state variables n_α and n_β, with more detail on the mathematical derivation given in Appendix III. The commonly adopted concept of phonon occupation number of a vibrational mode can be generalized as the t-dependent expectation value of the state variable n_α during a thermal relaxation process, i.e. $\overline{n}_\alpha(t\,|\,\Gamma^0) \equiv \int d\Gamma n_\alpha P(\Gamma, t\,|\,\Gamma^0)$, with $\overline{n}_\alpha(t\,|\,\Gamma^0) \to n_{\alpha,eq}$ and $\Delta_\alpha(t\,|\,\Gamma^0) \equiv \overline{n_\alpha^2}(t\,|\,\Gamma^0) - \overline{n_\alpha}(t\,|\,\Gamma^0)^2 \to \Delta_{\alpha,eq}$ at the $t \to \infty$ limit. At the weak phonon scattering limit of a phonon gas model, the thermal equilibrium values of $n_{\alpha,eq}$ follow the Bose-Einstein distribution, and the corresponding statistical variances are $\Delta_{\alpha,eq} = n_{\alpha,eq}(n_{\alpha,eq}+1)$. Applying the vibration FPE (Eq. (6.3)) to Eq. (6.8), we derive the time derivatives of $\overline{n}_\alpha(t\,|\,\Gamma^0)$ and $\Delta_\alpha(t\,|\,\Gamma^0)$ as:

$$\begin{aligned} \frac{d}{dt}\overline{n_\alpha}(t\,|\,\Gamma^0) &= \int d\Gamma A_\alpha(\Gamma) P(\Gamma, t\,|\,\Gamma^0) = \overline{A_\alpha}(t\,|\,\Gamma^0) \\ \frac{d}{dt}\Delta_\alpha(t\,|\,\Gamma^0) &= \overline{B_{\alpha\alpha}}(t\,|\,\Gamma^0) + 2\cdot[\overline{n_\alpha A_\alpha}(t\,|\,\Gamma^0) - \overline{n_\alpha}(t\,|\,\Gamma^0)\cdot\overline{A_\alpha}(t\,|\,\Gamma^0)] \end{aligned}$$

Eq. (6.15)

Furthermore, using Eq. (6.11), and Eq. (6.12), we define the cross-correlation functions between the fluctuating phonon number of α-th mode and the fluctuating phonon number of β-th mode (also referred to as two-mode correlation functions) as $C_{n_\alpha n_\beta}(t) \equiv \langle \delta n_\alpha(0)\cdot\delta n_\beta(t)\rangle_{eq}$ $= \langle n_\alpha(0)\cdot n_\beta(t)\rangle_{eq} - n_{\alpha,eq}\cdot n_{\beta,eq}$, with $C_{n_\alpha n_\beta}(t=0) = \langle \delta n_\alpha \cdot \delta n_\beta\rangle_{eq} = \langle n_\alpha \cdot n_\beta\rangle_{eq} - n_{\alpha,eq}\cdot n_{\beta,eq}$. We can further define the normalized two-mode correlation functions as:

$$c_{\alpha\beta}(t) \equiv \frac{C_{n_\alpha n_\beta}(t)}{\sqrt{\Delta_{\alpha,eq}\cdot\Delta_{\beta,eq}}} = \frac{\int d\Gamma^0 P_{eq}(\Gamma^0)\delta n_\alpha(\Gamma^0)\cdot\overline{\delta n_\beta}(t\,|\,\Gamma^0)}{\sqrt{\Delta_{\alpha,eq}\cdot\Delta_{\beta,eq}}}.$$

Eq. (6.16)

Since $X = n_\alpha$ and $Y = n_\beta$, we have $y_\mu = A_\beta \cdot \delta_{\mu\beta}$ and $y_{\mu\nu} = 0$. Using Eq. (6.14), we can show that:

$$\frac{dc_{\alpha\beta}(t)}{dt} = \frac{C_{n_\alpha A_\beta}(t)}{\sqrt{\Delta_{\alpha,eq} \cdot \Delta_{\beta,eq}}} = \frac{\langle \delta n_\alpha(0) A_\beta(t) \rangle_{eq}}{\sqrt{\Delta_{\alpha,eq} \cdot \Delta_{\beta,eq}}} = \frac{\int d\Gamma^0 P_{eq}(\Gamma^0) \delta n_\alpha(\Gamma^0) \cdot \overline{A_\beta}(t \mid \Gamma^0)}{\sqrt{\Delta_{\alpha,eq} \cdot \Delta_{\beta,eq}}}. \quad \text{Eq. (6.17)}$$

Multiple-mode correlation functions can be defined in a similar fashion. For example, there is only one type of three-mode correlation function among the α -th, β -th, and γ -th mode:

$$\begin{aligned} &\langle \delta n_\alpha(0) \cdot \delta n_\beta(0) \cdot \delta n_\gamma(t) \rangle_{eq} = \int d\Gamma^0 P_{eq}(\Gamma^0) \delta n_\alpha(\Gamma^0) \cdot \delta n_\beta(\Gamma^0) \cdot \overline{\delta n_\gamma}(t \mid \Gamma^0) \\ &= \int d\Gamma^0 P_{eq}(\Gamma^0)(n_\alpha(\Gamma^0) - n_{\alpha,eq}) \cdot (n_\beta(\Gamma^0) - n_{\beta,eq}) \int d\Gamma P(\Gamma, t \mid \Gamma^0)(n_\gamma(\Gamma) - n_{\gamma,eq}), \end{aligned} \quad \text{Eq. (6.18)}$$

and there are three types of four-mode correlation functions among four (α , β , μ , and ν) modes:

$$\begin{aligned} &\langle \delta n_\alpha(0) \delta n_\beta(0) \delta n_\mu(0) \delta n_\nu(t) \rangle_{eq} = \int d\Gamma^0 P_{eq}(\Gamma^0) \delta n_\alpha(\Gamma^0) \cdot \delta n_\beta(\Gamma^0) \cdot \delta n_\mu(\Gamma^0) \cdot \overline{\delta n_\nu}(t \mid \Gamma^0) = \\ &\int d\Gamma^0 P_{eq}(\Gamma^0)(n_\alpha(\Gamma^0) - n_{\alpha,eq}) \cdot (n_\beta(\Gamma^0) - n_{\beta,eq}) \cdot (n_\mu(\Gamma^0) - n_{\mu,eq}) \int d\Gamma P(\Gamma, t \mid \Gamma^0)(n_\nu(\Gamma) - n_{\nu,eq}), \end{aligned} \quad \text{Eq. (6.19)}$$

$$\begin{aligned} &\langle \delta n_\alpha(0) \delta n_\beta(0) \delta n_\mu(t) \delta n_\nu(t) \rangle_{eq} = \int d\Gamma^0 P_{eq}(\Gamma^0) \delta n_\alpha(\Gamma^0) \cdot \delta n_\beta(\Gamma^0) \cdot \overline{\delta n_\mu \cdot \delta n_\nu}(t \mid \Gamma^0) = \\ &\int d\Gamma^0 P_{eq}(\Gamma^0)(n_\alpha(\Gamma^0) - n_{\alpha,eq}) \cdot (n_\beta(\Gamma^0) - n_{\beta,eq}) \int d\Gamma P(\Gamma, t \mid \Gamma^0)(n_\mu(\Gamma) - n_{\mu,eq}) \cdot (n_\nu(\Gamma) - n_{\nu,eq}), \end{aligned} \quad \text{Eq. (6.20)}$$

$$\begin{aligned} &\langle \delta n_\alpha(0) \delta n_\beta(t) \delta n_\mu(t) \delta n_\nu(t) \rangle_{eq} = \int d\Gamma^0 P_{eq}(\Gamma^0) \delta n_\alpha(\Gamma^0) \cdot \overline{\delta n_\beta \cdot \delta n_\mu \cdot \delta n_\nu}(t \mid \Gamma^0) = \\ &\int d\Gamma^0 P_{eq}(\Gamma^0)(n_\alpha(\Gamma^0) - n_{\alpha,eq}) \int d\Gamma P(\Gamma, t \mid \Gamma^0)(n_\beta(\Gamma) - n_{\beta,eq}) \cdot (n_\mu(\Gamma) - n_{\mu,eq}) \cdot (n_\nu(\Gamma) - n_{\nu,eq}). \end{aligned} \quad \text{Eq. (6.21)}$$

Within the phonon gas model, the fluctuations of phonon occupation numbers at two different modes are considered to be statistically independent at a thermal equilibrium, i.e. $< n_\alpha \cdot n_\beta >_{eq} = n_{\alpha eq} \cdot n_{\beta eq}$ for $\alpha \neq \beta$. As a result, the values of the normalized time-correlation function at $t = 0$ are simply $c_{\alpha\beta}(t = 0) = \delta_{\alpha\beta}$, where $\delta_{\alpha\beta}$ is the Kronecker-δ symbol. Yet, the phonon gas model does not state the value of a cross-correlation function Eq. (6.16) at any other time $t \neq 0$, except that $c_{\alpha\beta}(t) \to 0$ as $t \to \infty$. Multiple-mode correlation functions remain poorly understood, even within the phonon gas model.

6.2.3 Ornstein-Uhlenbeck process

The FPE for a well-studied class of stochastic processes, the so-called Ornstein-Uhlenbeck (OU) processes [100], can be solved analytically. To demonstrate the properties of these OU processes, we start with a new set of zero-mean and unit-variance stochastic variables $\tilde{\Gamma} = (x_1, x_2, x_3, \cdots, x_N)$, i.e. $\langle x_\lambda \rangle_{eq} = 0$ and $\langle {x_\lambda}^2 \rangle_{eq} = 1$. The OU processes are defined in terms of their specific form of drift and diffusion coefficients: $A_\lambda(\tilde{\Gamma}) = -\gamma_\lambda x_\lambda$ and $B_{\lambda\lambda'}(\tilde{\Gamma}) = 2\gamma_\lambda \delta_{\lambda,\lambda'}$, with $\gamma_\lambda > 0$. Consequently, the Fokker-Planck equation for an OU type processes can be re-written in a separable multiple-variable partial differential equation:

$$\frac{\partial P(\tilde{\Gamma}, t \,|\, \tilde{\Gamma}^0)}{\partial t} = \sum_{\lambda=1}^{N} \gamma_\lambda [1 + x_\lambda \cdot \frac{\partial}{\partial x_\lambda} + \frac{\partial^2}{\partial x_\lambda^2}] P(\tilde{\Gamma}, t \,|\, \tilde{\Gamma}^0), \qquad \text{Eq. (6.22)}$$

and its solution can be expresses as:

$$P(\tilde{\Gamma}, t \,|\, \tilde{\Gamma}^0) = \prod_{\lambda=1}^{N} \frac{1}{\sqrt{2\pi\Delta_\lambda(t)}} e^{-\frac{[x_\lambda - \overline{x_\lambda}(t)]^2}{2\Delta_\lambda(t)}}, \qquad \text{Eq. (6.23)}$$

where, $\overline{x_\lambda}(t) = x_\lambda(\tilde{\Gamma}^0) \cdot e^{-\gamma_\lambda t}$. and $\Delta_\lambda(t) = 1 - e^{-2\gamma_\lambda t}$. More details on the solution of an OU type FPE can be found in Appendix IV. Here we highlight one key result of the time-correlation between any two state variables x_λ and $x_{\lambda'}$ of an OU type process:

$$\tilde{C}_{\lambda\lambda'}(t) = \langle x_\lambda(t') \cdot x_{\lambda'}(t' + t) \rangle_{eq} = \delta_{\lambda,\lambda'} e^{-\gamma_\lambda t}. \qquad \text{Eq. (6.24)}$$

More interesting results on the multiple variable correlation functions, such as the three-variable correlation functions: $\langle x_{\lambda}(t') \cdot x_{\lambda'}(t') \cdot x_{\lambda''}(t'+t)\rangle_{eq}$, $\langle x_{\lambda}(t') \cdot x_{\lambda'}(t'+t) \cdot x_{\lambda''}(t'+t)\rangle_{eq}$, and the four-variable correlation functions $\langle x_{\lambda}(t') \cdot x_{\lambda'}(t') \cdot x_{\lambda''}(t') \cdot x_{\lambda'''}(t'+t)\rangle_{eq}$ and $\langle x_{\lambda}(t') \cdot x_{\lambda'}(t') \cdot x_{\lambda''}(t'+t) \cdot x_{\lambda'''}(t'+t)\rangle_{eq}$, $\langle x_{\lambda}(t') \cdot x_{\lambda'}(t'+t) \cdot x_{\lambda''}(t'+t) \cdot x_{\lambda'''}(t'+t)\rangle_{eq}$, are presented in Appendix IV.

For a lattice vibration to be classified as an OU process, its set of drift coefficients $A(\Gamma)$ in the vibration FPE (Eq. 3) must satisfy the following conditions:

$$
\begin{aligned}
A_{\alpha}(\Gamma) &= -\sum_{\beta} \mathcal{D}_{\alpha\beta} \left(\frac{\Delta_{\alpha,eq}}{\Delta_{\beta,eq}}\right)^{1/2} (n_{\beta} - n_{\beta,eq}), \\
\frac{d\overline{n_{\alpha}}(t \mid \Gamma^{0})}{dt} &= -\sum_{\beta} \mathcal{D}_{\alpha\beta} \left(\frac{\Delta_{\alpha,eq}}{\Delta_{\beta,eq}}\right)^{1/2} (\overline{n_{\beta}}(t \mid \Gamma^{0})) - n_{\beta,eq}).
\end{aligned}
$$

Eq. (6.25)

Here $\mathcal{D}_{\alpha\beta}$ are matrix elements of the normalized drift matrix $\mathcal{D}$, $n_{\alpha,eq}$ and $\Delta_{\alpha,eq}$ are respectively the equilibrium average value of the phonon number at α -th mode and the corresponding statistical variance at the equilibrium, and $\alpha, \beta = 1, 2, 3, \cdots, N$.

The $\mathcal{D}$ matrix, as defined inEq. (6.25), is a positive definite, real, and symmetric $N \times N$ matrix with a set of N eigenvalues γ_{λ} and corresponding normalized eigenvectors written as as $\vec{u}_{\lambda} = (u_{\lambda,1}, u_{\lambda,2}, u_{\lambda,3}, \cdots, u_{\lambda,N})$ for $\lambda = 1, 2, 3, \cdots, N$. We then can transform the N -dimensional phonon number state variables $\Gamma = \{n_1, n_2, \cdots, n_N\}$ into an equivalent set of zero-mean and unit-variance state variables $\tilde{\Gamma} = (x_1, x_2, x_3, \cdots, x_N)$ using this set of eigenvectors:

$$
\begin{aligned}
n_{\alpha} \quad &= n_{\alpha,eq} + (\Delta_{\alpha,eq})^{1/2} \sum_{\lambda=1}^{N} x_{\lambda} u_{\lambda,\alpha}, \\
x_{\lambda} \quad &= \sum_{\alpha=1}^{N} \frac{n_{\alpha} - n_{\alpha,eq}}{\Delta_{\alpha,eq}^{1/2}} u_{\lambda,eq}.
\end{aligned}
$$

Eq. (6.26)

The linear transformation shown Eq. (6.26) also shows that the diffusion $B_{\alpha\beta}(\Gamma)$ coefficients for an OU type lattice vibration that are related to its drift coefficients $A_{\alpha}(\Gamma)$ through the $\mathcal{D}$ matrix:

$$B_{\alpha\beta}(\Gamma) = 2(\Delta_{\alpha,eq} \cdot \Delta_{\beta,eq})^{1/2} \sum_{\lambda=1}^{N} \gamma_{\lambda} u_{\lambda,\alpha} u_{\lambda,\beta} = 2(\Delta_{\alpha,eq} \cdot \Delta_{\beta,eq})^{1/2} \mathcal{D}_{\alpha\beta}. \quad \text{Eq. (6.27)}$$

In the rest of the paper, the $\mathcal{D}$ matrix is referred as the normalized drift/diffusion matrix.

Combining the results in Eq. (6.16), Eq. (6.24), and Eq. (6.26), we can show that the normalized two-mode correlation functions $c_{\alpha\beta}(t)$ (Eq. (6.16)) in this OU type lattice vibration are simply:

$$c_{\alpha\beta}(t) = \sum_{\lambda=1}^{N} e^{-\gamma_{\lambda} t} u_{\lambda,\alpha} u_{\lambda,\beta}, \quad \text{Eq. (6.28)}$$

with $c_{\alpha\beta}(t=0) = \sum_{\lambda=1}^{N} u_{\lambda,\alpha} u_{\lambda,\beta} = \delta_{\alpha\beta}$. We can generalize the normalized two-mode correlation functions in Eq. (6.28) in an integral form:

$$c_{\alpha\beta}(t) = \int_0^{\infty} d\gamma \chi_{\alpha\beta}(\gamma) e^{-\gamma \cdot t}, \quad \text{Eq. (6.29)}$$

with $\chi_{\alpha\beta}(\gamma) = \sum_{\lambda=1}^{N} u_{\lambda,\alpha} u_{\lambda,\beta} \cdot \delta(\gamma - \gamma_{\lambda})$. Eq. (6.29) indicates that a mode correlation function $c_{\alpha\beta}(t)$ can be viewed as the t-space Laplace transformation of the γ-space function $\chi_{\alpha\beta}(\gamma)$. We refer to $\chi_{\alpha\beta}(\gamma)$ as the Laplace spectral function of $c_{\alpha\beta}(t)$. At the $N \to \infty$ limit, a Laplace spectral function $\chi_{\alpha\beta}(\gamma)$ converges to a continuous function defined in the spectral regime of $[0, \gamma_{max}]$. The k-th moment of a $\chi_{\alpha\beta}(\gamma)$ function, defined as $\mu_{\alpha\beta}(k) \equiv \int_0^{\infty} d\gamma \chi_{\alpha\beta}(\gamma) \cdot \gamma^k$, is given as:

$$\mu_{\alpha\beta}(k) = \sum_{\lambda=1}^{N} u_{\lambda,\alpha} u_{\lambda,\beta} \cdot \gamma_{\lambda}{}^{k} = < \alpha | \mathcal{D}^k | \beta > = (\mathcal{D}^k)_{\alpha\beta}. \quad \text{Eq. (6.30)}$$

The results shown in Eq. (6.28) and Eq. (6.29) clearly demonstrate that in general the normalized mode self-correlaltion functions of lattice vibration do not decay as an exponetial function of time, and the time-integral of the cross-correlaltion functions are not zero for two different modes. Some recent simulation studies [97] have reported their implementation based on fitting the MD simulated mode self-correlation functions based on an assumed formula of $C_{\alpha\beta}(t) \approx \Delta_{\alpha,eq} \cdot \delta_{\alpha,\beta} \cdot e^{-\gamma_\alpha t}$, and they reported the fitted decay factors γ_α as the inverse of phonon life-times $\tau_\alpha = \gamma_\alpha^{-1}$ in the phonon gas model. For such a simplification to be valid, the normalized drift/diffusion matrix $\mathcal{D}$ has to be close to a diagonal matrix:

$$\mathcal{D} \approx \begin{bmatrix} \gamma_1 & 0 & 0 & \dots & 0 \\ 0 & \gamma_2 & 0 & \dots & 0 \\ \vdots & \vdots & \vdots & \ddots & \vdots \\ 0 & 0 & 0 & \dots & \gamma_N \end{bmatrix} \Leftrightarrow \quad \mathcal{D}^{-1} \approx \begin{bmatrix} \tau_1 & 0 & 0 & \dots & 0 \\ 0 & \tau_2 & 0 & \dots & 0 \\ \vdots & \vdots & \vdots & \ddots & \vdots \\ 0 & 0 & 0 & \dots & \tau_N . \end{bmatrix}$$

Eq. (6.31)

However, the off-diagonal terms in the $\mathcal{D}$ matrix characterize the phonon-phonon mode scatterings, and they are usually not zero even within the approximation of the phonon gas model. Similarly, the cross-correlation functions between two vibrational modes are usually not zero even within the approximation of the phonon gas model.

The analytical solution of the probability function of an OU type vibration FPE also predicts the time-correlation functions of multiple vibrational modes. For example, based on the derivation in Appendix II.1, all the correlation functions of odd-number vibrational modes are zero for an OU type lattice. There are three types of four-mode correlation functions:

$$\begin{aligned} &\langle \delta n_\alpha(0) \delta n_\beta(0) \delta n_\mu(0) \delta n_\nu(t) \rangle_{eq} = (\Delta_{\alpha,eq} \Delta_{\beta,eq} \Delta_{\mu,eq} \Delta_{\nu,eq})^{\frac{1}{2}} \\ &\cdot \sum_{\lambda\lambda'\lambda''\lambda'''} (u_{\lambda,\alpha} u_{\lambda',\beta} u_{\lambda'',\mu} u_{\lambda''',\nu}) \cdot \langle x_\lambda(0) \cdot x_{\lambda'}(0) \cdot x_{\lambda''}(0) \cdot x_{\lambda'''}(t) \rangle_{eq} \\ = \quad &(\Delta_{\alpha,eq} \Delta_{\beta,eq} \Delta_{\mu,eq} \Delta_{\nu,eq})^{\frac{1}{2}} \cdot [\delta_{\alpha\mu} c_{\beta\nu}(t) + \delta_{\beta\mu} c_{\alpha\nu}(t) + \delta_{\alpha\beta} c_{\mu\nu}(t)], \end{aligned}$$

Eq. (6.32)

$$
\begin{aligned}
&\langle \delta n_\alpha(0)\delta n_\beta(t)\delta n_\mu(t)\delta n_\nu(t)\rangle_{eq} = (\Delta_{\alpha,eq}\Delta_{\beta,eq}\Delta_{\mu,eq}\Delta_{\nu,eq})^{\frac{1}{2}} \\
&\cdot \sum_{\lambda\lambda'\lambda''\lambda'''} (u_{\lambda,\alpha}u_{\lambda',\beta}u_{\lambda'',\mu}u_{\lambda''',\nu}) \cdot \langle x_\lambda(0)\cdot x_{\lambda'}(t)\cdot x_{\lambda''}(t)\cdot x_{\lambda'''}(t)\rangle_{eq} \\
= \;\; &(\Delta_{\alpha,eq}\Delta_{\beta,eq}\Delta_{\mu,eq}\Delta_{\nu,eq})^{\frac{1}{2}} \cdot [\delta_{\mu\nu}c_{\alpha\beta}(t) + \delta_{\beta\nu}c_{\alpha\mu}(t) + \delta_{\beta\mu}c_{\alpha\nu}(t)],
\end{aligned}
$$

Eq. (6.33)

$$
\begin{aligned}
&\langle \delta n_\alpha(0)\delta n_\beta(0)\delta n_\mu(t)\delta n_\nu(t)\rangle_{eq} = (\Delta_{\alpha,eq}\Delta_{\beta,eq}\Delta_{\mu,eq}\Delta_{\nu,eq})^{\frac{1}{2}} \\
&\cdot \sum_{\lambda\lambda'\lambda''\lambda'''} (u_{\lambda,\alpha}u_{\lambda',\beta}u_{\lambda'',\mu}u_{\lambda''',\nu}) \cdot \langle x_\lambda(0)\cdot x_{\lambda'}(0)\cdot x_{\lambda''}(t)\cdot x_{\lambda'''}(t)\rangle_{eq} \\
= \;\; &(\Delta_{\alpha,eq}\Delta_{\beta,eq}\Delta_{\mu,eq}\Delta_{\nu,eq})^{\frac{1}{2}} \cdot [\delta_{\alpha\beta}\delta_{\mu\nu} + c_{\alpha\mu}(t)\cdot c_{\beta\nu}(t) + c_{\alpha\nu}(t)\cdot c_{\beta\mu}(t)],
\end{aligned}
$$

Eq. (6.34)

with $c_{\alpha\beta}(t)$ being the normalized time-correlation function between α -th mode and β -mode (Eq. (6.16), Eq. (6.28), and Eq. (6.29)), and the initial values of the four-mode time correlation functions derived as

$$\langle \delta n_\alpha(0)\delta n_\beta(0)\delta n_\mu(0)\delta n_\nu(0)\rangle_{eq} = (\Delta_{\alpha,eq}\Delta_{\beta,eq}\Delta_{\mu,eq}\Delta_{\nu,eq})^{\frac{1}{2}} \cdot [\delta_{\alpha\beta}\delta_{\mu\nu} + \delta_{\alpha\mu}\delta_{\beta\nu} + \delta_{\alpha\nu}\delta_{\beta\mu}]. \quad \text{Eq. (6.35)}$$

6.3 Lattice Thermal Conductivity

6.3.1 Green-Kubo theory

The fluctuation-dissipation theorem provides a general statistical theory to connect the equilibrium fluctuation processes of a macroscopic quantity e.g. the total heat current vector $\vec{J} = (J_x, J_y, J_z)$ in a solid and the related irreversible transport processes, such as heat conduction at non-equilibrium conditions. Within the statistical linear response transport theory, the thermal conductivity tensor κ_{IJ}, with $I, J = x, y, z$ labeling the Cartesian axes, is expressed in the Green-Kubo formula in terms of the time integral of the current-current correlation functions[87][88]:

$$\kappa_{IJ} = \frac{1}{k_B T^2 \Omega N_{cell}} \int_0^{\infty} dt \langle J_I(0) J_J(t) \rangle_{eq},$$ Eq. (6.36)

where Ω and N_{cell} are respectively volume of the unit-cell and total number of cells in a super-cell model with the Born-von Karman periodic boundary.

At the atomistic level, the heat current $\vec{J}$ is a function of atomic forces, displacements and momenta, and various approximations have been proposed and discussed [101]. Assuming the heat current vector is also a function of phonon numbers of modes, i.e. $\vec{J} = \vec{J}(\{\Gamma\}) = \vec{J}(n_1, n_2, n_3, \cdots, n_N)$, we can use Eq. (6.9) to evaluate the current-current correlation functions. Under the condition of small thermal fluctuation, the Cartesian components of the heat current vector can be simplified as:

$$J_I \approx \sum_{\alpha} \frac{\partial J_I}{\partial \Delta n_\alpha} \Delta n_\alpha = \sum_i \Lambda_{I\alpha} \Delta n_\alpha .$$ Eq. (6.37)

The seminal Peierls formula of the heat current of a phonon gas, $\vec{J} = \sum_\alpha \Delta n_\alpha \hbar \omega_\alpha \vec{v}_\alpha$, is an approximation of this class, with $\Lambda_{I\alpha} = \hbar \omega_\alpha v_{\alpha I}$. When the higher order terms(also referred as the non-harmonic terms) in the J formula are included as the corrections to the linear terms formulated in Eq. (6.37), we can rewrite the J_I as $J_I = \sum_i \Lambda_{I\alpha} \Delta n_\alpha + \delta J_I$. Consequently, the current-current correlation functions can be expressed as:

$$\begin{aligned} \langle J_I(0) J_J(t) \rangle_{eq} &= \sum_{\alpha\beta} \Lambda_{I\alpha} \Lambda_{J\beta} \langle \Delta n_\alpha(0) \Delta n_\beta(t) \rangle_{eq} \\ &+ \sum_{\alpha} \Lambda_{I\alpha} \langle \Delta n_\alpha(0) \delta J_J(t) \rangle_{eq} \\ &+ \sum_{\alpha} \Lambda_{J\alpha} \langle \delta J_I(0) \Delta n_\alpha(t) \rangle_{eq} \\ &+ \langle \delta J_I(0) \delta J_J(t) \rangle_{eq} \end{aligned}$$ Eq. (6.38).

Wherever the non-harmonic $\delta\vec{J}$ terms in the vibrational heat current in a lattice are not negligible, time-correlation functions of multiple modes, such as the four-mode correlation functions shown in Eq. (6.32), Eq. (6.33) and Eq. (6.34), are needed to evaluate the current-current correlation function shown in Eq. (6.38). At the condition that the general linear approximation of Eq. (6.37) is valid, the time integral of $\langle J_I(0)J_J(t)\rangle_{eq}$ is approximated in terms of time-integrals of normalized two-mode correlation functions $c_{\alpha\beta}(t)$:

$$\begin{aligned}\int_0^\infty dt\langle J_I(0)J_J(t)\rangle_{eq} &\approx \sum_{\alpha\beta}\Lambda_{I\alpha}\Lambda_{J\beta}\int_0^\infty dt\langle \Delta n_\alpha(0)\Delta n_\beta(t)\rangle_{eq} \\ &= \sum_{\alpha\beta}\Lambda_{I\alpha}\Lambda_{J\beta}(\Delta_{\alpha,eq}\cdot\Delta_{\beta,eq})^{1/2}\int_0^\infty dt c_{\alpha\beta}(t)\end{aligned} \qquad \text{Eq. (6.39)}$$

Based on the GK formula, we now express κ_{Latt} in the form of:

$$\kappa_{IJ} = \frac{1}{k_B T^2 \Omega N_{Cell}}\sum_{\alpha\beta}\Lambda_{I\alpha}\Lambda_{J\beta}(\Delta_{\alpha,eq}\cdot\Delta_{\beta,eq})^{1/2}\int_0^\infty dt c_{\alpha\beta}(t). \qquad \text{Eq. (6.40)}$$

As shown in Eq. (6.28) of Sec. 6.2.3, when a lattice vibration can be approximated as an Ornstein-Uhlenbeck process, the lattice thermal conductivity is simply:

$$\begin{aligned}\kappa_{IJ} &= \frac{1}{k_B T^2 \Omega N_{Cell}}\sum_{\alpha\beta}\Lambda_{I\alpha}\Lambda_{J\beta}(\Delta_{\alpha,eq}\cdot\Delta_{\beta,eq})^{1/2}\sum_{\lambda=1}^{N}\int_0^\infty dt e^{-\gamma_\lambda t}u_{\lambda,\alpha}u_{\lambda,\beta} \\ &= \frac{1}{k_B T^2 \Omega N_{Cell}}\sum_{\alpha\beta}\Lambda_{I\alpha}\Lambda_{J\beta}(\Delta_{\alpha,eq}\cdot\Delta_{\beta,eq})^{1/2}\sum_{\lambda=1}^{N}(\gamma_\lambda)^{-1}u_{\lambda,\alpha}u_{\lambda,\beta} \\ &= \frac{1}{k_B T^2 \Omega N_{Cell}}\sum_{\alpha\beta}\Lambda_{I\alpha}\Lambda_{J\beta}(\Delta_{\alpha,eq}\cdot\Delta_{\beta,eq})^{1/2}(\mathcal{D})^{-1}_{\alpha\beta}\end{aligned} \qquad \text{Eq. (6.41)}$$

6.3.2 Phonon Boltzmann transport equation

As a kinetic transport theory, the phonon BTE theory is valid only within the phonon gas approximation, i.e. at a thermal equilibrium, each mode oscillates at a harmonic frequency ω and the ensemble averaged number of phonons at this mode follows the Bose-Einstein distribution

$n_{eq}(\omega) = \langle n \rangle_{eq} = \frac{1}{e^{(\hbar\omega/k_B T)} - 1}$ and $\Delta_{eq} = \langle n^2 \rangle_{eq} - \langle n \rangle_{eq}^2 = n_{eq} \cdot (n_{eq} + 1)$. In addition, the phonon BTE theory applies only to a crystalline solid, where each vibrational mode of this translation-invariant periodic lattice corresponds to a definite reciprocal-space $\vec{k}$ vector and a definite group velocity $\vec{v} = \vec{\nabla}_k(\omega)$.

When a constant temperature gradient $\vec{\nabla}_r T$ is imposed on the periodic lattice , the ensemble averaged phonon numbers, n_α for $\alpha = 1, 2, 3, \cdots, N$, are no longer able to relax back to their original equilibrium values $n_{eq,\alpha}$ as a result of thermal diffusion. Instead, each n_α approaches a space-dependent value when a steady-state is reached:

$$\left(\frac{\partial n_\alpha}{dt}\right) = -\left(\frac{dn_\alpha}{dt}\right)_{diffusion} - \left(\frac{dn_\alpha}{dt}\right)_{scattering} = 0 \qquad \text{Eq. (6.42)}$$

where the diffusion term at the $\vec{\nabla}_r T \to 0$ limit is approximated as

$$\left(\frac{dn_\alpha}{dt}\right)_{diffusion} = -\vec{v}_\alpha \cdot \vec{\nabla}_r n_\alpha \simeq -\frac{\hbar\omega_\alpha}{k_B T^2} n_{\alpha,eq}(n_{\alpha,eq}+1)\vec{v}_\alpha \cdot \vec{\nabla}_r T. \qquad \text{Eq. (6.43)}$$

A common approximation for the scattering terms in the phonon BTE (Eq. 41) is the so-called linearized approximation:

$$\left(\frac{dn_\alpha}{dt}\right)_{scattering} \simeq -\sum_{\beta=1}^{N} \sqrt{\frac{n_{\alpha,eq}\cdot(n_{\alpha,eq}+1)}{n_{\beta,eq}\cdot(n_{\beta,eq}+1)}} \cdot \mathcal{L}_{\alpha\beta} \cdot (n_\beta - n_{\beta,eq}) \qquad \text{Eq. (6.44)}$$

where $\mathcal{L}$ is referred as the linear phonon scattering matrix.

Using the results of Eq. (6.43) and Eq. (6.44) and the definition of $\phi_\alpha \equiv \frac{n_\alpha - n_{\alpha,eq}}{\sqrt{n_{\alpha,eq} \cdot (n_{\alpha,eq}+1)}}$, the steady-state phonon Boltzmann equation (Eq. (6.42)) can be re-written as a set of linear equations for ϕ_α with $\alpha = 1, 2, 3, \cdots, N$:

$$\sum_{\beta=1}^{N}\mathcal{L}_{\alpha\beta}\cdot\phi_{\beta}=-\frac{\hbar\omega_{\alpha}}{k_{B}T^{2}}\sqrt{n_{\alpha,eq}(n_{\alpha,eq}+1)}\vec{v}_{\alpha}\cdot\vec{\nabla}_{r}T.$$

Eq. (6.45)

Similar to what we have derived in Sec. 6.2.3, we can solve the set of linear equations using the eigenvectors and the eigenvalues of the matrix $\mathbf{L}$:

$$\begin{aligned}\phi_{\alpha}&=-\sum_{\lambda=1}^{N}\gamma_{\lambda}{}^{-1}u_{\lambda,\alpha}\sum_{\beta=1}^{N}\frac{\hbar\omega_{\beta}}{k_{B}T^{2}}\sqrt{n_{\beta,eq}(n_{\beta,eq}+1)}(\vec{v}_{\beta}\cdot\vec{\nabla}_{r}T)u_{\lambda,\beta}\\&=-\sum_{\beta=1}^{N}(\sum_{\lambda=1}^{N}\gamma_{\lambda}{}^{-1}u_{\lambda,\alpha}u_{\lambda,\beta})\cdot\frac{\hbar\omega_{\beta}}{k_{B}T^{2}}\sqrt{n_{\beta,eq}(n_{\beta,eq}+1)}(\vec{v}_{\beta}\cdot\vec{\nabla}_{r}T)\\&=-\sum_{\beta=1}^{N}(\mathcal{L})_{\alpha\beta}^{-1}\cdot\frac{\hbar\omega_{\beta}}{k_{B}T^{2}}\sqrt{n_{\beta,eq}(n_{\beta,eq}+1)}(\vec{v}_{\beta}\cdot\vec{\nabla}_{r}T),\end{aligned}$$

Eq. (6.46)

where γ_{λ} and $\vec{u}_{\lambda}$ are the λ-th eigenvalue and eigenvector of the matrix $\mathcal{L}$, and $(\mathcal{L})^{-1}$ represents the inverse matrix of $\mathcal{L}$.

Based on the Peierls formula for the heat current of a phonon gas, the lattice thermal conductivity predicted by the linearized phonon BTE theory can be expressed as:

$$\begin{aligned}\kappa_{IJ}&=\frac{1}{\Omega N_{Cell}}\sum_{\alpha\beta}(\mathbf{L})_{\alpha\beta}^{-1}\cdot\frac{\sqrt{n_{\alpha,eq}(n_{\alpha,eq}+1)}\sqrt{n_{\beta,eq}(n_{\beta,eq}+1)}\hbar\omega_{\alpha}\hbar\omega_{\beta}}{k_{B}T^{2}}v_{\alpha I}\cdot v_{\beta J}\\&=\frac{1}{\Omega N_{Cell}}\sum_{\alpha\beta}(c_{\alpha}c_{\beta})^{1/2}\cdot v_{\alpha I}\cdot v_{\beta J}\cdot(\mathbf{L})_{\alpha\beta}^{-1},\end{aligned}$$

Eq. (6.47)

where $c=k_{B}\cdot(\frac{\hbar\omega}{k_{B}T})^{2}\cdot n_{\alpha,eq}\cdot(n_{\alpha,eq}+1)$ is the single mode heat capacity.

To compare κ_{Latt} predicted by the phonon BTE (Eq. (6.47)) and the one by the Ornstein-Uhlenbeck type vibration FPE (Eq. (6.41)), we first note that in the limit of weak phonon scattering of the phonon gas model, the variance of the phonon number fluctuation of a mode $\Delta_{\alpha,eq}$ has already been shown to converge to the value of $n_{\alpha,eq}\cdot(n_{\alpha,eq}+1)$, and the Peierls formula of heat current should be valid. Furthermore, if we interpret that phonon occupation number n_{α} in the phonon BTE as the time-dependent expectation value of the phonon number during the thermal relaxation process, we conclude that the normalized drift/diffusion matrix $\mathcal{D}$ in an OU type vibration FPE (Eq. (6.25)) converges to the linear phonon scattering matrix $\mathcal{L}$, i.e. $\mathcal{D} \rightarrow \mathcal{L}$, at the weak phonon scattering limit of the phonon gas approximation. Consequently, κ_{Latt} predicted by the vibration FPE (Eq. (6.41)) converges to that predicted by the conventional phonon BTE (Eq. (6.47)). The so-called single mode relaxation approximation (SMRA) or relaxation time approximation (RTA) of a kinetic transport model corresponds to the cases where the phonon scattering matrix $\mathcal{L}$ (or the drift/diffusion matrix ($\mathcal{D}$) can be treated as a positively defined diagonal matrix (Eq. (6.31)).

6.3.3 Discussion

A comparison chart is shown in Table 6-1 to highlight commonality and distinction between the atomistic MD simulation method and the vibration FPE. The MD simulation approach has an absolute advantage in simulating the atomistic scale lattice heat currents at moderate and high temperature, and it applies consistently to disordered solids, very anharmonic solids, as well as fluids. However, MD simulations only provide a semi-quantitative description of the fluctuation properties of individual vibrational modes based on the damped oscillator model. Firstly, corrections to the quantized lattice vibration have to be considered at low temperature because of the classical nature of MD simulations,. Secondly, the mode lifetimes extracted from the numerical solutions of MD trajectories over long periods of simulation time reflect only partial information on the fluctuation and relaxation processes in lattice dynamics. Because of the assumption that all the cross-mode correlation functions between two different vibrational modes are zero, the damped oscillator approximation is equivalent to the single mode relaxation approximation or relaxation time approximation in kinetic transport theories. The predicted κ_{Latt} from these approximate kinetic theories are known to be noticeably underestimated comparing to those derived from the full solutions of the phonon BTE theory at low temperature [54] or in low dimension materials [37].

In contrast, the vibration FPE approach complements the conventional MD simulation approach for conditions in which the interactions among vibrational modes are moderate, and it can be adopted to delineate the breakdown conditions of the phonon gas model in MD simulations. Based on vibration FPE, we propose that the phonon gas model applies when the OU approximation of the drift and diffusion coefficients (Eq. (6.25) and Eq. (6.27)) is valid. By considering the normalized drift/diffusion   matrix in an OU type vibration FPE equivalent to the scattering   matrix in a phonon BTE , we have proved for the first time that the   derived from the linear response transport theory converges to that from the kinetic transport theory within the phonon gas approximation.

When the interactions among vibrational modes are perturbatively small, the normalized drift/diffusion   matrix can be derived by using quantum perturbation theories for lattice vibration at low temperature. As temperature elevates to the semi-classical and classical regime, we can implement numerical algorithms to directly compute normalized drift coefficients and normalized diffusion coefficients using first-principles MD simulation methods. As these drift and diffusion coefficients are defined in the short time limit, high-performance parallel computer platforms can be utilized to distribute the computational load of such simulations in parallel. When the temperature dependence of   and   coefficients are extracted and tested with the OU approximation, we are able to not only quantitatively determine the temperature condition where the phonon gas model breaks-down, but also identify the individual vibrational modes that lead to the breakdown.

6.4 Conclusions

In summary, we have developed a vibration Fokker-Planck equation theory to describe stochastic lattice dynamics in solids. Instead of using the molecular dynamics methods to simulate the atomic trajectories (i.e. positions and velocities as functions of time), we characterize the fluctuation and relaxation processes in terms of a time-dependent, multiple-mode probability function, which evolves from an arbitrarily sampled distribution at $t=0$ to the equilibrium distribution as $t \to \infty$. The lattice properties that govern the stochastic processes at the atomistic scale are coarse-grained into two sets of parameters of a vibration FPE, the drift A and diffusion B coefficients of vibrational modes (Eq. (6.4)). At the limit of weak mode-mode interactions, these drift/diffusion coefficients can also be computed by using perturbation theory (Eq. (6.5) and Eq. (6.6)). Beyond the perturbation approximation, these coefficients can also be directly computed using MD methods, including at the conditions in which the phonon gas approximation is insufficient. Because both drift/diffusion coefficients of the vibration FPE theory are defined at the limit of $\delta t \to 0$, the intensive computational loads of MD simulations can be distributed in a parallel computer platform using massive parallel algorithms.

Our time-dependent probability theory presents a new paradigm to quantitatively compute correlation functions among vibrational modes (Eq. (6.16) and Eq. (6.17)6.). The advantages of this statistical approach is clearly demonstrated at the Ornstein-Uhlenbeck condition (Sec. 2.3), in which the vibration FPE has an analytical solution (Eq. (6.23) and Eq. (6.26)) and the correlation functions among multiple modes (Eq. (6.28), Eq. (6.32), Eq. (6.33) and Eq. (6.34)) can be derived in terms of eigenvalues and eigenvectors of the normalized drift/diffusion matrix $\mathcal{D}$ (Eq. (6.25) and Eq. (6.27)). The derived time-correlation function of lattice heat current at the level of Peierls harmonic flux model)Eq. (6.39) quantitatively illustrates the importance of counting the contributions of both self and cross correlation functions between two modes (Eq. (6.40)). This approach in principle can be extended with multiple-mode correlation function to account effects of anharmonic correction terms in heat flux [101]. Furthermore, by equating this the $\mathcal{D}$ matrix of an OU type vibration FPE with the conventional phonon scattering matrix $\mathcal{L}$ (Eq. (6.44)) of a phonon BTE, we have presented the first rigorous mathematical proof to equalize the Green-Kubo theory of κ_{Latt} (Eq. (6.36) and Eq. (6.41)) and the BTE theory of κ_{Latt} within the phonon gas model. When perturbation theory (such as Fermi's golden rule) becomes insufficient to accurately evaluate the phonon scattering matrix $\mathcal{L}$, the full set of matrix elements of $\mathcal{L}$, instead of just effective phonon lifetimes, can still be computed as the normalized drift/diffusion coefficients of an OU type FPE using the MD simulation approaches. As a results, the phonon gas model can be extended to a wider range of applications.

Based on the vibration FPE theory, we further propose a quantitative criterion to define the phonon gas approximation, i.e. the propertied of lattice vibration can be described with the phonon gas model when the drift/diffusion coefficients of this vibrating lattice satisfy the OU condition (Eq. (6.25) and Eq. (6.27)). Based on this quantitative criterion to delineate the breakdown conditions of the phonon gas model, we have established the theoretical foudation to numerically study the mechanisms of lattice thermal conduction beyond the phonon gas model. The necessary first step in the future studies is to establish a better understanding on the general functions of A and B coefficients at high temperature. Then, various numerical methods, such as adiabatic elimination of variables method, matrix continued-fraction method, or variational methods, will be adopted to solve the vibration FPE [99]. It is promising that this vibration FPE presents a new theoretical framework to accurately and effectively predict the stochastic vibrational processes and thermal transport properties beyond the phonon gas model.

Table 6-1 Comparison between MD method and FPE method

	Molecular Dynamics	**Fokker-Plank Equation**
Thermal Conductivity $\boldsymbol{\kappa}$	*Green-Kubo Formula:* $\kappa_{IJ} = \frac{1}{Vk_BT^2}\int_0^\infty < J_\alpha(0)J_\beta(t) > dt$ *,with J(t)as fluctuating heat current* *Required input: The time-correlation function of heat current* $< J_\alpha(0)J_\beta(t) >$	
Heat Current *J*	$\sum_i \mathbf{v}_i\varepsilon_i + \frac{1}{2}\sum_i\sum_{j>i}\mathbf{F}_{ij}\cdot\left(\mathbf{v}_i+\mathbf{v}_j\right)\left(\mathbf{r}_i-\mathbf{r}_j\right)$ $\mathbf{r}_i$, $\mathbf{v}_i$ *~ atomic position/ velocity* $\mathbf{F}_{ij}$ *~ inter-atomic force*	$\sum_\alpha n_\alpha h\omega\mathbf{v}_g + \Delta\mathbf{J}$ n_α *~ phonon number* $\Delta\mathbf{J}$ *~ anharmonic heat current, not yet formulated*
Dynamics	$\mathbf{F}_i = -\nabla_{\mathbf{r}_i}V\left(\mathbf{r}_1,\ldots,\mathbf{r}_n\right)$ *V ~ many-body inter-atomic potential*	$A_\alpha(\Gamma) \equiv \lim_{\delta t\to 0}\frac{1}{\delta t}\int_0^{\delta t} d\Gamma'\delta n_\alpha(\Gamma,\Gamma')P(\Gamma',\delta t\,\|\,\Gamma)$ $B_{\alpha\beta}(\Gamma) \equiv \lim_{\delta t\to 0}\frac{1}{\delta t}\int_0^{\delta t} d\Gamma'\delta n_\alpha(\Gamma,\Gamma')\delta n_\beta(\Gamma,\Gamma')P(\Gamma',\delta t\,\|\,\Gamma)$
Phonon Gas Limit	*Weak anharmoic potential:* $V = V_{harmonic} + \Delta V_{anh}$, $\Delta V_{anh} = V_{harmonic}$ *Only numerical solution for* $\mathbf{r}_i(t)$, $\mathbf{v}_i(t)$ *Normal mode analysis:* • *Long simulation time is necessary* • *Self-correlation functions* $c_{\alpha\alpha}(t)$ *often assumed to be* e^{-t/τ_α} • *Cross correlations* $c_{\alpha\beta}(t)$ *often assumed to be zero* • *Three/four-mode correlation functions rarely studied*	*Ornstein-Uhlenbeck processes:* $A_\alpha(\Gamma) = -\sum_\beta \mathcal{D}_{\alpha\beta}(\frac{\Delta_{\alpha,eq}}{\Delta_{\beta,eq}})^{1/2}(n_\beta - n_{\beta,eq})$, $B_{\alpha\beta}(\Gamma) = 2(\Delta_{\alpha,eq}\cdot\Delta_{\beta,eq})^{1/2}\mathcal{D}_{\alpha\beta}$ *Analytical solution:* $P(\tilde{\Gamma},t\,\|\,\tilde{\Gamma}^0) = \prod_{\lambda=1}^N \frac{1}{\sqrt{2\pi\Delta_\lambda(t)}}e^{-\frac{[x_\lambda - \overline{x_\lambda}(t)]^2}{2\Delta_\lambda(t)}}$ *Analytical formulas of multiple-mode time-correlation functions:* • *Two-mode:* $c_{\alpha\beta}(t) = <\delta n_\alpha(0)\cdot\delta n_\beta(t)>_{eq}\Big/\sqrt{(<\delta n_\alpha{}^2>_{eq}\cdot<\delta n_\beta{}^2>_{eq})}$ $= \sum_{\lambda=1}^N e^{-\gamma_\lambda t}u_{\lambda,\alpha}u_{\lambda,\beta} \Rightarrow \int_0^\infty d\gamma\chi_{\alpha\beta}(\gamma)e^{-\gamma\cdot t}$ with $N\to\infty$ • *Three-mode:* $\langle\delta n_\alpha(0)\delta n_\beta(0)\delta n_\mu(t)\rangle_{eq} = 0$ • *Four-mode:* $\langle\delta n_\alpha(0)\delta n_\beta(0)\delta n_\mu(0)\delta n_\nu(t)\rangle_{eq} =$ $[\delta_{\alpha\mu}c_{\beta\nu}(t)+\delta_{\beta\mu}c_{\alpha\nu}(t)+\delta_{\alpha\beta}c_{\mu\nu}(t)]\sqrt{(<\delta n_\alpha{}^2>_{eq}<\delta n_\beta{}^2>_{eq}<\delta n_\mu{}^2>_{eq}<\delta n_\nu{}^2>_{eq})}$

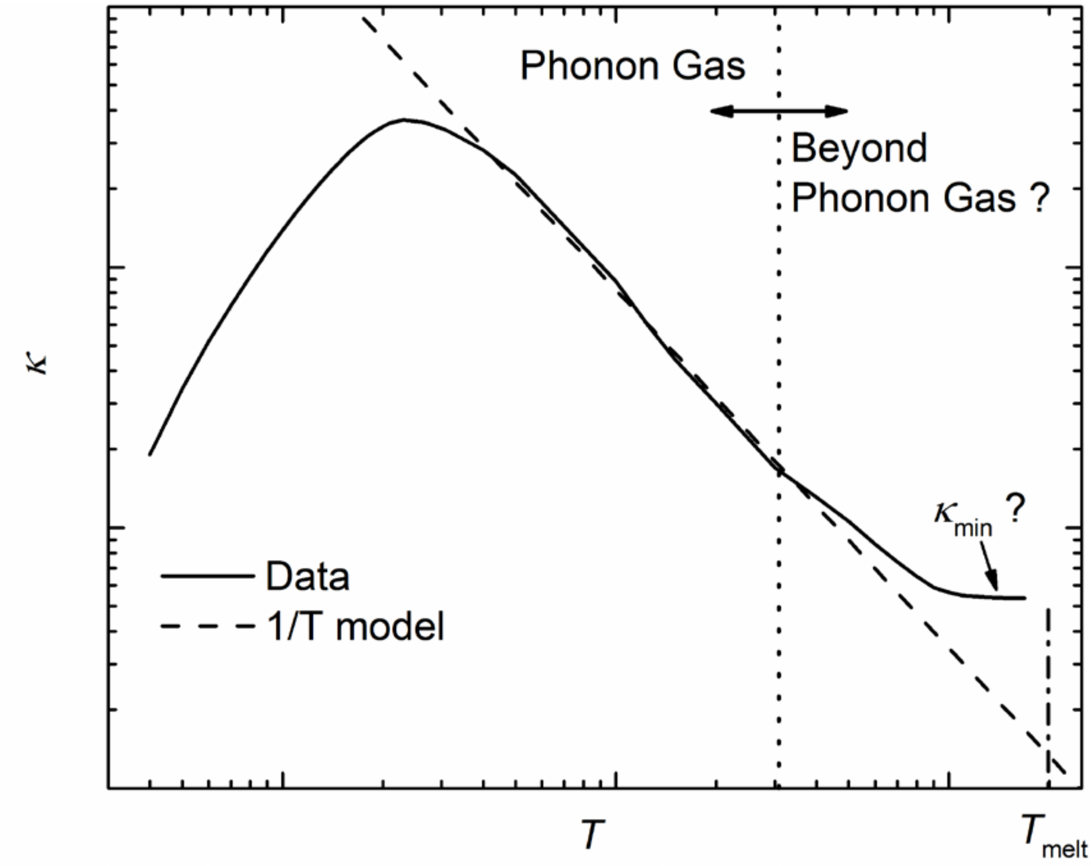

Figure 6-1 Dependence of the lattice thermal conductivity κ_{Latt} on temperature T , up to the melting temperature T_{melt}.

Chapter 7 Summary and Future Works

Future advances in energy storage is linked with the exploit of various properties of materials. In particular, thermal conductivity is always essential for selection of materials utilized in thermal energy storage system. Despite recent development of thermal conductivity measurements, the underlying mechanisms remain unknown for organic phase change materials and non-mentalis crystalline solids. This dissertation has explored the thermal transport of n-alkanes at the nanoscale, and further proposed a theory to describe the stochastic dynamics of lattice vibration. Performing MD simulations provide a detailed understating of heat transfer within and between n-alkane molecules, and the new FPE theory gives new insights on the microscopic mechanism and how correlated phonons contribute to the lattice thermal conductivity.

In Chapter 4, the mixture of long-chain n-alkanes are studied by MD simulation to illustrate the correlation between the orientation of molecules and their thermal conductivity. We demonstrate that there exists a strong correlation between the orientation factor and thermal conductivity of the n-alkane mixtures which is a result of the combination of the nearly 1-D molecular structure of long-chain n-alkanes and the huge discrepancy between the strong intra- and weak inter-molecular interactions. Basically, the directions with less number of interfaces provide a higher thermal conductivity in n-alkanes mixtures. This anisotropic heat transfer property in long-chain alkanes have barely been observed in macroscopic measurements of their thermal conductivity. Therefore, crystallization of n-alkanes from deposition in a very slow controlled growth rate is promising to create an ideal crystal of n-alkanes with strongly anisotropic effects.

This interface-dominated thermal transport in n-alkanes leads us to the discovery of the underlying fundamental mechanism in their TIC in Chapter 5. By performing MD simulations and a time-domain analysis of interfacial heat current flowing at a single molecular level to study heat transfer across a vdW force-bonded flexible interface in n-eicosane, a thermal coupling – decoupling mechanism of the thermal interfacial transfer in n-alkanes is found. Meanwhile, the interfacial heat exchange properties of a single molecule can be quantified by two parameters, the interfacial coupling time and the standard deviation of interfacial heat exchange. The inverse temperature dependence of the interfacial coupling time is the main contribution to the reduction of TIC in n-eicosane as the temperature increased. Further studies can be conducted on how the alignment angle between a single molecular chain and the normal direction of an interface affects the two interfacial parameters is the next step to quantify the morphology-TIC relation.

In Chapter 6, we proposed an FPE theory to describe the stochastic fluctuation and relaxation processes of lattice vibration over wide-ranging conditions, directly leading us to derive the time-dependent correlation function among multiple vibrational modes. This correlation function is important because of its essential position for the prediction of the lattice thermal conductivity from the Green-Kubo method. We have proven that the drift/diffusion coefficients in FPE is identical to the scattering matrix and the calculation of the lattice thermal conductivity from the Green-Kubo approach is converged to the one in phonon BTE under phonon gas mode. Further studies will focus on the combination of MD simulations and FPE, which is useful to predict the lattice thermal conductivity of crystalline solids at high temperatures when the phonon BTE breaks down.

References

[1] Don B. Fox, Daniel Sutter, and Jefferson W. Tester. "The thermal spectrum of low-temperature energy use in the United States." *Energy & Environmental Science* 4.10 (**2011**): 3731-3740.

[2] Harald Mehling, and Luisa F. Cabeza. Heat and cold storage with PCM. Berlin: Springer, **2008**.

[3] Florian Hengstberger, and Christoph Zauner"Materials Selection for Thermal Energy Storage: How to Increase the Thermal Conductivity of Phase Change Materials." *10TH International Conference on Sustainable Energy and Environmental Protection Energy Storage*. **2017**.

[4] Liwu Fan, and Jay M. Khodadadi. "Thermal conductivity enhancement of phase change materials for thermal energy storage: a review." *Renewable and Sustainable Energy Reviews* 15.1 (**2011**): 24-46.

[5] J. M. Khodadadi, Liwu Fan, and Hasan Babaei. "Thermal conductivity enhancement of nanostructure-based colloidal suspensions utilized as phase change materials for thermal energy storage: a review." *Renewable and Sustainable Energy Reviews* 24 (**2013**): 418-444.

[6] Eric T. Swartz, and Robert O. Pohl. "Thermal boundary resistance." *Reviews of Modern Physics* 61.3 (**1989**): 605.

[7] Max Born, and Kun Huang. Dynamical theory of crystal lattices. Clarendon press, **1954**.

[8] Gang Chen. Nanoscale energy transport and conversion: a parallel treatment of electrons, molecules, phonons, and photons. Oxford University Press, **2005**.

[9] Rudolf Peierls. "Zur kinetischen theorie der wärmeleitung in kristallen." *Annalen der Physik* 395.8 (**1929**): 1055-1101.

[10] John M. Ziman. Electrons and phonons: the theory of transport phenomena in solids. Oxford university press, **2001**.

[11] S. P. Srivastava, et al. "Phase-transition studies in n-alkanes and petroleum-related waxes—

A review." *Journal of Physics and Chemistry of Solids* 54.6 (**1993**): 639-670.

[12] Probjot Singh, Arm Youyen, and H. Scott Fogler. "Existence of a critical carbon number in the aging of a wax-oil gel." *AIChE journal* 47.9 (**2001**): 2111-2124.

[13] Prabir K Mukherjee. "Phase transitions among the rotator phases of the normal alkanes: A review." *Physics Reports* 588 (**2015**): 1-54.

[14] Michel Dirand et al. "Normal alkanes, multialkane synthetic model mixtures, and real petroleum waxes: crystallographic structures, thermodynamic properties, and crystallization." *Journal of Chemical & Engineering Data* 47.2 (**2002**): 115-143.

[15] Thoru Shimizu, and Takashi Yamamoto. "Melting and crystallization in thin film of n-alkanes: A molecular dynamics simulation." *The Journal of Chemical Physics* 113.8 (**2000**): 3351-3359.

[16] N. M. Waheed, S. Lavine, and G. C. Rutledge. "Molecular simulation of crystal growth in n-eicosane." *The Journal of Chemical Physics* 116.5 (**2002**): 2301-2309.

[17] Takashi Yamamoto, et al. "Molecular simulation of crystallization in n-alkane ultrathin films: Effects of film thickness and substrate attraction." *The Journal of Chemical Physics* 127.15 (**2007**): 154704.

[18] Nathaniel Wentzel, and Scott T. Milner. "Crystal and rotator phases of n-alkanes: A molecular dynamics study." *The Journal of Chemical Physic*s 132.4 (**2010**): 044901.

[19] Muhammad Anwar, Francesco Turci, and Tanja Schilling. "Crystallization mechanism in melts of short n-alkane chains." *The Journal of Chemical Physics* 139.21 (**2013**): 214904.

[20] Peng Yi, and Gregory C. Rutledge. "Molecular simulation of crystal nucleation in n-octane melts." *The Journal of Chemical Physics* 131.13 (**2009**): 134902.

[21] Peng Yi, and Gregory C. Rutledge. "Molecular simulation of bundle-like crystal nucleation

from n-eicosane melts." *The Journal of Chemical Physics* 135.2 (**2011**): 024903.

[22] Chuanfu Luo, et al. "Length-dependent segregation in crystallization of n-alkanes: MD simulations." *Journal of Non-Crystalline Solids* 407 (**2015**): 206-212.

[23] Takashi Yamamoto. "Molecular dynamics of crystallization in n-alkane mixtures; texture, compatibility, and diffusion in crystals." *Polymer* 99 (**2016**): 721-733.

[24] Asegun Henry, and Gang Chen. "High thermal conductivity of single polyethylene chains using molecular dynamics simulations." *Physical Review Letters* 101.23 (**2008**): 235502.

[25] Jun Liu, and Ronggui Yang. "Tuning the thermal conductivity of polymers with mechanical strains." *Physical Review B* 81.17 (**2010**): 174122.

[26] Tengfei Luo, et al. "Molecular dynamics simulation of thermal energy transport in polydimethylsiloxane." *Journal of Applied Physics* 109.7 (**2011**): 074321.

[27] Teng Zhang, and Tengfei Luo. "Morphology-influenced thermal conductivity of polyethylene single chains and crystalline fibers." *Journal of Applied Physics* 112.9 (**2012**): 094304.

[28] Jun Liu, and Ronggui Yang. "Length-dependent thermal conductivity of single extended polymer chains." *Physical Review B* 86.10 (**2012**): 104307.

[29] Teng Zhang, and Tengfei Luo. "High-contrast, reversible thermal conductivity regulation utilizing the phase transition of polyethylene nanofibers." *ACS nano* 7.9 (**2013**): 7592-7600.

[30] Hasan Babaei, Pawel Keblinski, and J. M. Khodadadi. "Improvement in thermal conductivity of paraffin by adding high aspect-ratio carbon-based nano-fillers." *Physics Letters A* 377.19 (**2013**): 1358-1361.

[31] Hasan Babaei, Pawel Keblinski, and J. M. Khodadadi. "Thermal conductivity enhancement of paraffins by increasing the alignment of molecules through adding CNT/graphene." *International Journal of Heat and Mass Transfer* 58.1 (**2013**): 209-216.

[32] Teng Zhang, Xufei Wu, and Tengfei Luo. "Polymer nanofibers with outstanding thermal conductivity and thermal stability: Fundamental linkage between molecular characteristics and macroscopic thermal properties." *The Journal of Physical Chemistry C* 118.36 (**2014**): 21148-21159.

[33] Rudolf Peierls. "Zur kinetischen theorie der wärmeleitung in kristallen." *Annalen der Physik* 395.8 (**1929**): 1055-1101.

[34] Xiaoli Tang, and Jianjun Dong. "Lattice thermal conductivity of MgO at conditions of Earth's interior." *Proceedings of the National Academy of Sciences* 107.10 (**2010**): 4539-4543.

[35] David A. Broido, et al. "Intrinsic lattice thermal conductivity of semiconductors from first principles." *Applied Physics Letters* 91.23 (**2007**): 231922.

[36] Alistair Ward, et al. "Ab initio theory of the lattice thermal conductivity in diamond." *Physical Review B* 80.12 (**2009**): 125203.

[37] Andrea Cepellotti and Nicola Marzari. "Thermal transport in crystals as a kinetic theory of relaxons." *Physical Review X* 6.4 (**2016**): 041013.

[38] Keivan Esfarjani, Gang Chen, and Harold T. Stokes. "Heat transport in silicon from first-principles calculations." *Physical Review B* 84.8 (**2011**): 085204.

[39] Yong Lu, Tao Sun, and Dong-Bo Zhang. "Lattice anharmonicity, phonon dispersion, and thermal conductivity of PbTe studied by the phonon quasiparticle approach." *Physical Review B* 97.17 (**2018**): 174304.

[40] Tianli Feng, Lucas Lindsay, and Xiulin Ruan. "Four-phonon scattering significantly reduces intrinsic thermal conductivity of solids." *Physical Review B* 96.16 (**2017**): 161201.

[41] Navaneetha K. Ravichandran, and David Broido. "Unified first-principles theory of thermal properties of insulators." *Physical Review B* 98.8 (**2018**): 085205.

[42] William L. Jorgensen, David S. Maxwell, and Julian Tirado-Rives. "Development and testing of the OPLS all-atom force field on conformational energetics and properties of organic liquids." *Journal of the American Chemical Society* 118.45 (**1996**): 11225-11236.

[43] Huai Sun. "COMPASS: an ab initio force-field optimized for condensed-phase applications overview with details on alkane and benzene compounds." *The Journal of Physical Chemistry B* 102.38 (**1998**): 7338-7364.

[44] Adri Van Duin, et al. "ReaxFF: a reactive force field for hydrocarbons." *The Journal of Physical Chemistry A* 105.41 (**2001**): 9396-9409.

[45] William L. Jorgensen, Jeffry D. Madura, and Carol J. Swenson. "Optimized intermolecular potential functions for liquid hydrocarbons." *Journal of the American Chemical Society* 106.22 (**1984**): 6638-6646.

[46] Marcus G. Martin, and J. Ilja Siepmann. "Transferable potentials for phase equilibria. 1. United-atom description of n-alkanes." *The Journal of Physical Chemistry B* 102.14 (**1998**): 2569-2577.

[47] Berend Smit, Sami Karaborni, and J. Ilja Siepmann. "Computer simulations of vapor–liquid phase equilibria of n-alkanes." *The Journal of Chemical Physics* 102.5 (**1995**): 2126-2140.

[48] Shyamal K. Nath, Fernando A. Escobedo, and Juan J. de Pablo. "On the simulation of vapor–liquid equilibria for alkanes." *The Journal of Chemical Physics* 108.23 (**1998**): 9905-9911.

[49] Steve Plimpton. "Fast parallel algorithms for short-range molecular dynamics." *Journal of Computational Physics* 117.1 (**1995**): 1-19. (http://lammps.sandia.gov)

[50] Shuichi Nosé. "A unified formulation of the constant temperature molecular dynamics methods." *The Journal of Chemical Physics* 81.1 (**1984**): 511-519.

[51] Rouzbeh Rastgarkafshgarkolaei. Effect of the chain on thermal conductivity and thermal

boundary conductance of long chain n-alkanes using molecular dynamics and transient plane source techniques. Masters Thesis, Department of Mechanical Engineering, Auburn University, 2014.

[52] Georg Kresse, and Jürgen Hafner. "Ab initio molecular dynamics for liquid metals." *Physical Review B* 47.1 (**1993**): 558.

[53] Paolo Giannozzi, et al. "QUANTUM ESPRESSO: a modular and open-source software project for quantum simulations of materials." *Journal of Physics: Condensed Matter* 21.39 (**2009**): 395502.

[54] Wu Li, et al. "ShengBTE: A solver of the Boltzmann transport equation for phonons." *Computer Physics Communications* 185.6 (**2014**): 1747-1758.

[55] Atsushi Togo, Laurent Chaput, and Isao Tanaka. "Distributions of phonon lifetimes in Brillouin zones." *Physical Review B* 91.9 (**2015**): 094306.

[56] Zhaohui Wang, et al. "Ultrafast flash thermal conductance of molecular chains." *Science* 317.5839 (**2007**): 787-790.

[57] Lin Hu, Tapan Desai, and Pawel Keblinski. "Determination of interfacial thermal resistance at the nanoscale." *Physical Review B* 83.19 (**2011**): 195423.

[58] Mohammad Alaghemandi, Florian Müller-Plathe, and Michael C. Böhm. "Thermal conductivity of carbon nanotube—polyamide-6, 6 nanocomposites: Reverse non-equilibrium molecular dynamics simulations." *The Journal of Chemical Physic*s 135.18 (**2011**): 11B606.

[59] Tengfei Luo, and John R. Lloyd. "Enhancement of thermal energy transport across graphene/graphite and polymer interfaces: a molecular dynamics study." *Advanced Functional Materials* 22.12 (**2012**): 2495-2502.

[60] Shangchao Lin, and Markus J. Buehler. "The effect of non-covalent functionalization on the thermal conductance of graphene/organic interfaces." *Nanotechnology* 24.16 (**2013**): 165702.

[61] Zhi Liang, William Evans, and Pawel Keblinski. "Equilibrium and nonequilibrium molecular dynamics simulations of thermal conductance at solid-gas interfaces." *Physical Review E* 87.2 (**2013**): 022119.

[62] Xufei Wu, and Tengfei Luo. "The importance of anharmonicity in thermal transport across solid-solid interfaces." *Journal of Applied Physics* 115.1 (**2014**): 014901.

[63] Mingchao Wang, et al. "Enhanced interfacial thermal transport across graphene–polymer interfaces by grafting polymer chains." *Carbon* 85 (**2015**): 414-421.

[64] Yu Wang, et al. "A molecular dynamics study on thermal and mechanical properties of graphene–paraffin nanocomposites." *RSC Advances* 5.101 (**2015**): 82638-82644.

[65] Rouzbeh Rastgarkafshgarkolaei, Yi Zeng, and J. M. Khodadadi. "A molecular dynamics study of the effect of thermal boundary conductance on thermal transport of ideal crystal of n-alkanes with different number of carbon atoms." *Journal of Applied Physic*s 119.20 (**2016**): 205107.

[66] James Gonzalez, Josue Ortega, and Zhi Liang. "Prediction of thermal conductance at liquid-gas interfaces using molecular dynamics simulations." *International Journal of Heat and Mass Transfer* 126 (**2018**): 1183-1192.

[67] Choon Sup Yoon, John N. Sherwood, and Richard A. Pethrick. "Growth, characterization and ultrasonic studies of n-Eicosane single crystals." *Journal of the Chemical Society, Faraday Transactions 1: Physical Chemistry in Condensed Phases* 85.10 (**1989**): 3221-3232.

[68] R. J. Stoner, and H. J. Maris. "Kapitza conductance and heat flow between solids at temperatures from 50 to 300 K." *Physical Review B* 48.22 (**1993**): 16373.

[69] E-K. Kim, et al. "Thermal boundary resistance at Ge 2 Sb 2 Te 5/ZnS: SiO 2 interface." *Applied Physics Letters* 76.26 (**2000**): 3864-3866.

[70] Ruxandra M. Costescu, Marcel A. Wall, and David G. Cahill. "Thermal conductance of epitaxial interfaces." *Physical Review B* 67.5 (**2003**): 054302.

[71] Ho-Ki Lyeo, and David G. Cahill. "Thermal conductance of interfaces between highly dissimilar materials." *Physical Review* B 73.14 (**2006**): 144301.

[72] Z. Chen, et al. "Thermal contact resistance between graphene and silicon dioxide." *Applied Physics Letters* 95.16 (**2009**): 161910.

[73] Austin J. Minnich et al. "Thermal conductivity spectroscopy technique to measure phonon mean free paths." *Physical review letters* 107.9 (**2011**): 095901.

[74] C. J. Glassbrenner, and Glen A. Slack. "Thermal conductivity of silicon and germanium from 3 K to the melting point." *Physical Review* 134.4A (**1964**): A1058.

[75] Anne M. Hofmeister, Jianjun Dong, and Joy M. Branlund. "Thermal diffusivity of electrical insulators at high temperatures: Evidence for diffusion of bulk phonon-polaritons at infrared frequencies augmenting phonon heat conduction." *Journal of Applied Physics* 115.16 (**2014**): 163517.

[76] David G Cahill. "Thermal conductivity measurement from 30 to 750 K: the 3ω method." *Review of Scientific Instruments* 61.2 (**1990**): 802-808.

[77] G. Z. Bagieva, et al. "Influence of structural defects on the thermal conductivity of polycrystalline and single-crystal PbTe." *Inorganic Materials* 48.8 (**2012**): 789-791.

[78] Yi Zhang, et al. "Intrinsic low thermal conductivity in weakly ionic rocksalt structures." *Physical Review B* 92.2 (**2015**): 020301.

[79] Ambroise van Roekeghem, et al. "High-throughput computation of thermal conductivity of high-temperature solid phases: the case of oxide and fluoride perovskites." *Physical Review X* 6.4 (**2016**): 041061.

[80] J. J. Ludlam, et al. "Universal features of localized eigenstates in disordered systems." *Journal of Physics: Condensed Matter* 17.30 (**2005**): L321.

[81] Philip B. Allen, and Joseph L. Feldman. "Thermal conductivity of disordered harmonic solids." *Physical Review B* 48.17 (**1993**): 12581.

[82] Ryogo Kubo, Morikazu Toda, and Natsuki Hashitsume. Statistical physics II: nonequilibrium statistical mechanics. Vol. 31. Springer Science & Business Media, **2012**.

[83] Sebastian G. Volz, and Gang Chen. "Molecular dynamics simulation of thermal conductivity of silicon nanowires." *Applied Physics Letters* 75.14 (**1999**): 2056-2058.

[84] Jianjun Dong, Otto F. Sankey, and Charles W. Myles. "Theoretical study of the lattice thermal conductivity in Ge framework semiconductors." *Physical Review Letters* 86.11 (**2001**): 2361.

[85] J. E. Turney, et al. "Predicting phonon properties and thermal conductivity from anharmonic lattice dynamics calculations and molecular dynamics simulations." *Physical Review B* 79.6 (**2009**): 064301.

[86] Niall J. English, and S. Tse John. "Mechanisms for thermal conduction in methane hydrate." *Physical Review Letters* 103.1 (**2009**): 015901.

[87] Melville S. Green. "Markoff random processes and the statistical mechanics of time-dependent phenomena. II. Irreversible processes in fluids." *The Journal of Chemical Physics* 22.3 (**1954**): 398-413.

[88] Ryogo Kubo. "Statistical-mechanical theory of irreversible processes. I. General theory and simple applications to magnetic and conduction problems." *Journal of the Physical Society of Japan* 12.6 (**1957**): 570-586.

[89] Aris Marcolongo, Paolo Umari, and Stefano Baroni. "Microscopic theory and quantum simulation of atomic heat transport." *Nature Physics* 12.1 (**2016**): 80.

[90] Christian Carbogno, Rampi Ramprasad, and Matthias Scheffler. "Ab initio Green-Kubo approach for the thermal conductivity of solids." *Physical Review Letters* 118.17 (**2017**): 175901.

[91] Jun Kang, and Lin-Wang Wang. "First-principles Green-Kubo method for thermal conductivity calculations." *Physical Review B* 96.2 (**2017**): 020302.

[92] Alper Kinaci, Justin B. Haskins, and Tahir Çağın. "On calculation of thermal conductivity from Einstein relation in equilibrium molecular dynamics." *The Journal of Chemical Physics* 137.1 (**2012**): 014106.

[93] John S. Tse, et al. "Thermal conductivity of solids from first-principles molecular dynamics calculations." *The Journal of Physical Chemistry C* 122.20 (**2018**): 10682-10690.

[94] Anthony JC Ladd, Bill Moran, and William G. Hoover. "Lattice thermal conductivity: A comparison of molecular dynamics and anharmonic lattice dynamics." *Physical Review B* 34.8 (**1986**): 5058.

[95] Alan JH McGaughey, and M. Kaviany. "Quantitative validation of the Boltzmann transport equation phonon thermal conductivity model under the single-mode relaxation time approximation." *Physical Review B* 69.9 (**2004**): 094303.

[96] Asegun S. Henry, and Gang Chen. "Spectral phonon transport properties of silicon based on molecular dynamics simulations and lattice dynamics." *Journal of Computational and Theoretical Nanoscience* 5.2 (**2008**): 141-152.

[97] Nico de Koker. "Thermal conductivity of MgO periclase from equilibrium first principles molecular dynamics." *Physical Review Letters* 103.12 (**2009**): 125902.

[98] Doyl Dickel, and Murray S. Daw. "Improved calculation of vibrational mode lifetimes in anharmonic solids—Part I: Theory." *Computational Materials Science* 47.3 (**2010**): 698-704.

[99] Risken, Hannes. "The Fokker-Planck equation, volume 18 of." Springer Series in Synergetics (**1989**).

[100] George E. Uhlenbeck, and Leonard S. Ornstein. "On the theory of the Brownian motion." *Physical Review* 36.5 (**1930**): 823.

[101] Robert J. Hard. "Energy-flux operator for a lattice." *Physical Review* 132.1 (**1963**): 168.

Appendix I

In this Appendix, the supplemental materials for Chapter 4 are provided. Specifically, the projected vibration density of the state of atoms in n-eicosane is analyzed. In addition, the effects of different values of imposed heat flux and the chain length of n-alkanes on thermal coupling parameters are presented.

I. 1 Projected Vibration Density of States of Interfacial Atoms

The molecular motions are also analyzed through examination of their velocity auto-correlation functions and the corresponding power spectra (i.e. the Fourier transformation of auto-correlation functions). In a solid with zero atomistic diffusivity, the power spectrum of an atom is proportional to the projected vibration density of states (pVDOS). To focus on the motion at the molecular interfaces, we calculate the ensemble-averaged power spectra along three Cartesian directions at two representative temperatures, T = 150 K and T = 300 K. As the results of the y-direction analysis are almost identical to those obtained for the z-direction, we only plot results associated with the x-direction and y-direction in Appendix Figure I.1. The power spectra along the y-direction (or z-direction) are consistent with those of "an amorphous Lennard-Jones system", indicating that the projected motions within the molecular interface planes are largely determined by the vdW forces among neighbors. As temperature increases, the signature of structural disorder, i.e. the broadness of the spectra, becomes more significant.

On the other hand, the power spectra along the x-direction show much complex spectra with multiple sharp peaks from 0 up to 800 cm^{-1} in frequency. As we know, the interface between molecular blocks of the ideal crystal of the long-chain n-alkanes can be described by the inter-block interaction, which is the integral effect from the relative weak LJ potential between atoms at the interface. In addition to the LJ potential describing the inter-molecule interaction within the molecular block, the intra-block interaction is also contributed by the strong bonding energy with the molecule. The significant discrepancy between intensity of the inter-block and intra-block forces leads the dynamics of the atoms at the interface to be dominated by the interaction within the molecular block, especially within the molecule. As the first order approximation, we interpret the *x*-direction power spectra with the simple one-dimensional linear chain model, with a unit-cell of 20 united-atoms connected with a strong spring and the united-atoms in the both edges connected to a much weaker spring that represents the interfacial vdW forces. Within this approximation, each peak corresponds to a vibration branch in the reciprocal space, and its width and shape are determined by the frequency dispersion with each branch. The sharpness of all the peaks indicates that the contrast in strength of intra-molecular forces and inter-molecular forces results in relatively small dispersions in these branches, i.e. relative narrow frequency bands. The flatness in the vibration dispersions is also associated with the spatial localization of these vibration modes. We note that the higher frequency peaks typically have narrower widths, suggesting that the higher frequency vibration modes are much localized within each molecular chain. Consequently, the higher frequency vibration motions likely contribute less to the interfacial heat transfer across the molecular interfaces. The sharpness of peaks of the power spectrum, except for the lowest frequency peak, also suggests the non-attenuation characters of these vibrational modes. Therefore, the heat transfer within the nano-meter scale of each molecular chain is likely to be ballistic-like, instead of the diffusion-like. Meanwhile, the vibration motions that are represented in the lowest frequency peak show distinct features, both in term of its broader shape, and the large temperature dependence. These vibration motions likely play a vital role in heat transfer across the molecular interfaces. Overall, the analysis of vibration motion of interfacial atoms is in good agreement with previous observation that the low-frequency vibration modes dominate the heat transfer across the interface between the nano-filers and the host materials.

I. 2 Interfacial Heat Flux

To study the effect of net heat flux on the thermal coupling-decoupling parameters, we have compared NEMD simulations with different heat flux rates. The NEMD cases at an energy exchange rate of 0.01 kcal/(mol fs) are carried out at four different temperatures (150 K, 200 K, 250 K and 300 K) for 0.5 nano-seconds. The case at an energy exchange rate of 0.02 kcal/(mol fs) is conducted at 150 K for 0.5 nano-seconds. Both NEMD simulations are performed after the system reaches the steady-state condition. As illustrated in Appendix Figure I.2, the values of the parameters describing the coupling-decoupling mechanism are not sensitive to imposed rate of net kinetic energy transfer.

I. 3 Chain Length Dependence

To study the chain length dependence of the thermal coupling-decoupling parameters, we have carried out additional equilibrium MD simulations using long-chain n-alkanes of two different lengths ($C_{10}H_{22}$ and $C_{18}H_{38}$). The chosen temperature range, between 200 K and 300 K, is within the melting temperature of different n-alkanes. MD simulations at each temperature are only carried out for a shorter period of 50 pico-seconds. Although the smaller amounts of data provide larger fluctuations of results in Appendix Figure I.3, we find that both the thermal coupling ratio (α_c) and the standard deviations of single molecule interfacial heat currents (σ_c and σ_d) in these molecule chains are comparable and have similar temperature dependence. Therefore, the thermal interfacial conductance of ideal crystal of n-alkanes is not sensitive to their chain length.

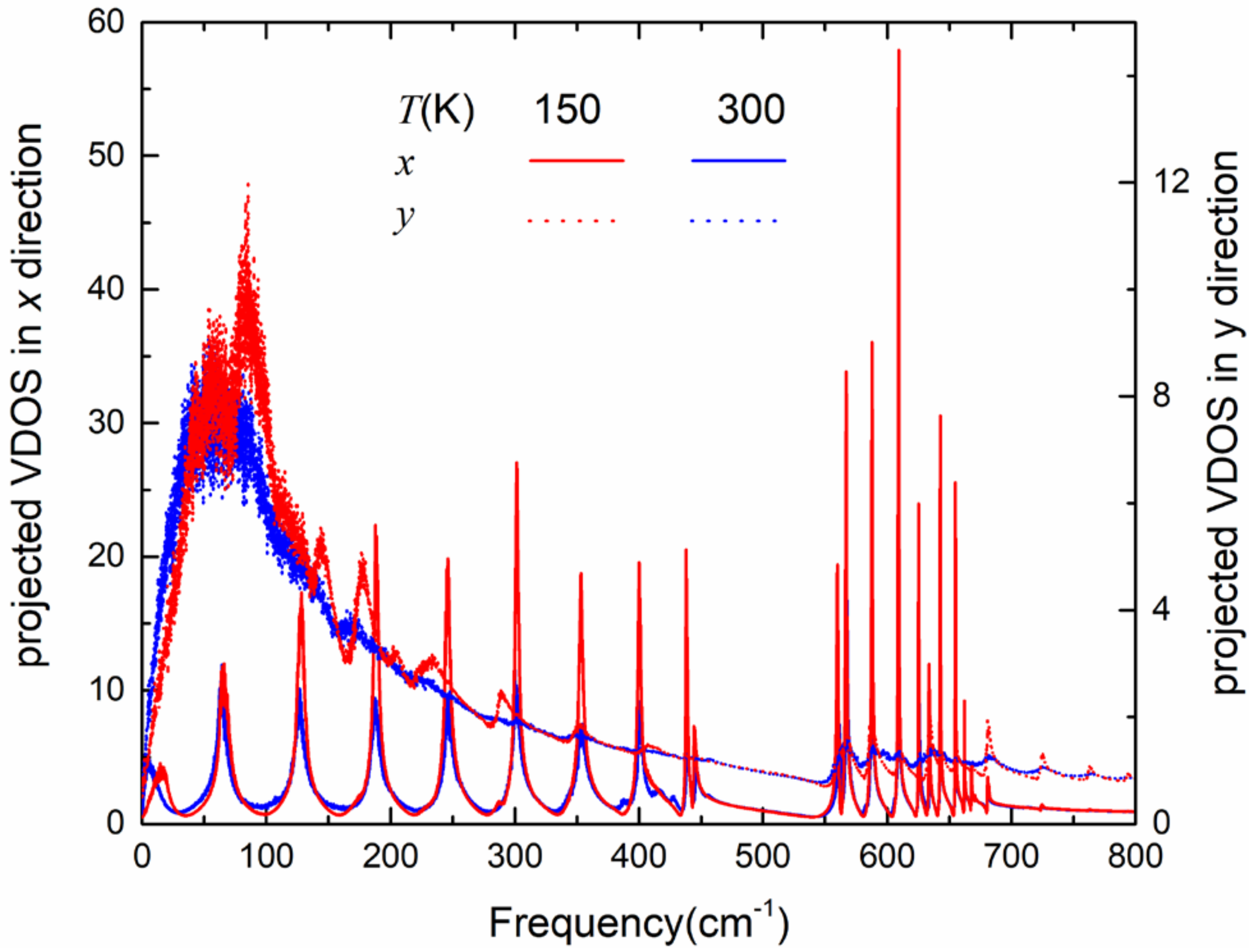

Appendix Figure I.1 Projected vibrational density of the state of the atom at an interface

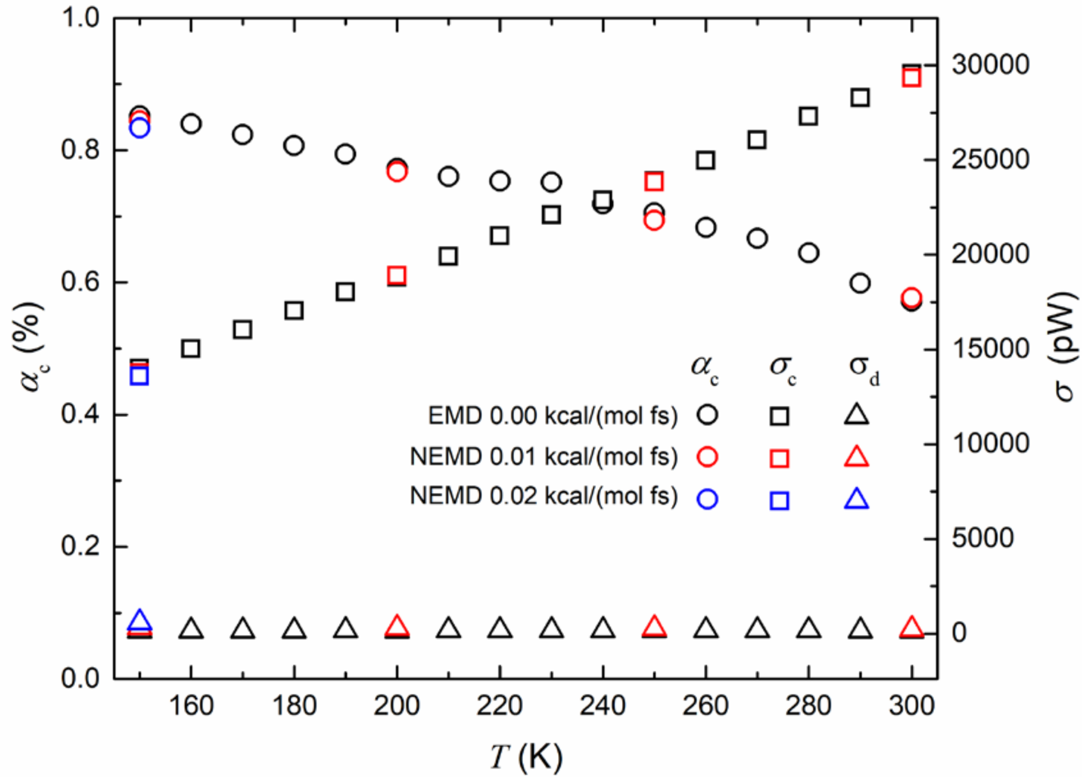

Appendix Figure I.2 Temperature dependence of two microscopic interfacial heat exchange parameters at imposed rates of net kinetic energy transfer: the thermal coupling ratio α_c (○) and standard deviation of the pulse-like heat currents σ_c (△) during the thermally-coupled time periods. For comparison purposes, we also include results of the standard deviation of the noise-like heat currents σ_d (□) during the thermally-decoupled time periods.

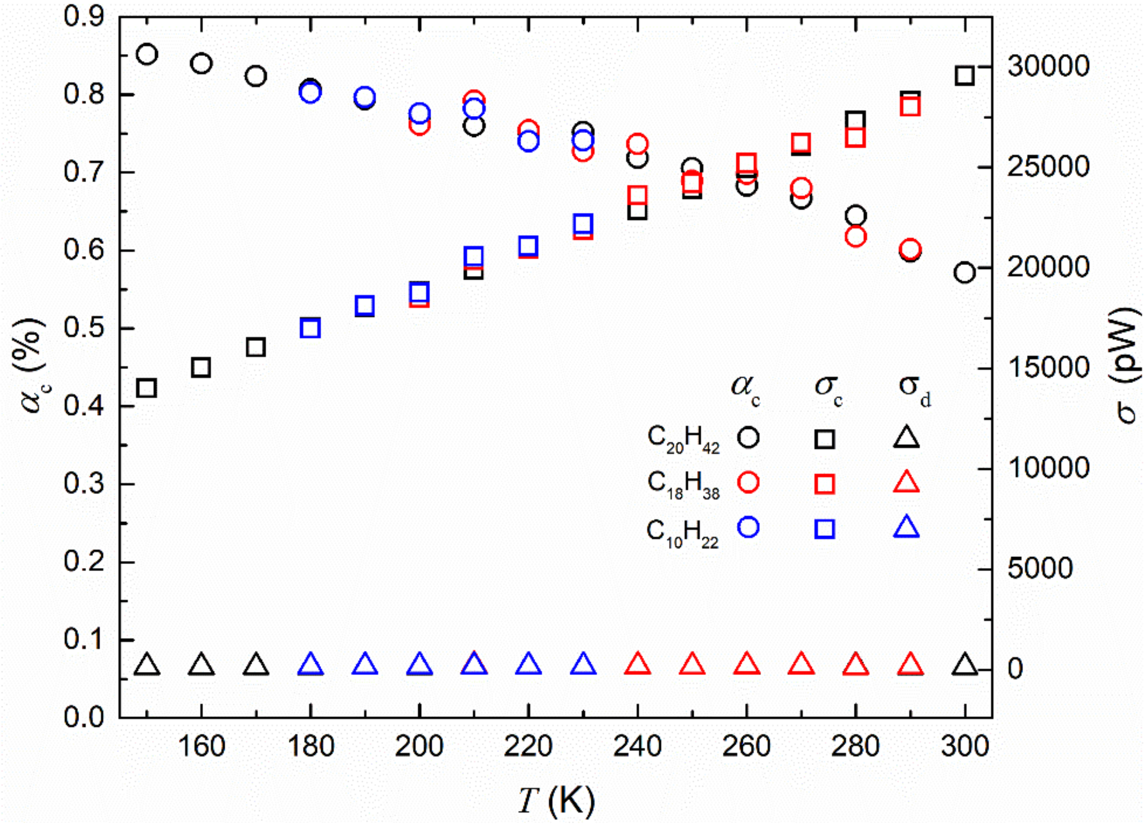

Appendix Figure I.3 Temperature dependence of two microscopic interfacial heat exchange parameters of $C_{10}H_{22}$ (blue), $C_{18}H_{38}$ (red) and $C_{20}H_{42}$ (black): thermal coupling ratio α_c (○) and standard deviation of the pulse-like heat currents σ_c (△) during the thermally-coupled time periods. For comparison purposes, we also include results of the standard deviation of the noise-like heat currents σ_d (□) during the thermally-decoupled time periods.

Appendix II

II. 1 Expectation Values and Statistical Variances of Numbers of Phonons

This Appendix provides derivation details on some formulas associated with the expectation values and statistical variances of the phonon numbers discussed in Sec. 6.2. We first define the t-dependent expectation values of the following three quantities using the ensemble average approach given in Sec. 2.2:

$$\overline{n}_\alpha(t\,|\,\Gamma^0) \equiv \langle n_\alpha \rangle = \int d\Gamma n_\alpha P(\Gamma;t) \qquad \text{Eq. (II.1)}$$

$$\overline{n_\alpha n_\beta}(t\,|\,\Gamma^0) \equiv \langle n_\alpha n_\beta \rangle = \int d\Gamma n_\alpha n_\beta P(\Gamma;t) \qquad \text{Eq. (II.2)}$$

$$\overline{\Delta}_{\alpha\beta}(t\,|\,\Gamma^0) = \langle n_\alpha n_\beta \rangle - \langle n_\alpha \rangle \langle n_\beta \rangle \qquad \text{Eq. (II.3)}$$

Using the vibration FPE shown in Eq. (6.3), we then prove that the first-order t-derivatives of these three quantities in Eq. (II.1) and Eq. (II.2) have the following forms:

$$\begin{aligned}\frac{d\overline{n}_\alpha}{dt} &= \int d\Gamma n_\alpha \frac{\partial}{\partial t} P(\Gamma,t\,|\,\Gamma^0) \\ &= -\sum_i \int d\Gamma n_\alpha \frac{\partial}{\partial n_i}[A_i(\Gamma)\cdot P(\Gamma,t\,|\,\Gamma^0)] \\ &+ \frac{1}{2}\sum_{ij}\int d\Gamma n_\alpha \frac{\partial^2}{\partial n_i \partial n_j}[B_{ij}(\Gamma)\cdot P(\Gamma,t\,|\,\Gamma^0)]\end{aligned} \qquad \text{Eq. (II.4)(50)}$$

For $\alpha \neq i$, we have $\int d\Gamma n_\alpha \frac{\partial}{\partial n_i}[A_i(\Gamma)P(\Gamma,t\,|\,\Gamma^0)] = 0$. Similarly, $\int d\Gamma n_\alpha \frac{\partial}{\partial n_i}\frac{\partial}{\partial n_j}[B_{ij}(\Gamma)P(\Gamma,t\,|\,\Gamma^0)]$ $= 0$ for $\alpha \neq i$ or $\beta \neq j$. As a result, Eq. (II.3) is now simplified as:

$$\frac{d\overline{n}_\alpha(t\,|\,\Gamma^0)}{dt} = -\int d\Gamma n_\alpha \frac{\partial}{\partial n_i}(A\cdot P) + \frac{1}{2}\int d\Gamma n_\alpha \frac{\partial^2}{\partial n_i \partial n_j}(B\cdot P), \qquad \text{Eq. (II.5)}$$

with $\int d\Gamma n_\alpha \frac{\partial}{\partial n_\alpha}(A_\alpha \cdot P) = \int d\Gamma \frac{\partial}{\partial n_\alpha}(n_\alpha A_\alpha P) - \int d(\Gamma A_\alpha P) = -\int d\Gamma A_\alpha(\Gamma)\cdot P(\Gamma,t\,|\,\Gamma^0) = -\overline{A_\alpha}(t\,|\,\Gamma^0)$,

and $\int d\Gamma n_\alpha \frac{\partial}{\partial n_\alpha}\frac{\partial}{\partial n_\alpha}(B_{\alpha\alpha}\cdot P) = \int d\Gamma \frac{\partial}{\partial n_\alpha}[n_\alpha \frac{\partial}{\partial n_\alpha}(B_{\alpha\alpha}P)] - \int d\Gamma \frac{\partial}{\partial n_\alpha}(B_{\alpha\alpha}P) = 0$.

We now get:

$$\frac{d\overline{\alpha}(t\,|\,\Gamma^0)}{dt} = \overline{A_\alpha}(t\,|\,\Gamma^0) \qquad \text{Eq. (II.6)}$$

Similarly, we can show that

$$\frac{d\overline{n_\alpha n_\beta}(t\,|\,\Gamma^0)}{dt} = \overline{n_\alpha A_\beta}(t\,|\,\Gamma^0) + \overline{n_\beta A_\alpha}(t\,|\,\Gamma^0) + \overline{B_{\alpha\beta}}(t\,|\,\Gamma^0). \qquad \text{Eq. (II.7)}$$

Consequently, we also have:

$$\begin{aligned}\frac{d\overline{\Delta_{\alpha\beta}}(t\,|\,\Gamma^0)}{dt} &= \frac{d\overline{n_\alpha n_\beta}(t\,|\,\Gamma^0)}{dt} - \overline{n_\alpha}(t\,|\,\Gamma^0)\cdot\frac{d\overline{n_\beta}(t\,|\,\Gamma^0)}{dt} - \overline{n_\beta}(t\,|\,\Gamma^0)\cdot\frac{d\overline{n_\alpha}(t\,|\,\Gamma^0)}{dt} \\ &= \overline{B_{\alpha\beta}}(t\,|\,\Gamma^0) + [\overline{n_\alpha A_\beta}(t\,|\,\Gamma^0) - \overline{n_\alpha}(t\,|\,\Gamma^0)\cdot\overline{A_\beta}(t\,|\,\Gamma^0)] + [\overline{n_\beta A_\alpha}(t\,|\,\Gamma^0) - \overline{n_\beta}(t\,|\,\Gamma^0)\cdot\overline{A_\alpha}(t\,|\,\Gamma^0)]\end{aligned}$$

Eq. (II.8)

II. 2 Analytical Solutions of the FPE for an OU Process

In this part of Appendix, we verify the analytical solutions of an OU type FPE (Eq. (6.22)) discussed in Sec. 6.2.3. For a probability function of one stochastic variable x with zero-mean and unit-variance, the corresponding OU type FPE can is given as:

$$\frac{\partial P(x,t)}{\partial t} = \gamma\cdot(1 + x\cdot\frac{\partial}{\partial x} + \frac{\partial^2}{\partial^2 x})P(x,t). \qquad \text{Eq. (II.9)}$$

With $\frac{d}{dt}\overline{x} = -\gamma\overline{x}$, $\frac{d}{dt}\overline{x^2} = 2\gamma(1-\overline{x^2}\,)$, and the initial values $\overline{x}$ and $\overline{x^2}$ being x_0 and $(x_0)^2$ respectively, we have:

$$\begin{aligned} \bar{x} &= x_0 e^{-\gamma t} \\ \Delta &= \overline{x^2} - \bar{x}^2 = 1 - e^{-2\gamma t}. \end{aligned}$$ Eq. (II.10)

We skip the details of derivation and only show that the analytical solution of Eq. (II.9) is given as:

$$P(x,t) = \frac{1}{\sqrt{2\pi\Delta(t)}} e^{-\frac{(x-\bar{x}(t))^2}{2\Delta(t)}}.$$ Eq. (II.11)

Using the analytical solution in Eq. (II.11), we can show that $\frac{\partial P(x,t)}{\partial t}$ on the left hand side of Eq. (II.9) is:

$$\begin{aligned} \frac{\partial P(x,t)}{\partial t} &= \frac{\partial[\frac{1}{\sqrt{2\pi\Delta(t)}}]}{\partial t} e^{-\frac{(x-\bar{x}(t))^2}{2\Delta(t)}} + \frac{1}{\sqrt{2\pi\Delta(t)}} \frac{\partial[e^{-\frac{(x-\bar{x}(t))^2}{2\Delta(t)}}]}{\partial t} \\ &= \gamma[1-\Delta^{-1}(t)]P(x,t) + \gamma[\frac{(x-\bar{x}(t))^2}{\Delta^2(t)} - \frac{x\cdot(x-\bar{x}(t)}{\Delta(t)}]P(x,t) \\ &= \gamma[1-\Delta^{-1}(t)\cdot(1-x\bar{x}(t)+x^2)+\Delta^{-2}(t)\cdot(x-\bar{x}(t))^2]P(x,t) \end{aligned}$$ Eq. (II.12)

From the analytical solution Eq. (II.10), we also have $\frac{\partial P(x,t)}{\partial x} = -\Delta^{-1}(t)\cdot(x-\bar{x}(t))\cdot P(x,t)$ and $\frac{\partial^2 P(x,t)}{\partial x^2} = -\Delta^{-1}(t) + \Delta^{-2}(t)\cdot(x-\bar{x}(t))^2 \cdot P(x,t)$. These results give us the right hand side of Eq. (II.9) in the form of:

$$\begin{aligned} &\gamma\cdot[1+x\cdot\frac{\partial}{\partial x}+\frac{\partial^2}{\partial^2 x}]P(x,t) = \\ &\gamma\cdot[1-x\cdot\Delta^{-1}(t)\cdot(x-\bar{x}(t))-\Delta^{-1}(t)+\Delta^{-2}(t)\cdot(x-\bar{x}(t))^2]\cdot P(x,t) = \\ &\gamma\cdot[1-\Delta^{-1}(t)\cdot(1-x\cdot\bar{x}(t)+x^2)+\Delta^{-2}(t)\cdot(x-\bar{x}(t))^2]\cdot P(x,t) \end{aligned}$$ Eq. (II.13)

With both Eq. (II.12) and Eq. (II.13), we now verify that the probability function in Eq. (II.11) is indeed the analytical solution of Eq. (II.9).

For the case $N > 1$, the N-dimensional probability function of an OU type FPE (Eq. (6.22)) can be expressed in a separable form $P(\tilde{\Gamma}, t) = \prod_{\lambda=1}^{N} f_\lambda(x_\lambda, t)$, and one N-variable FPE (Eq. (6.22)) is converted into N sets of partial differential equations:

$$\frac{\partial f_\lambda(x,t)}{\partial t} = \gamma_\lambda \cdot \left(1 + x_\lambda \cdot \frac{\partial}{\partial x_\lambda} + \frac{\partial^2}{\partial^2 x_\lambda}\right) f_\lambda(x,t) \qquad \text{Eq. (II.14)}$$

where $\lambda = 1, 2, 3, \cdots N$. Similar to the solution shown in Eq. (II.11), we have the N sets of solutions of $f_\lambda(x,t) = (2\pi\Delta_\lambda)^{-1/2} \cdot e^{-\frac{(x_\lambda - \overline{x_\lambda})^2}{2\Delta_\lambda}}$, with $\overline{x_\lambda} = x_{\lambda,0} e^{-\gamma_\lambda t}$ and $\Delta_\lambda = 1 - e^{-2\gamma_\lambda t}$. Plugging these results in the separable multiple-variable formula, we now can verify that the analytical solution of Eq. (6.22) is indeed the probability function shown in Eq. (6.23).

The analytical solution of the probability function for an OU type FPE allows us to directly derive the correlation functions among these state variables with zero-means and unit-variances. For example, the time correlation functions between any two such stochastic variables can be shown to have the following familiar forms:

$$\begin{aligned} \langle x_\lambda(t') \cdot x_{\lambda'}(t' + t) \rangle_{eq} &= \langle x_\lambda(0) \cdot x_{\lambda'}(t) \rangle_{eq} \\ &= \langle x_\lambda \cdot x_{\lambda'} \rangle_{eq} e^{-\gamma_{\lambda'} t} \qquad \text{Eq. (II.15)} \\ &= \delta_{\lambda,\lambda'} e^{-\gamma_\lambda t} \end{aligned}$$

Meanwhile, we can prove that all three-variable correlation functions for a multiple variable OU process zero:

$$\begin{aligned} \langle x_\lambda(0) \cdot x_{\lambda'}(0) \cdot x_{\lambda''}(t) \rangle_{eq} &= \langle x_\lambda \cdot x_{\lambda'} \cdot x_{\lambda''} \rangle_{eq} e^{-\gamma_{\lambda''} t} \\ &= 0 \cdot e^{-\gamma_{\lambda''} t} \qquad \text{Eq. (16)} \\ &= 0, \end{aligned}$$

$$\begin{aligned}\langle x_{\lambda}(t)\cdot x_{\lambda'}(0)\cdot x_{\lambda''}(t)\rangle_{eq} &= \langle x_{\lambda}\cdot x_{\lambda'}\cdot x_{\lambda''}\rangle_{eq} e^{-2\gamma_{\lambda''}t} + \langle x_{\lambda}\rangle_{eq}\cdot(1-e^{-2\gamma_{\lambda''}t})\cdot\delta_{\lambda'\lambda''} \\ &= 0\cdot e^{-2\gamma_{\lambda''}t} + 0\cdot(1-e^{-2\gamma_{\lambda''}t})\cdot\delta_{\lambda'\lambda''} \\ &= 0.\end{aligned} \tag{Eq. (II.17)}$$

We can further generalize that the correlation functions of odd-number variables, such as three-variable, five-variable, etc, are all zero. At the same time, the correlation functions of even-number variables are not always zero. For example, for four-variable correlation functions, we have the following free formula:

$$\begin{aligned}\langle x_{\lambda}(0)\cdot x_{\lambda'}(0)\cdot x_{\lambda''}(0)\cdot x_{\lambda'''}(t)\rangle_{eq} &= \langle x_{\lambda}\cdot x_{\lambda'}\cdot x_{\lambda''}\cdot x_{\lambda'''}\rangle_{eq} e^{-\gamma_{\lambda'''}t} \\ &= (\delta_{\lambda\lambda'''}\cdot\delta_{\lambda'\lambda''} + \delta_{\lambda'\lambda'''}\cdot\delta_{\lambda\lambda''} + \delta_{\lambda''\lambda'''}\cdot\delta_{\lambda\lambda'})e^{-\gamma_{\lambda'''}t},\end{aligned}$$

$$\begin{aligned}&\langle x_{\lambda}(0)\cdot x_{\lambda'}(t)\cdot x_{\lambda''}(t)\cdot x_{\lambda'''}(t)\rangle_{eq} \\ = \quad & \langle x_{\lambda}\cdot x_{\lambda'}\cdot x_{\lambda''}\cdot x_{\lambda'''}\rangle_{eq} e^{-(\gamma_{\lambda'}+\gamma_{\lambda''}+\gamma_{\lambda'''})t} + \langle x_{\lambda}x_{\lambda'}\rangle_{eq}\cdot e^{-\gamma_{\lambda'}t}\cdot(1-e^{-2\gamma_{\lambda''}t})\cdot\delta_{\lambda''\lambda'''} + \\ & \langle x_{\lambda}x_{\lambda''}\rangle_{eq}\cdot e^{-\gamma_{\lambda''}t}\cdot(1-e^{-2\gamma_{\lambda'}t})\cdot\delta_{\lambda'\lambda'''} + \langle x_{\lambda}x_{\lambda'''}\rangle_{eq}\cdot e^{-\gamma_{\lambda'''}t}\cdot(1-e^{-2\gamma_{\lambda'}t})\cdot\delta_{\lambda'\lambda''} \\ = \quad & (\delta_{\lambda\lambda'}\cdot\delta_{\lambda''\lambda'''} + \delta_{\lambda\lambda''}\cdot\delta_{\lambda'\lambda'''} + \delta_{\lambda\lambda'''}\cdot\delta_{\lambda'\lambda''})\cdot e^{-(\gamma_{\lambda'}+\gamma_{\lambda''}+\gamma_{\lambda'''})t} + \\ & e^{-\gamma_{\lambda}t}\cdot[\delta_{\lambda\lambda'}\cdot\delta_{\lambda''\lambda'''}\cdot(1-e^{-2\gamma_{\lambda''}t}) + \delta_{\lambda\lambda''}\cdot\delta_{\lambda'\lambda'''}\cdot(1-e^{-2\gamma_{\lambda'}t}) + \delta_{\lambda\lambda'''}\cdot\delta_{\lambda'\lambda''}\cdot(1-e^{-2\gamma_{\lambda'}t})] \\ = \quad & (\delta_{\lambda\lambda'}\cdot\delta_{\lambda''\lambda'''} + \delta_{\lambda\lambda''}\cdot\delta_{\lambda'\lambda'''} + \delta_{\lambda\lambda'''}\cdot\delta_{\lambda'\lambda''})e^{-\gamma_{\lambda}t},\end{aligned}$$

Eq. (II.18)

Eq. (II.19)

$$\begin{aligned}&\langle x_{\lambda}(0)\cdot x_{\lambda'}(0)\cdot x_{\lambda''}(t)\cdot x_{\lambda'''}(t)\rangle_{eq} \\ = \quad & \langle x_{\lambda}\cdot x_{\lambda'}\cdot x_{\lambda''}\cdot x_{\lambda'''}\rangle_{eq} e^{-(\gamma_{\lambda''}+\gamma_{\lambda'''})t} + \langle x_{\lambda}x_{\lambda'}\rangle_{eq}\cdot(1-e^{-2\gamma_{\lambda''}t})\cdot\delta_{\lambda''\lambda'''} \\ = \quad & (\delta_{\lambda\lambda''}\cdot\delta_{\lambda'\lambda'''} + \delta_{\lambda\lambda'''}\cdot\delta_{\lambda'\lambda''} + \delta_{\lambda\lambda'}\cdot\delta_{\lambda''\lambda'''})e^{-(\gamma_{\lambda''}+\gamma_{\lambda'''})t} + \delta_{\lambda\lambda'}\cdot\delta_{\lambda''\lambda'''}\cdot(1-e^{-2\gamma_{\lambda''}t}) \\ = \quad & \delta_{\lambda\lambda'}\cdot\delta_{\lambda''\lambda'''} + (\delta_{\lambda\lambda''}\cdot\delta_{\lambda'\lambda'''} + \delta_{\lambda\lambda'''}\cdot\delta_{\lambda'\lambda''})e^{-(\gamma_{\lambda}+\gamma_{\lambda'})t}.\end{aligned} \tag{Eq. (II.20)}$$